ABSTRACT

Title of Dissertation: THEORETICAL AND NUMERICAL STUDIES OF TROPICAL CYCLONE DEVELOPMENT

Chanh Q. Kieu, Doctor of Philosophy, 2008

Dissertation directed by: Professor Da-Lin Zhang
Department of Atmospheric and Oceanic Science

Part I of this dissertation is devoted to a theoretical study of tropical cyclones (TCs), in which a class of exact solutions is obtained. These solutions capture well many important dynamical aspects of the TC development. Major results include:

- A strong dependence of the TC growth rate on the vertical structure, i.e., the lower the level of the maximal tangential wind, the faster TCs will grow;
- A much faster TC growth rate inside the radius of the maximal wind than that outside; and
- The key dynamical roles of the secondary circulation in controlling the evolution and structures of TCs. In particular, the bottom-upward development of the cyclonic flow is demonstrated to be a consequence of the secondary circulation.

The new analytical model provides a systematic way to construct the three-dimensional storm structures needed for initialization of TC models. An application of the new theory in deriving the pressure-wind relationship is also presented.

In Part II, the genesis of Tropical Storm Eugene (2005) is studied, using a cloud-resolving, multiple-grid simulation with the Weather Research and Forecast (WRF) model. It is shown that the genesis of Eugene is a result of the merger of two

mesovortices associated with the ITCZ breakdowns. The simulation captures well the vortex merger as well as Eugene's life-cycle developments. Some key findings include:

- The merger of mesoscale vortices is critical for the genesis of Eugene;
- The total potential vorticity associated with the merging vortices increases substantially during the merging phase as a result of the net internal dynamical forcing between the PV condensing and diabatic production and partly from the continuous PV fluxes from the ITCZ; and
- Cyclonic vorticity grows from the bottom upward during the merger due to deep convection caused by the low-level frictional convergence and latent heating. Without deep convection, little vorticity growth could result from the vortex merger.

THEORETICAL AND NUMERICAL STUDIES OF TROPICAL CYCLONE DEVELOPMENT

By

Chanh Q. Kieu

Dissertation submitted to the Faculty of the Graduate School of the
University of Maryland, College Park, in partial fulfillment
of the requirements for the degree of
Doctor of Philosophy
2008

Advisory Committee:

Prof. Da-Lin Zhang, Chair
Prof. James Carton
Prof. Ferdinand Baer
Prof. Daniel Kirk-Davidoff
Prof. James Wallace

DEDICATION

To my parents, my wife, and my son

ACKNOWLEDGEMENTS

First, I would like to express my heartfelt thank to Prof. Da-Lin Zhang for having been not only my inspirational academic advisor but also my dear friend as well as my fellow for the last five years. His endless encouragement and enthusiasm in science have been and is helping me shape my thinking and perspectives of science and life. By asking me repeatedly a simple question "why", Prof. Zhang has pushed me continuously to think hard about many different problems, which very often led me in the end to new ideas and creativities, for which I am deeply grateful.

I am tremendously indebted to the faculties and fellow students in the Department of the Atmospheric and Oceanic Science here at Maryland, who have shown and taught me invaluable lessons of generosity, open-mindedness, and friendship beyond the mere course works. To me, these lessons are of vital importance not only for those who wish to become a good scientist but also for those who simply want to be a good person. Special thank to Wallace Hogsett and Debra Baker for their extremely careful and comprehensive revision of this dissertation.

Finally, and most importantly, my deepest thanks go to my family, who have always supported me and been with me. Even with their tiny incomes, my parents have been so determined to give me a chance to study aboard that they went through painful financial debts for me to be here today. My dear wife decided to discontinue her pursuit of higher education as well as her favorite studies to follow me anywhere I would go. My uncles, brothers and sisters always supported and encouraged me continuously during my studying here in the US. With these dedications alone, I can never say enough thanks to my family.

I would like to take this opportunity to also apologize those who have helped me during the course of my Ph.D. years at the University of Maryland and Saint Louis University but their names are not mentioned explicitly in this acknowledgement due to the limited space. Life is always a stochastic and intriguing story, and sometimes (actually, many times), a simple help or good advice we come across here and there may twist our life forever. I myself have been fortunate to experience such lucky moments more than one, and I just want to say thank the people who have believed in me and given me such an opportunity.

This doctoral research receives financial support partly from the graduate research assistantship under Prof. Zhang's research grants and partly from the Vietnam Education Foundation.

08/2008
College Park, Maryland
Kiều Quốc Chánh

TABLE OF CONTENTS

LIST OF TABLES

LIST OF FIGURES

(dashed). The observed profile is reproduced from McBride (1981).

Figure 1.7. Radius-height cross section of the tangential wind (contoured) at intervals of 3 m s^{-1} and pressure perturbations (shaded at intervals of 2 hPa), superimposed by in-plane flow vectors, as constructed from the analytical solutions obtained in section 3.

Figure 2.1. (a) Hovmöller diagram of the vertical absolute vorticity (unit: 10^{-5} s^{-1}) at 850 hPa during the period of 0000 UTC 11 - 1200 UTC 18 July 2005 and the longitudinal span of 120^0 – 65^0W that is obtained by meridionally averaging 3 slices (i.e., 3^0) of NCEP's reanalysis following V_1's center, starting at 8^0N; (b) *GOES-10/12 CIMSS* images of clouds, superimposed by the low-level winds valid at 0000 UTC 11 July 2005; and (c) NCEP's reanalysis of the 850-hPa streamlines (solid), isotachs (dashed, every 2 m s^{-1}), and relative humidity (shaded for 85% and 95%). Letters, "V_1" and "V_2", denote the two MCVs associated with the formation of TS Eugene (shown as "E"); similarly for the rest of the figures. Hurricane symbol marks the evolution of Emily (2005). Note that V_2 does not exist before 0000 UTC 13 July.

Figure 2.2. *GOES-10/12 CIMSS* images of clouds, superimposed by the low-level winds, from 0000 UTC 17 to 0000 UTC 21 July 2005. More frequent timeframes are shown during the period of 0600 UTC 17 – 0900 UTC 18 July in order to show better the merger of V_1 and V_2.

Figure 2.3. West-east vertical cross sections from NCEP's reanalysis of the vertical absolute vorticity that is area-averaged within a 3^0 latitudinal span centered along 14^0N, at intervals of 2 x 10^{-5} s^{-1}, superimposed by in-plane horizontal wind barbs, along the two vortex centers, valid at (a) 0000 UTC 18; and (b)

1200 UTC 18 July 2005. The absolute vorticity values of greater than 4, 8, and 12×10^{-5} s^{-1} are shaded.

Figure 2.4. NCEP reanalysis of the sea-level pressure (solid, every 2 hPa), the horizontal flow vectors and relative humidity (shaded for 85% and 95%) at 900 hPa at (a) 0000 UTC 17; and (b) 0000 UTC 20 July 2005. The model meshes with horizontal resolutions of 36, 12, 4, and 1.33 km for domains A, B, C, and D are, respectively, sketched in (a), along with the observed (thick line) and simulated (thick-dashed) tracks. The finest domain D follows the movement of the storm, and D_1 and D_N denote the first and the last position of domain D.

Figure 2.5. South-north vertical cross sections along 103^0W from the NCEP reanalysis at 0000 UTC 17 July 2005 of (a) the zonal wind speeds (at intervals of 2 m s^{-1}), superimposed with horizontal wind barbs (a full barb is 5 m s^{-1}) and relative humidity (shaded for > 85% and > 95%); (b) PV (at intervals of 0.2 PVU; 1 PVU = 10^{-6} m^2 s^{-1}K kg^{-1}) and meridional PV gradient (shaded for negative values); and (c) equivalent potential temperature θ_e (solid, at intervals of 2 K), superimposed by deviation temperature (dashed, at intervals of 0.3 K, shaded for negative values). Shading at the lower right corner denotes the terrain over Mexico

Figure 2.6. (a) Comparison of the simulated track (dashed) of Eugene to the best track analysis (solid), superimposed by the SST field (dotted) at intervals of 1^0C. The simulated minimum pressure positions of Eugene at the three selected model levels (z = 0, 5, 10 km) are also shown. Note that the model-data points are given at the corresponding best track analysis times. Lower left

corner enlarges the tracks of both "V_1" and "V_2", based on their 850-hPa relative vorticity and surface pressure centers, from 18/00-24 to 18/18-39 at 3-h intervals. Time-height cross section of the (400 km x 400 km) area-averaged horizontal wind barbs centered at (b) V_1 and (c) V_2 from 17/00-00 to 19/12-60. Note that the wind barbs in (b) and (c) become more similar after 18/06-30 and identical after 18/18-39 due to their merging.

Figure 2.7. Time series of (a) the simulated maximum surface wind (solid, m s^{-1}) versus the observed (dotted); and (b) the simulated minimum sea-level pressure (solid, hPa) versus the observed (dotted) during the 4-day period of 17/00-00 to 21/00-96. Note that the best track analysis is only available during the final 54 hours. The time evolution of the area-averaged (800 km × 800 km) VWS (long-dashed, m s^{-1}) in the layer of 200 – 900 hPa is also shown in (b). VWS during the first 36-h simulation is taken around V_1's and V_2's center within an area of 400 km × 400 km because of their reducing distance with time.

Figure 2.8. Comparison of the 6-h accumulated rainfall (mm) valid at the (a) 17/06-06; (b) 18/00-24; (c) 18/12-36; (d) 19/00-48; (e) 19/12-60; and (f) 20/00-72 simulations over a subdomain of C to the corresponding 6-h TRMM satellite-estimated (contoured). The simulated surface flow vectors are also provided.

Figure 2.9. As in Fig. 2.1 but for the model-simulated during the period of 0000 UTC 17 - 0000 UTC 21 July 2005 (i.e., 17/00-00 to 21/00-96) and the longitudinal span of 115^0 – 95^0W. It is meridionally averaged within a 1^0 zone centered through the MCV V_1 and later Eugene.

Figure 2.10. Horizontal distribution of the sea-level pressure (at intervals of 1 hPa)

and flow vectors (bottom); flow vectors and streamlines at 500 hPa (middle); and flow vectors and streamlines at 200 hPa (top) over a subdomain of C at (a) 18/06-30; (b) 18/12-36; (c) 18/18-42; and (d) 19/06-54. Shadings in the top and bottom panels are for the simulated radar reflectivity, at intervals of 5 dBz, and in the middle panels are for PV, at intervals of 0.5 PVU. Line "AB" shows vertical cross sections used in Fig. 2.11. All flows are system relative.

Figure 2.11. As in Fig. 2.10 but for the 3-slice-averaged (i.e., 4-km) vertical cross sections of the normal component of horizontal winds (at 2 m s^{-1} intervals), PV (shaded at intervals of 0.5 PVU), superimposed by the system-relative in-plane flow vectors along the centers of V_1 and V_2 (see Fig. 2.10 for their locations). Note that the vertical wind component has been amplified by a factor of 10.

Figure 2.12. Vertical cross sections of the north-south average of PV (shaded, every 0.5 PVU) within ± 360 km along the line through the centers of V_1 and V_2, and the corresponding PV tendency (contoured, every 10^{-4} PVU s^{-1}), superimposed with the vertical motion vectors, from 18/09-33 to 18/23-47. Bold-dashed lines are for convectively generated vortices spawn within V_2 and V_1.

Figure 2.13. As for Fig. 2.12 but for horizontal distribution of the vertically averaged PV (shaded at interval of 0.2 PVU), superimposed with flow vectors at z = 3 km.

Figure 2.14. Time series of the BPV (in PVU unit) from the hourly model outputs: BPV (solid), BPV after subtracting the net PV flux at the boundaries (short-dashed), BMPV after subtracting the net mass-weighted PV flux at the

boundaries (long-dashed) for a control volume of 720 km × 720 km × 10 km following V_2 until 18/18-42 and then Eugene. The corresponding total mass flux is also plotted (dotted, 10^7 kg s^{-1}).

Figure 2.15. As in Fig. 2.14 but for (a) the BPV tendency (solid), the net boundary PV fluxes (dotted), and the sum of the PV condensing and heating-generation rates (dashed); and (b) the PV condensing rate (solid), the PV generation rate by diabatic heating (dashed), the PV boundary flux due to normal flows (dotted) and to the movement of the control volume (thin solid). The unit is 10^{-6} PVU s^{-1}.

Figure 2.16. Vertical profiles of the control (720 km × 720 km) area-averaged quantities. Upper panel: PV (q, dotted, unit: 0.2 PVU), 3D velocity divergence (3DIV, solid, unit: 10^{-5} s^{-1}), and diabatic heating rates (H, dot-dashed, unit: 2×10^{-4} K s^{-1}), and 2D divergence (2DIV, dashed, unit: 10^{-5} s^{-1}); Middle panel: the vertical (η, solid, unit: 10^{-5} s^{-1}) and horizontal (ω_{xy}, dotted, unit: 5×10^{-4} s^{-1}) components of the absolute vorticity, the vertical (Q_z, dashed) and horizontal (Q_{xy}, dot-dashed) contributions of QH; Bottom panel: QH (short-long dashed), QCON (dashed), the net boundary PV flux divergence (QBND, dot-dashed), vertical PV flux divergence (VFLX, i.e., $\partial(wq)/\partial z$, solid) and QTEN (dotted). All the PV forcing terms have the unit of 10^{-5} PVU s^{-1}. The left, middle and right columns are for 18/03-27, 18/12-36, and 20/00-72, respectively.

Figure 2.17. Height-time cross sections of the (720 km × 720 km) area-averaged quantities from the hourly model outputs: (a) PV (solid, every 0.1 PVU), and QCON (shaded, every 0.3×10^{-5} PVU s^{-1}); (b) diabatic heating rates (shaded, every 0.2×10^{-3} K s^{-1}) and the potential temperature deviation from its initial

value (solid, every 0.5 K); and (c) 3DIV (solid, every 0.2 × 10^{-5} s^{-1}) and QH (shadings, at intervals of 10^{-5} PVU s^{-1}). Thick-dashed lines denote the melting level.

Figure 2.18. As in Fig. 2.12, but (a) – (d) for the 3D advection of PV (i.e., $-\vec{u} \bullet \nabla q$, every 5 × 10^{-5} PVU s^{-1}), superimposed with the vertical component of the diabatic PV generation rates (i.e., $\rho^{-1}\eta \partial H / \partial z$, shadings); and (e) –(h) for the diabatic PV generation rate (i.e., $\rho^{-1}\vec{\omega} \bullet \nabla H$, every 5 × 10^{-5} PVU s^{-1}), superposed with the diabatic heating rates (shaded at intervals of 3 × 10^{-4} K s^{-1}) and in-plan absolute vorticity vectors ($\vec{\omega}_{xz}$) during the merging period between 18/13-37 and 18/19-43. Note that η has been multiplied by 10 in constructing the $\vec{\omega}_{xz}$ vectors. Solid (dashed) lines are for positive (negative) values.

Figure 2.19. . As in Fig. 2.17, but for (a) the vertical component of absolute vorticity (every 10^{-5} s^{-1}), and the stretching rates (shaded, every 5 × 10^{-10} s^{-2}); (b) the bulk stretching rates (shaded, every 10^{-10} s^{-2}) and 2DIV (contoured, every 10^{-5} s^{-1}); and (c) the bulk tilting rates (shaded, every 10^{-10} s^{-2}) and the absolute vorticity tendency (solid, every 3 × 10^{-10} s^{-2}). Bold-dashed lines in (a) are for the ridge axis of the absolute vorticity.

Figure 2.20. As in Fig. 2.12, but for the vertical absolute vorticity (every 3 × 10^{-5} s^{-1}) superimposed with its total tendency (shaded at intervals of 4 × 10^{-9} s^{-2}) during the period of 18/13-37 – 18/23-47. Solid (dashed) lines are for positive (negative) values.

Figure 2.21. A schematic description of tropical cyclogenesis from two merging

MCVs: (a) prior to the merger; (b) during the initial merging phase; (c) complete merging of the midlevel MCVs; and (d) the formation of a tropical storm. The shaded areas with thin arrows denote MCVs; dashed lines show isobaric or isentropic surfaces; and large shaded arrows represent lower-level flow directions.

Figure 2.22. Initial condition of the vertical component of the absolute vorticity field at z = 3 km (shaded in the intervals of 10^{-5} s^{-1}) for (a) control run; and (b) after the MCV V_1 is removed from the initial condition valid at 17/00-00. Superimposed is the flow field (vectors) at the corresponding level

Figure 2.23. Simulated tracks for the control run (solid) and three sensitivity experiments (dashed): V_1 is removed from the initial condition (NOV1), no frictional convergence (NFRC), and 12 km domain is shifted 500 km to the east to include Hurricane Emily nearby (SHIF). Superimposed are the 700 hPa flow field (vectors) and sea level pressure (contour, intervals of 1 hPa) valid at 18/06-39. Note that dash line in CTL panel is for the best track

Figure 2.24. Time series of the simulated minimum sea-level pressure (hPa) during the 4-day period of 17/00-00 to 21/00-96 for the sensitivity experiments: control run (solid), NOV1 (dashed), NFRC (dotted), SHIF (dotted-dashed)

Figure 2.25. Time series during the 4-day period of 17/00-00 to 21/00-96 of the area average of (a) the sensible heating flux; and (b) latent heat flux for the CTL (solid) and NFRC experiments (dashed). The unit is W s^{-1}

Figure 2.26. Horizontal distribution of the radar reflectivity (shaded at 5-dBz intervals) and flow vectors at 850 hPa at 18/12-36, 19/00-48, 19/12-60, 20/00-72, 20/12-84, and 21/00-96 over a subdomain of C. Hodographs with vertical

shear vectors (solid) between 900 and 200 hPa, that are obtained by averaging them over an area of 800 km × 800 km at the storm center, are sketched with the speed scale given on the top and right frames.

Figure 2.27. Three-dimensional view (800 km × 800 km × 12 km) of the θ_e = 352 K isosurface superimposed by the storm-relative surface flow vectors from a subdomain of C at (a) 19/18-66; and (b) 20/06-78.

Figure 2.28. (a) Horizontal distribution of θ_e (at intervals of 2 K), flow vectors, and vertical motion (shaded at intervals 0.1 m s^{-1} for descending and 0.3 m s^{-1} for ascending motion) at 700 hPa at 19/12-60; (b) as in (a) but for vertical cross section through the storm center of θ_e (at intervals of 2 K) and deviation potential temperature (θ', shaded); and (c) as in (b) but for 19/18-66. Superimposed in (b) and (c) are the storm-relative in-plane flow vectors. Note that the vertical motion has been amplified by a factor of 10. Line A-B in (a) shows the 3-slice-averaged (i.e., 4-km) vertical cross sections used in (b) and (c).

LIST OF ABBREVIATIONS

2DIV:	Two dimensional flow divergence
3D:	Three Dimensional
3DIV:	Three dimensional flow divergence
AMSU-A:	Advanced Microwave Sounding Unit satellite
BMPV:	Bulk (or volume-averaged) mass-weighted potential vorticity
BPV:	Bulk (or volume-averaged) potential vorticity
CAPE:	Convective Available Potential Energy
CISK:	Conditional Instability of Second Kind
CGV:	Convectively-Generated Vortex
CTL:	Control-run simulation
HRD:	Hurricane Research Division
ITCZ:	Inter-Tropical Convergence Zone
MM5:	Fifth-Generation NCAR/Penn State Mesoscale Model
MPI:	Maximal Potential Intensity
MCS:	Mesoscale Convective System
MCV:	Mesoscale Convective Vortex
NASA:	National Aeronautics and Space Administration
NOAA:	National Oceanic and Atmospheric Administration
NCEP:	National Centers for Environmental Prediction
NFRC:	Sensitivity experiment with no frictional effects
NMI:	National Meteorological Institute
NLB:	Nonlinear Balance

NOV1: Sensitivity experiment with no vortex V_1

PBL: Planetary Boundary Layer

PC: Primary Circulation

PV: Potential Vorticity

PVR: Pressure-Wind Relationship

QBND: Net across-boundary PV fluxes

QCON: Condensing or diluting rate of PV due to the 3D flow divergence

QFLX: 3D normal-to-boundary flows of PV

QH: A PV forcing term caused by the 3D diabatic heating gradient

QMOV: PV changes due to the control volume's movement

QTEN: Time rate of the total PV within a control volume

R1: Inner core region of troposphere (WISHE theory)

R2: Eyewall region of troposphere (WISHE theory)

R3: Outer region of troposphere (WISHE theory)

RMW: Radius of Maximal Wind

SC: Secondary Circulation

SHIF: Sensitivity experiment with the domain shifted to the east

SSM/I: Special Sensor Microwave Imager

SST: Sea Surface Temperature

TC: Tropical Cyclone

TCG: Tropical Cyclogenesis

TD: Tropical Depression

TRMM: Tropical Rainfall Measuring Mission

TCSP: Tropical Cloud Systems and Processes field experiment

TS:	Tropical Storm
VHTs:	Vortical Hot Towers
VMPV:	Volume integration of Mass-weighted Potential Vorticity
VPV:	Volume integration of Potential Vorticity
VWS:	Vertical Wind Shear
WISHE:	Wind Induced Surface Heat Exchange
WKB:	Wentzel, Kramers and Brillioun (method)
WRF:	Weather Research and Forecasting model

PART I. THEORY OF TROPICAL CYCLONES

Chapter 1. Introduction

1.1. Background

A remarkably large number of hurricanes in the North Atlantic Ocean (so-called typhoons in the Western Pacific or tropical cyclones in the Southwest Indian Ocean, hereafter referred generally to as TCs) in 2005 make this year the most active TC season ever. The same situation also occurred in the Western Pacific in both 2005 and 2006 when the number of TCs, the length of the TC season as well as TC tracks show remarkable irregularities compared with previous years. Whether this is an isolated seasonal event or will happen again in the upcoming years is an important question that needs to be addressed explicitly. At the deepest essence, this unresolved question is related to our incomplete understanding of the formation of TCs and their subsequent development. Answering this question will enhance our understanding of the connection between TC activities and global warming, an issue of vital importance in atmospheric science.

The lifecycle of TCs is typically divided into four different phases: the genesis stage with no closed isobar at the surface, tropical depression (TD), tropical storm (TS), and finally hurricane stage. Despite extensive research in the past decades and considerable progress in the forecasts of TC track and intensity, our current understanding of each phase still remains elusive, even at the most well-defined hurricane stage. In particular, tropical cyclone genesis (TCG), a process by which a weak disturbance grows into a TD, is poorly understood because of the lack of high-

resolution observations at the very early phase of TC development and deficiencies in current TC models. Each year there are many disturbances but only a small fraction of these disturbances develop fully into TCs (e.g. McBride and Zehr 1981; DeMaria 2001).

The main obstacle in theoretical studies of TCs is so far due to the seemingly insurmountable complexity of the Navier-Stoke equations, which prevents us from obtaining detailed analytical descriptions of both dynamical and thermodynamical processes within TCs. Especially, the evolution of TCs at their early TD stage is often characterized by a rapid growth before approaching a quasi-stationary mature stage. This is a critical transition period in the lifetime of TCs but much of our current knowledge about this rapid intensification is based on limited observations and high-resolution modeling studies.

1.2. Objectives

In Part I of this thesis, an analytical axisymmetric model of TC development in response to organized deep convection is proposed, in which all nonlinear terms in the horizontal momentum equations are retained. Some key issues that we would like to tackle are:

- Does a class of exact solutions to the Navier-Stokes equations exist that could describe realistically the TC development as captured by observations and modeling studies? How different is the TC development from the perspectives of the primary circulation and the secondary circulation?;
- Is there any dependence of the growth rate of TCs on its vertical structure? What are the roles of the secondary circulation in determining the vertical structure as well as evolution of TCs?; and

- Is the TC development from the bottom-upward or top-downward at the lower half of the troposphere? What physical mechanisms could explain such growth of the cyclonic vorticity?

By assuming a positive feedback between buoyancy and vertical motion, we will show that there does exist a class of time-dependent analytical solutions for both the primary and secondary circulations of TCs with our axisymmetric model, given the vertical profile of diabatic heating rate in the inner-core region. The analytical solutions are shown to capture many observed dynamical structures as well as the intensity and growth of TCs from the early genesis to hurricane stages. We will demonstrate further that the analytical model can be used to construct dynamically consistent vortices for TC models, and to derive the functional relationship between the central pressure and maximum tangential wind. Limitations and possible improvements of the analytical model are also discussed.

Chapter 2. Review of the theories of tropical cyclones

2.1. Theoretical foundation

At the most fundamental level, TCs are described by the following system of the fluid equations: the Navier-Stokes equations (in Cartesian coordinates)

$$\frac{du}{dt} = -2\Omega \times u - \frac{1}{\rho}\nabla p + g + F\,, \tag{1.1}$$

the continuity equation

$$\frac{d\rho}{dt} + \rho\nabla \cdot U = 0\,, \tag{1.2}$$

the state equation

$$p = p(\rho, T)\,, \tag{1.3}$$

and the thermodynamic equation

$$C_p \frac{dT}{dt} - \frac{1}{\rho}\frac{dp}{dt} = J\,, \tag{1.4}$$

where the differential operator is defined as

$$\frac{d}{dt} \equiv \frac{\partial}{\partial t} + u\frac{\partial}{\partial x} + v\frac{\partial}{\partial y} + w\frac{\partial}{\partial z},$$

U = (u, v, w) denotes the 3D flow field with three components in x, y, and z directions, p is pressure, ρ denotes density, T is temperature, J is diabatic heating, F represents frictional forcing, g is gravitational constant, and C_p is the specific heat capacity at constant pressure. Upon taking Reynolds average, the rhs of Eqs. (1.1) – (1.4) will contain some eddy components, e.g., $\overline{(u'v')}$, $\overline{(u'w')}$, $\overline{(u'T')}$, which need to be parameterized. Given the forcing terms F and J as well as necessary parameterizations for the eddy terms, the above system is closed with six unknowns

(u, v, w, p, ρ, T) and it could be, in principle, solved completely. One of the most challenging tasks in understanding the development of TCs lies in how to parameterize the eddy forcing terms properly in the TC conditions.

Typically, TCs are characterized by a circular mesoscale moist vortex with a deep cyclonic flow thorough the troposphere and an anticyclonic flow within a thin layer just below the tropopause. As TCs are highly axisymmetric, it is more convenient for theoretical purposes to transform the system of equations (1.1) – (1.4) to the cylindrical coordinates (r, φ, z) as follows:

$$\frac{du}{dt} - \frac{v^2}{r} = -\frac{1}{\rho}\frac{\partial p}{\partial r} + fv + F_u, \tag{1.5}$$

$$\frac{dv}{dt} + \frac{uv}{r} = -\frac{1}{\rho}\frac{\partial p}{r\partial \varphi} - fu + F_v, \tag{1.6}$$

$$\frac{dw}{dt} = -\frac{1}{\rho}\frac{\partial p}{\partial z} + g + F_w, \tag{1.7}$$

$$\frac{\partial \rho}{\partial t} + \nabla \cdot (\rho U) = 0, \tag{1.8}$$

where $\nabla = \partial/\partial r + (1/r)\partial/\partial\varphi + \partial/\partial z$, $F_{u,v,w}$ are components of F in r, φ, and z directions, respectively. The state and thermodynamic equations, Eqs. (1.3) and (1.4), are of the same form in both coordinate systems. As the tangential wind v is typically one order of magnitude larger than the vertical component w and radial component u during most of the TC lifetime, Eqs. (1.5) – (1.8) are often expanded in terms of a non-dimensional number, for instance, the ratio of u over v (see, e.g., Willoughby 1979; Montgomery and Farrell 1991). This linearization enables us to obtain two separate subsystems: one for the primary circulation (zero order) and the other for the secondary circulation (first order). Both observations and modeling studies show that

TCs can be approximated to a good degree by the gradient-wind balanced relationship during most of their development stage (e.g. Willoughby 1990; Zhang et al. 2001; Hendricks et al 2004). Therefore, Eq. (1.5) is replaced by

$$\frac{v^2}{r} = -\frac{1}{\rho}\frac{\partial p}{\partial r} + fv. \qquad (1.9)$$

This gradient-wind balanced approximation underlies all contemporary theories of TCs and serves a wide range of applications with some considerable success.

2.2. Balanced dynamics

Perhaps the earliest theoretical framework of TCs is the gradient-wind or nonlinear balanced model in which the divergent wind component is considered to be much smaller than the TC rotational flow. One of the restrictions of this approximation is that it does not allow us to examine how the secondary circulation (SC) which consists of convergent inflow in the planetary boundary layer (PBL), vertical motion in the inner-core region and divergent outflow aloft, interacts with the primary circulation (PC). Because of this limitation, quasi-balanced prognostic models, first introduced by Eliassen (1952), have been proposed to describe the characteristics of the SC resulting from diabatic and frictional processes (Willoughby 1979; Shapiro and Willoughby 1982) and the associated slow evolution of an axisymmetric vortex (e.g., Sundqvist 1970; Schubert and Hack 1982; Hack and Schubert 1986). Essentially, this quasi-balanced model consists of three basic equations:

- The Saywer-Elliassen equation, which is obtained by combining the gradient balance equation, the thermal wind relationship, and the hydrostatic approximation as follows (see, e.g., Yanai 1965)

$$\frac{\partial}{\partial r}\left(A\frac{\partial(r\psi)}{r\partial r} + B\frac{\partial \psi}{\partial z}\right) + \frac{\partial}{\partial z}\left(B\frac{\partial(r\psi)}{r\partial r} + C\frac{\partial \psi}{\partial z}\right) = \frac{g}{\theta_0}\frac{\partial J}{\partial r} + \frac{\partial(\eta F_r)}{\partial z}, \quad (1.10)$$

where ψ is the streamfunction representing the transverse circulation, η is the absolute vorticity, θ_0 denotes the reference potential temperature at 1000 hPa, and the coefficients *A, B*, and *C* in Eq. (1.10) are given by:

$$A = \frac{g}{\rho\theta_0}\frac{\partial\theta}{\partial z}, \text{ representing the static stability,}$$

$$B = -\frac{g}{\rho\theta_0}\frac{\partial\theta}{\partial r}, \text{ representing the baroclinic stability,}$$

$$C = \frac{f^2}{4r^3\rho}\frac{\partial}{\partial z}\left[\frac{2rv}{f} + r^2\right], \text{ representing inertial instability,}$$

- The horizontal momentum equation for the tangential wind:

$$\frac{\partial v}{\partial t} = -\left(u\frac{\partial v}{\partial r} + w\frac{\partial v}{\partial z} + \frac{uv}{r}\right) - fu, \quad (1.11)$$

- The hydrostatic equations:

$$\frac{\partial \phi}{\partial z} = \frac{g\theta}{\theta_0}. \quad (1.12)$$

where θ is potential temperature. The radial and vertical flow components *u* and *w* are determined from the transverse streamfunction as follows:

$$(\rho u, \rho w) = \left(-\frac{\partial \psi}{\partial z}, \frac{\partial(r\psi)}{r\partial r}\right). \quad (1.13)$$

Given a diabatic heating distribution *J* and frictional distribution F_r, the quasi-balanced SC can be obtained by solving Eqs. (1.10) and (1.13). Together with the gradient-wind relationship (1.9), the system of Eqs. (1.10) - (1.13) is complete and can be used to study the evolution of the balanced vortex in a quasi-balanced

framework.

Since the seminal work of Hoskins et al. (1985) about the balanced dynamics associated with potential vorticity (PV), a different formulation for the quasi-balanced dynamics has emerged. In this new formulation, two key relationships are needed (see e.g. Davis and Emanuel 1992; Wang and Zhang 2003):

The Charney nonlinear balanced (NLB) equation:

$$\nabla^2\Phi = \nabla_h(f\nabla_h\Psi) + 2J(\frac{\partial\Psi}{\partial x},\frac{\partial\Psi}{\partial y}) + \nabla_h.F\,, \qquad (1.14)$$

and the PV equation:

$$q = \frac{1}{r(z)}\frac{\theta_0}{g}\left[(f+\nabla_h^2\Psi)\frac{\partial^2\Phi}{\partial z^2} - \frac{\partial^2\Psi}{\partial x\partial z}\frac{\partial^2\Phi}{\partial x\partial z} - \frac{\partial^2\Psi}{\partial y\partial z}\frac{\partial^2\Phi}{\partial y\partial z}\right], \qquad (1.15)$$

where $z = [1 - (P/P_0)^{R/Cp}](C_p\theta_0/g)$ is the vertical pseudo-height coordinate, and $r(z) = \rho_0(P/P_0)^{R/Cp}$ is pseudo-density, Ψ is a horizontal streamfunction that should be distinguished cautiously with the transverse streamfunction ψ in Eq. (1.19), and Φ is geopotential. Given a distribution of PV, q, and necessary boundary conditions, it is possible to invert Eqs. (1.14) and (1.15) to obtain the full 3D balanced dynamics. The NLB equation is essentially the divergent equation in the limit of the small Rossby number approximation with the forcing terms, from left to right, respectively representing the Coriolis forcing, advection, and frictional effects. The system of PV-NLB equations (1.14) and (1.15) has been widely used to diagnose the TC intensification (Möller and Shapiro 2002), the TC structural changes through the wave-mean flow and the wave-wave interaction of vortex Rossby waves (Möller and Montgomery 2000).

The PV inversion has recently been extended to include the omega equation to

study TC asymmetric, balanced characteristics (Wang and Zhang 2003) and examine the effects of vertical wind shear and the quasi-balanced contributions to forced SCs (Zhang and Kieu 2006). In both quasi-balanced systems, one has to assume *a priori* the PC in order to study the structures and evolution of the SC. In this sense, the SC is just a passive agent in the development of TCs.

2.3. CISK theory

The Conditional Instability of the Second Kind (CISK) theory is one of the first attempts to study the growth of TDs analytically (Charney and Eliassen 1964; Ooyama 1969). It considers the SC as a perturbation superimposed on a given symmetrical balanced vortex. This perturbation is characterized by a streamfunction Ψ', and the growth of TDs is attributed to some kind of instability that is assumed to grow exponentially with time as $\Psi' = \Psi(r)e^{\beta t}$, where β is the growth rate. This instability is postulated to be the result of a self-amplifying feedback mechanism between the latent heat release and the fictional convergence. A stronger balanced vortex will create more low-level convergence which, in the work of Charney and Eliassen (1964), is controlled by the Ekman pumping. This enhanced low-level convergence will pick up more moisture at the ocean surface, advect it vertically and produce further latent heat release at the upper levels. The diabatic heating will strengthen the balanced vortex via the gradient-wind balanced adjustment and thermal wind relationship, and the vortex keeps intensifying, and so on. By following this direction, Charney and Eliassen (1964) found an important relationship between the growth rate β and the scale radius of the cloud disk covering TDs. The functional

dependence of β on a is complicated but the main point is that the smaller the scale of TDs, the faster their growth rate would be[1].

The same feedback mechanism was later utilized by Ooyama (1969) in a 2D slab model of TCs in which he showed more completely and consistently the development of TCs at the early stages. By assuming a direct dependence of the diabatic heating profile on the vertical motion, Ooyama obtained a quite similar dependence of the growth rate on scale of TDs except for very small-scale TDs, where no growth can occur. In the Charney and Eliassen's model, the growth rate is maximal for the small-scale TDs.

Several weaknesses with the CISK theory should be pointed out. First, the growth rate β is uniform with radius, i.e. the perturbation grows at the same rate at all radii. This contradicts the observations and modelling studies (e.g. Willoughby 1990) which all show that TDs tend to develop much more rapidly within the inner-core area than in the outer area. Second, the exact solutions for the perturbation streamfunction Ψ' are obtained only at one specific level. The explicit dependence of the solutions on radius and height is not provided. Third, a time-dependent solution for the mean balanced vortex, which is the most important characterization for TDs, is not achieved. Finally, the CISK theory assumes implicitly that the growth of TCs is characterized by the quasi-balanced growth of the SC. This tends to underestimate the real TC development as it is the PC associated with the tangential flow that decides

[1]The detailed functional dependence of the growth rate β on the horizontal scale a is given implicitly from the following matching condition:

$$\frac{B_1(\lambda_+ a)}{B_0(\lambda_- a)} = i\frac{\lambda_- H_1^{(1)}(i\lambda_- a)}{\lambda_+ H_0^{(1)}(i\lambda_+ a)}$$

where $B_{0,1}$ and $H^{(1)}_{0,1}$ are, respectively, the Bessel and Hankel functions of the first kind of order 0 and 1, a is the radius of the cloud disk at which the ascending motion is separated from descending motion, $\lambda_\pm$ is an explicit function of the growth rate $\lambda_\pm(\beta)$.

the strength of TCs. The fact that the PCs are often one order of magnitude larger than that the SCs is a clue that it may be insufficient to examine the growth of TCs merely from the behaviours of the SCs. This will be elucidated in our new theory of the TC development presented in Chapter 3.

2.3. WISHE theory

Emanuel (1986, hereinafter E86) proposed a different analytical theory of TC growth with the particular focus on the mature TCs. Assuming the neutral slantwise convection and gradient-wind balance, E86 arrived at an important relationship between equivalent potential temperature θ_e and pressure at the top of the PBL as follows:

$$-\frac{T_B-\overline{T}_{out}}{T_B}\ln\frac{\theta_e}{\theta_{ea}}=\ln\frac{\Pi}{\pi_a}+\frac{r}{2}\frac{\partial\ln\Pi}{\partial r}+\frac{f^2}{4C_pT_B}(r^2-r_0^2)\ \text{ at } z=h \qquad (1.16)$$

where T_B is temperature at the PBL top (i.e., $z = h$), T_{out} is the outflow temperature at the upper level, θ_{ea} is the ambient equivalent potential temperature, and Π is the Exner function representing the pressure field $\Pi = (p/p_0)^{R/Cp}$. While this relationship contains two unknown variables θ_e and Π, some immediate inferences can be drawn including the proportionality of the central pressure with the potential temperature anomaly θ'_e, and the decrease of the relative humidity with radius inward along the top of the PBL, which can be used to predict the upper bound of the TC intensity.

To solve for Eq. (1.16), another relationship between θ_e and Π is needed. This relationship can be derived from the assumption of the gradient-wind balance:

$$M^2=r^3[C_pT_B\frac{\partial\ln\Pi}{\partial r}+\frac{fr^4}{4}], \qquad (1.17)$$

where $M = rv + f^2r/2$, and from the assumption of the conservations of the angular momentum and the entropy *within the boundary* (i.e. $z \in [0,h]$), which gives

$$\ln\theta_e = \ln\theta_{ea} - \frac{C_D}{C_\theta}\frac{1}{C_p(T_B - T_0)}(v^2 + \frac{frv}{2}), \qquad (1.18)$$

where and T_0 is an constant approximation of T_{out}. While Eqs. (1.16) - (1.18) are in principle enough to solve for completely the three unknowns Π, v and θ_e, some technical difficulties associated with the high order polynomial dependence in solving these equations arise. To overcome these difficulties, E86 introduced a semi-empirical approach that separates the PBL into three different regimes: inner core region (R1), eyewall region (R2), and the outer region (R3). Within R1 and R2, the Rossby number is assumed to be large enough such that $fr << v$. This leads directly to an explicit dependence of v on Π from Eq. (1.17). By using Eq. (1.18), the exact solutions for Π and θ_e are easily obtained. For the R3, the assumption of the constant relative humidity along $z = h$ results in an exact dependence of Π on θ_e, and the explicit solutions can be obtained upon using Eq. (1.16). The assumption of the constant relative humidity for R3 is justified from the observations during the mature stage (see e.g. Frank 1977 and E86 for more discussion).

E86's theory has two important consequences. The first is an exact dependence of the maximal surface wind V_{max} on the drag coefficients C_D and C_θ. This important feature is the cornerstone for the Emanuel's later development of the so-called Wind Induced Surface Heat Exchange (WISHE) theory, which essentially *assumes the same dependence of V_{max} on the drag coefficients for the early developing stage of TCs*. According to WISHE theory, a stronger vortex leads to larger heat and moisture fluxes from the ocean surface (through the eddy transport by

cumulus convection), which in turn enhance the buoyant forcing and result in a further growth of the vortex. The main feedback mechanism lies in the interaction between the vortex and the exchanges at the ocean surface. Under the air-sea feedback mechanism, a vortex can grow even in a convectively neutral environment. This WISHE hypothesis has been verified *numerically* by Rotunno and Emanuel (1987). The second remarkable result is a connection of the maximal potential intensity (MPI) that a TC can attain and the difference between ocean surface temperature and the average temperature of the outflows below the tropopause is obtained explicitly. It is this difference that suggests a similarity between TCs and the Carnot cycle. The efficiency of energy conversion from ocean surface into the atmosphere is decided by the sea surface temperature (SST): the higher the SST, the stronger a TC would be.

The roles of air-sea interaction were in fact addressed long ago in the early works of Yanai (1964) and Ooyama (1969). Ooyama (1969) even proposed an equation that relates the perturbation equivalent potential temperature θ'_e within the boundary to the eddy fluxes at the surface. This equation controls the feedback between the ocean heat and moisture at the surface and the vertical heating function. In Ooyama's 2D simulation, this feedback is enough to spin up a weak vortex to a hurricane in a reasonable timescale. However, it is Emanuel who was the first to derive an explicit dependence of the TC strength on this air-sea interaction. Based on his finding, Emanuel (1995) suggested the MPI of a TC as follows:

$$V_{\max}^2 = C_p (T_s - T_0) \frac{T_s}{T_0} \frac{C_k}{C_D} (\ln \theta_e^* - \ln \theta_e)\big|_m \qquad (1.19)$$

where V_m is the maximal surface wind, T_s is the surface temperature, and θ^*_e is the

saturated equivalent potential temperature at the ocean surface.

Several comments should be noted about E86's theory. First, all analytical solutions are obtained only at the top of the PBL, i.e., $z = h$. In order to find the full 2D structure of TCs from the top of the PBL to the tropopause, a temperature distribution T has to be given *a priori* and the balanced equation be solved iteratively to get the whole distribution of the absolute angular momentum.. Secondly, it should be cautioned that the radial profile of the tangential wind v within R1 is not derived from the theory but given from observation. The theory is thus no self-contained. A recent study by Smith et al. (2008) points out further that Emanuel's MPI theory tends to underestimate the actual intensity of TCs due to the assumption of the gradient wind balance within the PBL, the so-called superintensity in Smith et al. (2008). Finally, because E86's theory is for the mature TCs, no time-dependent solutions for TCs have been achieved.

Chapter 3. A new theoretical model of tropical cyclogenesis

3.1. Theoretical framework

To present our new formulation of TC development by organized convection in a more transparent framework, we first transform the system of Eqs. (1.5) – (1.8) from the physical space to the pseudo-height coordinates system and replace the potential temperature θ by a new variable b that represents the buoyancy. The new system of equations in the pseudo-height coordinates is

$$\frac{\partial u}{\partial t}+u\frac{\partial u}{\partial r}+\frac{v}{r}\frac{\partial u}{\partial \varphi}+w\frac{\partial u}{\partial z}-\frac{v^2}{r}=-\frac{\partial \phi}{\partial r}+fv+F_u, \tag{1.20}$$

$$\frac{\partial v}{\partial t}+u\frac{\partial v}{\partial r}+\frac{v}{r}\frac{\partial v}{\partial \varphi}+w\frac{\partial v}{\partial z}+\frac{uv}{r}=-\frac{1}{r}\frac{\partial \phi}{\partial \varphi}-fu+F_v, \tag{1.21}$$

$$\frac{\partial w}{\partial t}+u\frac{\partial w}{\partial r}+\frac{v}{r}\frac{\partial w}{\partial \varphi}+w\frac{\partial w}{\partial z}=b, \tag{1.22}$$

$$\frac{1}{r}\frac{\partial}{\partial r}(ru)+\frac{1}{r}\frac{\partial v}{\partial \varphi}+\frac{\partial w}{\partial z}-Sw=0, \tag{1.23}$$

$$\frac{\partial b}{\partial t}+u\frac{\partial b}{\partial r}+\frac{v}{r}\frac{\partial b}{\partial \varphi}+N^2w=\frac{Jg}{\overline{T}}, \tag{1.24}$$

where ϕ is the geopotential height perturbation from its reference value $\overline{\phi}(z)$; $b \equiv$ gT'/$\overline{T}(z)$ is the buoyancy; f is the Coriolis parameter; N is the buoyancy frequency; $S = -1/\rho\partial\rho/\partial z \equiv N^2/g$ is a stratification parameter; and J denotes the diabatic heating rate (see Willoughby 1979). For the convenience of our derivation, parameters f, and N will be treated as constants. The reference geopotential height $\overline{\phi}(z)$ and temperature $\overline{T}(z)$ are assumed to be in hydrostatic balance and invariant with time.

In this study, we make the following assumptions: (i) TCs are axisymmetric; (ii) the vertical motion w is proportional to the diabatic heating rate J (i.e., $J = \tau\, w$); and (iii) the nonlinear terms in Eqs. (1.22) and (1.24) can be neglected. Regarding the assumption (i), the axisymmetry should be considered as the internal dynamical nature of TCs at any stage of their development. All flow asymmetries are caused by environmental factors such as vertical wind shear, horizontal deformation, or inhomogeneities in the atmosphere and oceans, which are not considered herein. The feedback assumption (ii) implies the presence of a self-amplifying mechanism by which the greater the buoyancy resulting from latent heat release, the stronger the vertical motion is. Perhaps the assumption (iii) is the most severe limitation of this analytical model, because it would lead to the unbounded growth of TCs. A justification for this assumption is based on the fact that both w and b are small at the lower and upper levels, whereas $\partial w/\partial z$ and $\partial b/\partial z$ are small at the middle level. Nonetheless, relaxing this assumption is necessary for a more realistic description of TCG, and this will be explored in a forthcoming work in which a numerical approach will be invoked.

With the above assumptions, Eqs. (1.20) - (1.24) now become

$$\frac{\partial u}{\partial t} + u\frac{\partial u}{\partial r} + w\frac{\partial u}{\partial z} - \frac{v^2}{r} = -\frac{\partial \phi}{\partial r} + fv - \kappa u, \tag{1.20'}$$

$$\frac{\partial v}{\partial t} + u\frac{\partial v}{\partial r} + w\frac{\partial v}{\partial z} + \frac{uv}{r} = -fu - \kappa v, \tag{1.21'}$$

$$\frac{\partial w}{\partial t} = b, \tag{1.22'}$$

$$\frac{1}{r}\frac{\partial}{\partial r}(ru) + \frac{\partial w}{\partial z} - Sw = 0, \tag{1.23'}$$

$$\frac{\partial b}{\partial t} + N^2 w = \alpha w. \qquad (1.24')$$

where $\kappa(z)$ is a frictional drag coefficient, and $\alpha \equiv \tau g / \overline{T}(z)$. Eqs. (1.20') - (1.24') will be solved over a cylindrical domain Ω (r, φ, z) defined as: $\Omega = [0, R_m] \times [0, 2\pi] \times [0, H_0]$ with the following initial and boundary conditions:

$$u_{r=R_m} = u_{r=0} = 0; \quad w_{z=0} = w_{z=H_0} = 0;$$

$$v_{r=R_m} = v_{r=0} = 0; \quad \Phi_{r=R_m} = 0. \qquad (1.25)$$

Initial condition for buoyancy b is denoted by a cloud disk of radius a covering the inner-core region of a TC vortex,

$$b(\mathrm{r}, \mathrm{z}, \mathrm{t} = 0) = \begin{cases} B_0 \sin(\lambda z) & r \le a \quad \textit{(region I)} \\ 0 & r > a \quad \textit{(region II)} \end{cases}, \qquad (1.26)$$

where B_0 and $\lambda = \pi / H_0$ are constants. It is worth pointing out that the initial conditions for the other variables cannot be arbitrarily chosen because they are constrained by Eqs. (1.20') - (1.24') and (1.26). These dynamical constrains will be demonstrated in section 3.5 to be of importance in constructing 3D vortices for TC models. Table 1 lists the definition and dimension of all the parameters used in the present study. Because J, w, and b are proportional to each other, (1.26) may be also referred to as the initial profile for either the heating rate or vertical motion. Although the top-hat heating function (1.26) may be more suitable for TCG stage, its vertical profile resembles closely that diagnosed from a cloud-resolving simulation of hurricanes (see Fig. 8 in Zhang et al. 2002). To obtain more realistic flow structures of hurricanes, the radial heating distribution may need to be modified to fit the eyewall pattern with much greater values of B_0 than those during the early stages of TCG.

Table 1.1. Dimension and specification of parameters used for the theoretical model

Parameters	Remarks	Values
a	Radius of the cloud disk	100 km
B_0	Area-averaged heating parameter for the cloud disk	2×10^{-7} m s^{-2}
β	Growth rate parameter [$\beta \equiv (\alpha - N^2)^{1/2}$]	10^{-5} s^{-1}
f	The Coriolis parameter at 10^{o}N	2×10^{-5} s^{-1}
G_0	An integral constant evaluated from Eq. (23) with an assumed vortex of V_{max} = 10 m s^{-1} at a = 100 km	2.7×10^{-5} s^{-1}
H_0	Depth of the troposphere	15 km
H_{PBL}	Depth of the PBL	1 km
λ	Inversed depth of the troposphere (= π/H_0)	2.1×10^{-4} m^{-1}
κ_0	Frictional drag coefficient at z = 0	5×10^{-5} s^{-1}
R_m	The outer radius of a TC beyond which the ambient environment is at rest	2000 km
S	Stratification parameter ($S \equiv N^2/g$)	10^{-5} m^{-1}

By assuming the feedback between the vertical motion w and buoyancy b, the equation system of (1.20') - (1.24') can be divided into two subsystems: one for the vertical motion and buoyancy [i.e., (1.22') and (1.24')], and the other for the geopotential height perturbation ϕ, the tangential v and radial wind u [i.e., (1.20'), (1.21') and (1.23')]. Once solutions for w and b are obtained, solution for u will follow from (1.23'), v from Eq. (1.21'), and ϕ from Eq. (1.20'). In other words, given the diabatic heating rate function (1.26), the TC development can be estimated from Eqs. (1.20') – (1.24').

3.2. Analytical solutions

We first combine Eqs. (1.22') and (1.24') to obtain a solution for the vertical motion

$$w(r,z,t) = w_1(r,z)e^{\beta t} + w_2(r,z)e^{-\beta t}, \qquad (1.27)$$

where $\beta \equiv (\alpha - N^2)^{1/2}$. Using the initial condition (1.26) and considering only the growing mode, we have

$$w(\mathrm{r,z,t}) = \begin{cases} W_0 \sin(\lambda z) e^{\beta t} & r \le a \quad \textit{(region I)} \\ 0 & r > a \quad \textit{(region II)} \end{cases}, \qquad (1.28)$$

where $W_0 \equiv B_0/\beta$. Strictly speaking, β is a function of z, as is N, but β can be approximated as a constant after limiting the WKB (Wentzel, Kramers and Brillioun) expansion of the exponential function to the first order. This approximation amounts to the assumption of a constant deepening rate of TCs in the vertical, which is not a severe constraint as TCs often show a near-constant growth rate at all levels. To see this point, Fig. 1.1 shows the simulated time series of the deepening of Tropical Storm Eugene (2005) at three different vertical (i.e., lower, middle and upper) levels using the Weather Research and Forecasting (WRF-ARW) model; see Kieu and Zhang (2008) for a detailed case description.

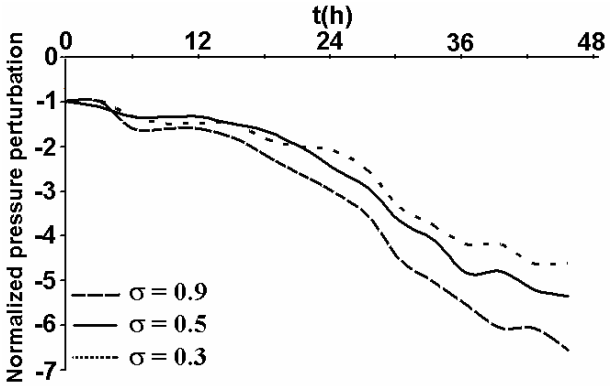

Figure 1.1. Time series of the pressure perturbation at three different sigma levels: σ = 0.9 (long-dashed); σ = 0.5 (solid); and σ = 0.3 (short-dashed) from the simulation of Tropical Storm Eugene (2005) using the WRF model. All pressure perturbations are normalized to their values at t = 0.

Except for a few minor differences, the central pressure time series (and deepening rates) are similar at all the levels. Since diabatic heating is assumed to occur only in the inner-core region (i.e., $r \le a$), the remaining solutions for variables *u, v,* and ϕ will be derived from Eqs. (1.20'), (1.21') and (1.23') for the inner-core region (I) and the outer region (II), separately.

a. Analytical solutions for Region I

From the continuity equation (1.23') and $w_1(r,z,t) = H(z)e^{\beta t}$, where $H(z)=W_0 \sin(\lambda z)$, the radial wind in Region I is given by

$$u_1(r,z,t) = (SH - \frac{dH}{dz})e^{\beta t}\frac{r}{2} + \frac{C_1}{r} \equiv Qre^{\beta t} + \frac{C_1}{r}, \tag{1.29}$$

where $Q(z)=W_0[S \sin(\lambda z) - \lambda \cos(\lambda z)]/2$, and the integral function $C_1(z,t)$ vanishes after applying the boundary condition (1.25) at $r = 0$.

Plugging Eqs. (1.28) and (1.29) into Eq. (1.21'), it is straightforward to obtain the following equation for the tangential wind in Region I

$$\frac{\partial v_1}{\partial t} + (Qr\frac{\partial v_1}{\partial r} + Qv_1 + H\frac{\partial v_1}{\partial z})e^{\beta t} = -fQe^{\beta t}r - \kappa v_1, \tag{1.30}$$

The only separable solution that Eq. (1.30) can admit is of the form: $v_1(r,z,t) = F_1(z,t)r$. Use of this form in Eq. (1.30), we have

$$\frac{\partial F_1}{\partial t} = -(H\frac{\partial F_1}{\partial z} + 2QF_1 + fQ)e^{\beta t} - \kappa F_1. \tag{1.31}$$

Consider an asymptotic expansion of the solution $F_1(z,t)$ in terms of the drag coefficient κ as follows

$$F_1(z,t) = F^{(0)}(z,t) + \kappa(z)F^{(1)}(z,t) + \kappa^2(z)F^{(2)}(z,t) + O(\kappa^3(z)). \tag{1.32}$$

Assuming that this series expansion converges at higher orders, we can obtain a solution for $F_1(z,t)$ with each order of $\kappa(z)$ after substituting (1.32) into (1.31). For the

simplicity of our derivation, we only present the calculation up to the first-order correction.

Consider first the zero-order solution of Eq. (1.31), which is governed by the following equation:

$$\frac{\partial F^{(o)}}{\partial t} = -e^{\beta t}(H\frac{\partial F^{(o)}}{\partial z} + 2QF^{(o)} + fQ) \tag{1.33}$$

Let $F^{(0)}(z,t) = -f/2 + F_h(z,t)$, then

$$\frac{\partial F_h}{\partial t} = -e^{\beta t}(H\frac{\partial F_h}{\partial z} + 2QF_h) \tag{1.34}$$

A simple factoring technique suggests that the solution of (1.34) is of the form

$$F_h(z,t) = G(z)\exp(\mu e^{\beta t}) \ , \tag{1.35}$$

where μ is an arbitrary positive, dimensionless number. Plugging (1.35) into (1.34), followed by an integration, an explicit form for $F_h(z,t)$ could be derived as (see Appendix I)

$$F_h(z,t) = G_0 \sin(\lambda z)e^{-Sz}\exp(\mu e^{\beta t})/[\tan(\frac{\lambda z}{2})]^{\frac{\mu\beta}{W_0\lambda}}, \tag{1.36}$$

Thus, the zero-order solution for the tangential wind is given by

$$v_1^{(0)}(r,z,t) = \{G_0 \sin(\lambda z)e^{-Sz}\exp(\mu e^{\beta t})/[\tan(\frac{\lambda z}{2})]^{\frac{\mu\beta}{W_0\lambda}} - \frac{f}{2}\}r. \tag{1.37}$$

where G_0 is an integration constant (with the unit of s^{-1}) to be determined by an observed $v_1^{(0)}$ above the PBL. Note that the double-exponential factor, $exp(\mu e^{\beta t})$, is associated with the effects of the radial and vertical advection of angular momentum [see Eqs. (1.34) and (1.35)] whereas the factor, e^{-Sz}, denotes the vertical weighting effects of the atmospheric stratification on $v_1^{(0)}$. Solution (1.37) contains an infinite number of possible solutions depending on the values of μ. However, the requirement

of the regularity of (1.37) at $z = 0$ imposes a strong restriction on the possible range of μ. Specifically, by taking a limit of (1.37), we have (see Appendix I):

$$\mu\beta/(\lambda W_0) < 1. \qquad (1.38)$$

Given β, λ and W_0, the largest possible value of μ is: $\mu_{max} = \lambda W_0/\beta$. In addition, by restricting the solutions only to the growing modes, the range of μ will be truncated to $\mu > 0$. To ease the subsequent discussion, let $\mu\beta/(\lambda W_0) = 1 - \delta$ so that δ will be in the range of [0, 1], solution (1.37) can be re-written now as

$$v_1^{(0)}(r,z,t) = \{2G_0 \sin^{\delta}(\frac{\lambda z}{2})\cos^{2-\delta}(\frac{\lambda z}{2})e^{-Sz}\exp[\frac{W_0\lambda}{\beta}(1-\delta)e^{\beta t}] - \frac{f}{2}\}r\,. \quad (1.39)$$

To help understand the physical implication of the parameter δ, Fig. 1.2 shows how the vertical profile of $v_1^{(0)}(r,z,t)$ in Region I varies with different values of δ. Apparently, the zero-order solution exhibits a deep layer of cyclonic flow in the troposphere with the peak tangential wind shifting from the surface to midlevel as δ increases from 0 to 1.

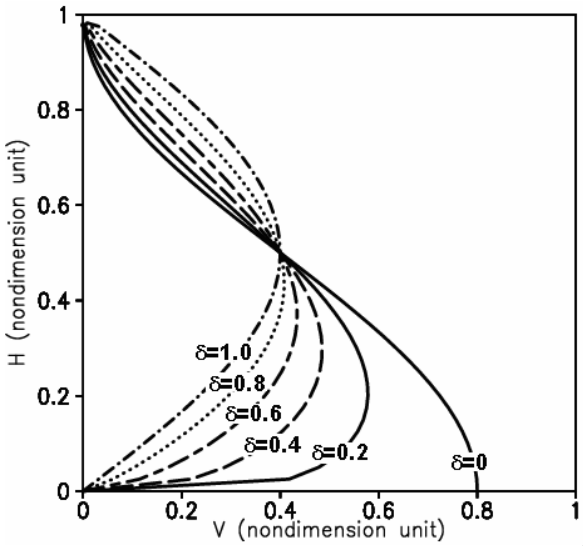

Figure 1.2. Vertical profiles of the tangential winds at the zero order, $v^{(0)}_1(z,a,0)$, given by Eq. (1.39), with different values of δ. They are plotted with nondimensional units.

Of interest is that the solution (1.39) shows the strong dependence of growth rate on the vertical structure of tangential wind. Indeed, if the e-folding time (τ_e) is defined from the exponent of the double exponential in (1.39) as $\tau_e = \ln\{\beta[W_0\lambda(1-\delta)]^{-1}\}/\beta$, we can see that the higher the level where the peak tangential flow (i.e., the larger δ) is located, the slower rate at which the TC vortex will grow at (i.e., the larger τ_e). In other words, a TC vortex with the peak tangential wind near the surface will amplify faster than one with the peak tangential wind located higher up. This is a result of the absolute angular momentum conservation (see Zhang et al. 2001). That is, it would take much shorter time for the SC to spin up a TC vortex through its radial and vertical advection of the absolute angular momentum if the peak rotational flow is located in the lowest inflow layer than a higher layer. The result suggests that the fastest growing mode will be the one with the tangential wind peaked at the surface where the inflow is maximized, i.e., the mode with $\delta = 0$. In nature, the peak tangential wind in rapid intensifying TCs is often observed near the top of the PBL. Thus, we may regard $\delta = 0$ as a mode for a frictionless vortex (e.g., in the free atmosphere), i.e., the zero-order solution $v_1^{(0)}(r,z,t)$. Note that the e-folding time also depends on the depth of the troposphere (through λ), the mean vertical motion, and static stability.

The first-order frictional correction $F^{(1)}(z,t)$ is governed by

$$\frac{\partial F^{(1)}}{\partial t} = -e^{\beta t}\left(H\frac{\partial F^{(1)}}{\partial z} + 2QF^{(1)}\right) - F^{(0)} \qquad (1.40)$$

Following the same procedures as that for the zero-order solution, and noting that $F^{(0)}(z,t) = -f/2 + F_h(z,t)$, the solution for $F^{(1)}(z,t)$ can be approximated as

$$F^{(1)}(z,t) = \frac{2G_1 W_0 \lambda}{\beta}\cos^2(\frac{\lambda z}{2})e^{-Sz}\frac{\exp(W_0\lambda e^{\beta t}/\beta) - \tan(\lambda z/2)}{W_0\lambda e^{\beta t}/\beta - \ln[\tan(\lambda z/2)]}, \qquad (1.41)$$

where G_1 is an integration constant to be determined later. Note that only the highest weighted (i.e., lower-order) contribution to $F^{(1)}(z,t)$ is included in (1.41) (see Appendix II).

Adding the zero- and first-order solutions yields the tangential wind in Region I:

$$v_1(r,z,t) = [F^{(0)}(z,t) + \kappa(z)F^{(1)}(z,t)]r \equiv K(z,t)r, \qquad (1.42)$$

where $K(z,t)$ is defined as

$$K(z,t) = 2G_0\cos^2(\frac{\lambda z}{2})e^{-Sz}\left[\exp(\frac{W_0\lambda}{\beta}e^{\beta t}) + \varepsilon\frac{\exp(W_0\lambda e^{\beta t}/\beta) - \tan(\lambda z/2)}{W_0\lambda e^{\beta t}/\beta - \ln[\tan(\lambda z/2)]}\right] - \frac{f}{2} \qquad (1.43)$$

and $\varepsilon = \kappa W_0\lambda G_1/\beta G_0$. Fig. 1.3 shows the vertical profiles of the zero-order solution (1.39) with $\delta = 0$, the first-order frictional correction (1.41) - mostly associated with the PBL effects, and the total solution (1.42) at four different instants of time. Obviously, the frictional boundary layer reduces the surface wind to near null, causing the peak wind located above the PBL (Fig. 1.3b). In general, the larger the frictional effects (i.e., the larger κ), the higher the level of the peak frictional correction will be located. Note that the frictional correction increases rapidly with time, and the level of its peak magnitude shifts slightly downward. A similar pattern is seen for the total tangential winds (Fig. 1.3c). In terms of the growth rate, however, the TC vortex tends to grow from the bottom up due to the fastest growing mode at the surface from the zero-order solution, as mentioned earlier. This result appears to provide an important theoretical insight into the dynamical behaviors of growing vortices during the TCG stage. Namely, the TC vortex tends to spin up from the

bottom upward as a result of the inward advection of the absolute angular momentum in the lowest inflow layer (Zhang and Bao 1996; Hendricks et al. 2004; and Montgomery et al. 2006).

To find $\phi_1(r,z,t)$ in Region I, substituting solutions for v_1, w_1, and u_1 into Eq. (1.20'), after some manipulations, gives

$$\frac{\partial \phi_1}{\partial r} = -(Q\beta e^{\beta t} + Q^2 e^{2\beta t} + He^{2\beta t}\frac{dQ}{dz} - K^2 - fK - Q\kappa)r\,. \quad (1.44)$$

A simple integration of (1.44) with respect to r leads to

$$\phi_1(r,z,t) = \Phi_a - (K^2 + fK - Q\beta e^{\beta t} - Q\kappa - Q^2 e^{2\beta t} - He^{2\beta t}\frac{dQ}{dz})\frac{(a^2 - r^2)}{2}, \quad (1.45)$$

where $\Phi_a(z)$ is the geopotential height perturbation at $r = a$ and it will be determined later with the geopotential height distribution in Region II.

b. Analytical solutions for Region II

Exact solutions for Region II can be derived using the same procedures as those for Region I. First, integrating the continuity equation (1.23'), with $w_2(r,z,t) = 0$, gives

$$u_2(r,z,t) = C_1(z,t) - \frac{C_2(z,t)}{r}, \quad (1.46)$$

where $C_1(z,t)$ and $C_2(z,t)$ are integral functions. Using Eq. (1.23) at $r = a$ and the boundary condition (1.25) yields $C_1 = 0$ and $C_2 = \frac{a^2}{2}(\frac{dH}{dz} - SH)e^{\beta t}$. So, the solution for the radial wind in Region II is

$$u_2(r,z,t) = -\frac{1}{2}(\frac{dH}{dz} - SH)e^{\beta t}\frac{a^2}{r} \equiv e^{\beta t}\frac{a^2 Q}{r}. \quad (1.47)$$

Substitution of u_2 into Eq. (1.21'), followed by some simple rearrangements, yields

$$\frac{\partial v_2}{\partial t} = -a^2 e^{\beta t}(\frac{Q}{r}\frac{\partial v_2}{\partial r} + \frac{Q}{r^2}v_2 + f\frac{Q}{r}) - \kappa v_2. \quad (1.48)$$

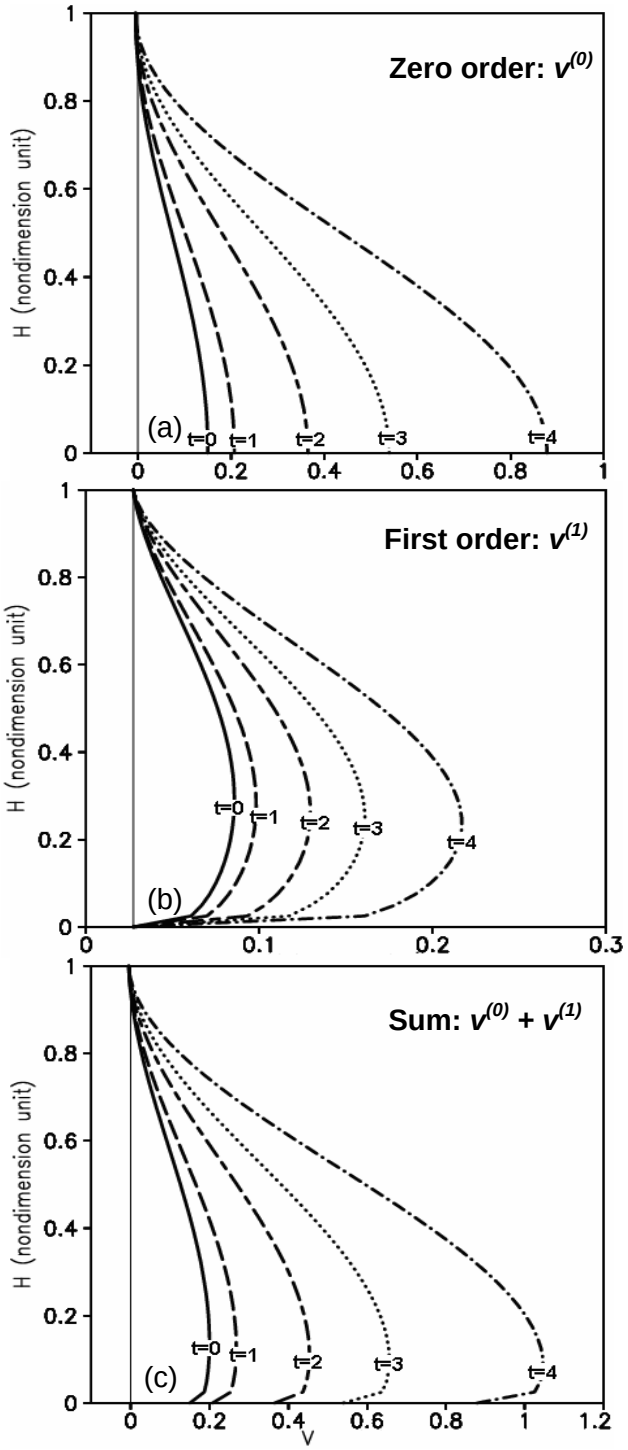

Figure 1.3. Vertical profiles of the mean tangential wind in Region I at four different times t = 0, 1, 2, 3, 4 for (a) the zero-order $v^{(0)}{}_1(z,a,t)$ given by (20); (b) the first-order frictional correction $v^{(1)}{}_1(z,a,t)$ given by (1.41); and (c) the sum of the zero- and first-order solutions given by (1.42). Note that $\delta = 0$ is required for the zero-order solution, and that all the parameters have been nondimensionized.

The only separable solution of (1.48) is of the form of $v_2(r,z,t) = F_2(z,t)/r$, so we have

$$\frac{\partial F_2}{\partial t} = -e^{\beta t} a^2 fQ - \kappa F_2. \tag{1.49}$$

Integrating it gives an explicit solution for the tangential wind in Region II:

$$v_2(r,z,t) = \left(\frac{-e^{\beta t} Qfa^2}{\beta + \kappa} + Ze^{-\kappa t}\right)/r, \tag{1.50}$$

where $Z(z)$ is an integral function of z that can be determined by matching $v_1(r,z,t)$ and $v_2(r,z,t)$ at $r = a$ and $t = 0$ as follows

$$Z(z) = \left(K + \frac{Qf}{\beta + \kappa}\right)a^2. \tag{1.51}$$

By plugging u_2, v_2, w_2 into Eq. (1.20'), we obtain

$$\frac{\partial \phi_2}{\partial r} = -\left(e^{\beta t} Qa^2 \frac{\beta + \kappa}{r} - e^{2\beta t} \frac{Q^2 a^4}{r^3} - \frac{C^2}{r^3} - \frac{fC}{r}\right), \tag{1.52}$$

where $C(z,t) = \left(\frac{-e^{\beta t} Qfa^2}{\beta + \kappa} + Ze^{-\kappa t}\right)$. Finally, integrating (1.52) gives the geopotential height perturbation in Region II:

$$\phi_2(r,z,t) = \Phi_0 + [e^{\beta t} a^2 Q(\beta + \kappa) - fC] \ln \frac{R_m}{r} - e^{2\beta t} \frac{a^4 Q^2}{2r^2} - \frac{C^2}{2r^2}, \tag{1.53}$$

where radius R_m and $\Phi_0(z,t)$ are defined such that $\phi_2|_{r=Rm} = 0$. All the solutions for the wind and mass fields in both Region I and II are thus derived completely.

One should keep in mind that the analytical solutions obtained above are more suitable for the growing stage during which the energy supply is assumed to be favorable for the full development of TCs. As the storms reach their maximum intensity, the feedback relation between vertical motion and diabatic heating (i.e., assumption iii) is no longer valid, so the time-dependent solutions cannot be further extended in time. In particular, there must be an upper limit for the mean upward

motion, which may be closely related to the MPI (Emanuel 1986; Holland 1997). Thus, we have to restrict the validity of the above growing solutions to a range of [0, T_m], where T_m is the shortest time at which the maximum mean upward motion is reached due to diabatic heating in the inner-core region.

3.3. Verification

In this section, we compare the above analytical solutions to some well-documented observations and model simulations in the literature (e.g., McBride 1981; McBride and Zehr 1981; Willoughby et al. 1982; Willoughby 1990; Liu et al. 1999). They are summarized as follows: (i) The TC flow is prevalently cyclonic throughout the troposphere and it becomes anticyclonic only in a thin layer near the tropopause; (ii) the tangential wind increases nearly linearly with radius until reaching the RMW and then decreases slowly to the ambient value at a very large distance; (iii) the tangential wind peaks near the top of the PBL and then decreases with height, especially near the RMW; and (iv) TCs grow at a much faster pace in the inner-core region than that in the outer region. Some other typical features may include (v) radial inflow and outflow at the low- and upper-levels, respectively; (vi) the peak vertical motion in the midtroposphere with a null value at the surface and the tropopause; and (vii) lower pressures (or geopotential heights) in the core region throughout the troposphere except in the upper layer where the horizontal winds become anticyclonic. Next, we will determine to what extent our analytical solutions could exhibit the above-mentioned features by looking at growth rates, 3D flow structures, 3D mass fields, and gradient wind approximation.

Growth Rates. A comparison of solutions (1.42) and (1.50) show clearly that the tangential wind in the inner-core region $v_1(r,z,t)$ grows at a rate much faster (due to

the double exponential factor) than that in the outer region $v_2(r,z,t)$, as listed by (i). Fig. 1.4 shows an example associated with Hurricane Diana (1984); See Willoughby (1990) for more TC cases. Evidently, the tangential wind within the RMW nearly doubles in magnitude in 24 hours whereas its outer-region magnitude exhibits a slow increase. Our solutions capture well this contrast in the growth rate between the inner-core and outer regions.

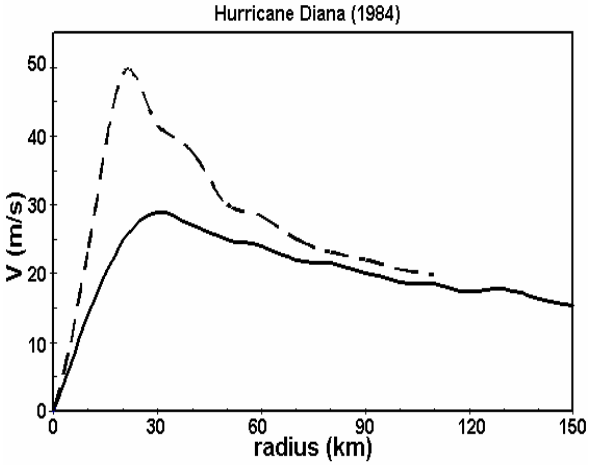

Figure 1.4. Growth of the 850-hPa tangential wind of Hurricane Diana (1984) that is valid during 2335 UTC 9 – 1514 UTC 10 September (solid); and 0228 UTC – 0903 UTC 11 September 1984 (dashed) [Reproduced from Willoughby (1990)].

Physically, this intriguing PC behavior in the inner-core region could be attributed to the radial-inward and upward advection of the absolute angular momentum. That is, the axisymmetry of TCs requires both the radial and tangential winds to vanish at the vortex center and in the far outer region. This implies that the tangential wind has to attain its maximum value somewhere near the core of the vortex (i.e., $r = a$ in our model). It follows that the radial inward advection in the PBL will help accelerate (decelerate) the PC in the inner-core (outer) region. In addition, the ascending motion in the inner-core region advects more angular momentum upward, further facilitating

the amplification of the TC vortex in the layers above. Thus, the dynamical impacts of the SC on the PC are of vital importance in determining the growth of TCs in addition to their usual thermodynamical roles (Emanuel 1986).

Now we describe how to quantify our analytical solutions with some observations. Since diabatic heating tends to be mostly offset by adiabatic cooling (see, e.g., Zhang et al. 2002), only the small difference between them [i.e., αw and $N^2 w$ in Eq. (1.24')] contributes to the warming of the inner-core region and the growth of TCs. As a result, we can choose $\beta \approx O(N^2) \approx 10^{-5}$ s^{-1} (Charney and Eliassen 1964), and $J_0 = 5\times10^{-5}$ m s^{-2} corresponding to an inner-core (π a^2) area-averaged heating rate of about 5^0C d^{-1} (see Schubert and Hack 1982). Given the values of β and J_0, the thermodynamical constraints of Eqs. (1.22') and (1.24') will give $W_0 = 0.02$ m s^{-1}. This is an acceptable value for the mean vertical motion within the cloud disk covering TCs at their early depression stage. If we assume the maximum tangential wind $V_{max} = 12$ m s^{-1} at $z = 1$ km and $a = 100$ km at t = 0 at this stage, solving Eq. (1.39) will give $G_0 = 2.5 \times 10^{-5}$ s^{-1}, and then solving Eq. (1.42) will yield $\varepsilon = 0.25$. To represent the strong damping effects in the frictional boundary layer, we use the drag coefficients of the form $\kappa(z) = \kappa_0 \exp[-(z/H_{PBL})^2]$, where $\kappa_0 = 2.5 \times 10^{-5}$ s^{-1}. This $\kappa(z)$ profile corresponds to a near-constant drag coefficient in the PBL (H_{PBL}) that decreases rapidly upward. All the other parameters were given in Table 1.

Results for two different heating rates are given in Fig. 1.5, which shows slow growth of the TC intensity at first and more rapid deepening at later times, corresponding to the early TCG and later hurricane stages, respectively. The maximal tangential wind nearly doubles its initial intensity in 2.5 day. If the heating rate is doubled, the maximum tangential wind can surge to 70 m s^{-1} in 2 days and the

deepening rate of the surface pressure during the final 2 hours could be as large as 15 hPa. Nonetheless, this deepening rate is even smaller than the observed hourly rate of 9 hPa associated with the record-breaking Hurricane Wilma (2005) which developed over a warm ocean surface in a weak-sheared environment. Clearly, such a large deepening rate could be related to a much greater heating rate in the

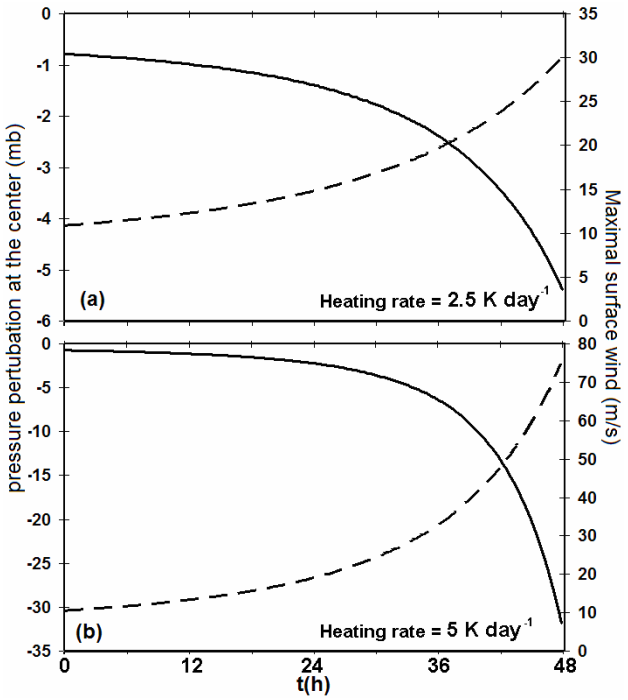

Figure 1.5. Time series of the minimum sea-level pressure (solid) and the maximum tangential wind (dashed) from solutions (1.45) and (1.42), respectively, for two different heating rates (a) $J_0 = 2.5$ K d^{-1}; and (b) $J_0 = 5$ K d^{-1}.

inner-core region. In reality, various factors such as vertical wind shear, horizontal deformation, cold sea-surface temperature, or friction will all tend to suppress TCG, thereby increasing the intensity doubling time.

The 3D flow structures. Solutions (1.42) and (1.50) show that the tangential wind increases linearly with radius for $r \leq a$ and decreases inversely with radius for $r > a$. This radial distribution fits well the familiar pictures of TCs even at the early stage (e.g., Willoughby 1990), as listed under (ii). More notably, the two solutions

show cyclonic flows in a deep layer in the troposphere and anticyclonic flows in a thin layer beneath the tropopause, as listed under (i). Fig. 1.6 shows an example of the vertical profile of the area-averaged tangential flow over the inner-core area as given by Eq. (1.42). Except for the slope of the theoretical tangential wind profile, which is steeper than the observations, the analytical solution shows a general consistency with a cyclonic flow dominating in the troposphere and a peak near the top of the PBL due to the inclusion of frictional effects. The physical reasoning for such a deep layer of cyclonic flow is again attributable to the roles of the SC in transporting the absolute angular momentum. Solutions (1.28), (1.29) and (1.47) also provide a consistent description of the SC with an inflow in the lower half, an outflow in the upper half of the troposphere, and the maximum vertical motion at the middle level (Fig. 1.7), as listed by (v) and (vi). The atmospheric stratification makes the inflow layer somewhat shallower than the outflow layer in the pseudo-height vertical coordinate, which is again expected from observations.

The 3D mass field. The observed bow shape of the geopotential height, listed by (vii), can be reproduced by solutions (1.45) and (1.53). To see this, we consider each half of the troposphere separately. Because $Q \approx - dH/dz$ is negative and $dQ/dz \approx - d^2H/dz^2$ is positive in the lower atmosphere, the first four (last two) terms inside the parenthesis of (1.45) will contribute positively (negatively) to the decrease of geopotential height at each level. Since $K(z,t)$ (Eq. (1.43)) is a very sensitive function of time (i.e., due to the double exponential factor), the first two terms in solution (1.45) containing K will become more dominant with time so lower pressures are guaranteed to develop in the inner-core region after a while. In contrast, in the upper half of the troposphere, $Q > 0$ and $dQ/dz < 0$. This implies that the positive

contributions of the first two terms, though decreasing with height, will be compensated by the negative contributions of the last four terms in the parenthesis of (1.45). Therefore, we may still expect to have lower pressures developed in the upper troposphere with time. Near the tropopause, however, *K* becomes very small due to its strong dependence on height [cf. Fig. 1.6 and Eq. (1.45)] so that a weak high-pressure system may be seen corresponding to an anticyclonic flow aloft.

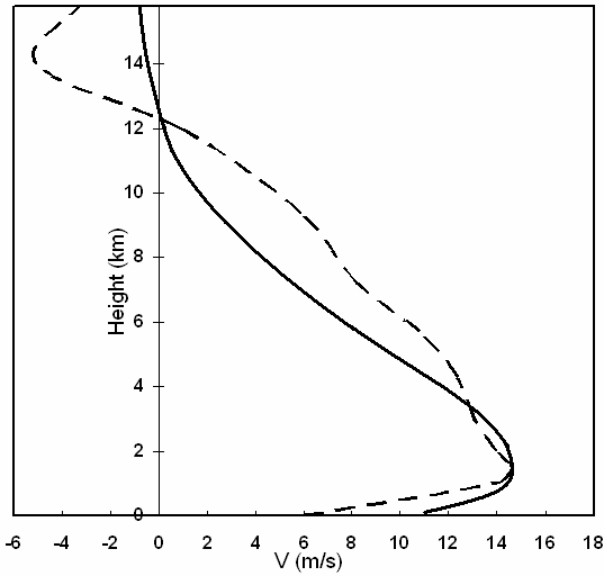

Figure 1.6. A comparison of the vertical profiles of the mean tangential wind estimated from Eq. (1.42) (solid) to the observed in West Pacific typhoons (dashed). The observed profile is reproduced from McBride (1981).

Gradient wind approximation. Since the gradient-wind approximation has been widely accepted in the previous TC studies, it is of interest to see how well this balance relation is represented in our analytical solutions. This can be done simply by deriving the geopotential height perturbation from the gradient wind balance, i.e.,

$$-\frac{v^2}{r} = -\frac{\partial \phi_b}{\partial r} + fv, \tag{1.54}$$

and then comparing it with the solutions (1.45) and (1.53). Substituting tangential

wind $v_1(r,z,t)$ and $v_2(r,z,t)$ into Eq. (1.54) will yield ϕ_b for Region I and II, separately. For example, a comparison of the balanced geopotential height ϕ_b with solution (1.45) for Region I gives

$$\left|\frac{\phi_1-\phi_b}{\phi_1}\right| \cong \left|\frac{\phi_1-\phi_b}{\phi_1}\right|_{t=0} \times \left[\frac{\cos(\lambda z)}{\cos^2(\lambda z/2)}\frac{e^{2\beta t}}{\exp(W_0\beta e^{\beta t}/\lambda)}\right]^2. \quad (1.55)$$

Eq. (1.55) shows that no matter how large the difference is between the exact solution and the gradient-wind approximation at the initial time is, the relative difference will approach zero because the denominator increases rapidly with time. Therefore, the gradient wind balance is expected to be a better approximation at the later stages. The gradient balance relation should be more easily satisfied in the outer region.

3.4. Applications

In this section, we shall demonstrate how our analytical solutions could be used to construct bogused vortices for initializing TC models and to derive the functional dependence of the central pressure on maximal tangential wind that has been shown previously to be useful in case of missing observations.

a. Initialization of TC models

Some TC models (e.g., the WRF and MM5, the Fifth-Generation NCAR/Penn State Mesoscale Model) are currently initialized with an axisymmetric (Rankine) vortex prescribed arbitrarily by a vertical weighting function (e.g., Yang et al. 2008). Even in the GFDL operational hurricane model (see Kurihara et al. 2003), an *ad hoc* vertical weighting function must be used to obtain the vertical distribution of tangential wind. Moreover, in many cases, only the PC is initialized, and one has to rely on the TC models to adjust or spin up realistically the 3D vortex flows. The

analytical solutions presented herein provide an alternative way to construct the 3D flow and mass fields of TCs, if a top-hat heating distribution plus some observations of the tangential wind at any level (e.g., from flight reconnaissance) are available. All one has to do is to set t = 0 in solutions (1.28), (1.29), (1.42), (1.45), (1.47), (1.50), and (1.53), thus yielding the 3D fields of *w, u, v*, and ϕ in both Region I and II. As indicated by Eqs. (1.20') – (1.24'), our solutions provide more complete and dynamically consistent 3D distributions for both the PC and SC. Specifically, tangential wind at t = 0 is given by

$$v_1(r,z,0) = K(z,0)r, \qquad \text{for r} \le \text{a}$$

$$v_2(r,z,0) = (-Qfa^2/\beta + Z)/r, \qquad \text{for r} > \text{a}$$

where *Q(z)*, *Z(z)*, and *K(z,t)* are defined in section 3.3. The geopotential height perturbation is given by

$$\phi_1(r,z,0) = \Phi_a - (K^2 + fK - Q\beta - Q^2 - H\frac{dQ}{dz})\frac{(a^2 - r^2)}{2}, \text{ for r} \le \text{a}$$

$$\phi_2(r,z,0) = \Phi_0 + a^2Q(\beta + \kappa - fC)\ln\frac{R_m}{r} - \frac{a^4Q^2}{2r^2} - \frac{C^2}{2r^2}, \qquad \text{for r} > \text{a}$$

where $C(z,t)=(\frac{-e^{\beta t}Qfa^2}{\beta+\kappa} + Ze^{-\kappa t})$, $\Phi_0(z) = (a^4Q^2 + C^2)/R^2{}_m$, and $\Phi_a(z) = \phi_2(a,z,0)$.

The radial wind is given by

$$u_1(r,z,0) = Qr \quad , \qquad \text{for r} \le \text{a}$$

$$u_2(r,z,0) = a^2Q/r. \qquad \text{for r} > \text{a}$$

The vertical motion is given by

$$w_1(r,z,0) = W_0 sin(\lambda z), \qquad \text{for r} \le \text{a}$$

$$w_2(r,z,0) = 0. \qquad \text{for r} > \text{a}$$

The buoyancy (or temperature perturbation) is given by

$$b_1(r,z,0) = \beta W_0 \sin(\lambda z), \qquad \text{for } r \le a$$

$$b_2(r,z,0) = 0. \qquad \text{for } r > a$$

The above 3D vortex structures appear at first to contain too many free parameters (e.g., β, λ, κ_0, W_0, R_m, S). However, most of these parameters are nearly constants and suitable for all of the TCs so they only need to be evaluated once (see Table 1). Some case-dependent parameters in the above solutions are the area-averaged maximum vertical motion (W_0), RMW (a), the Coriolis parameter (f), and the frictional correction (ε). The first two parameters W_0 and a can be estimated from (1.22') and (1.24') once the diabatic heating rate profile is observationally available. Such heating profile appears to be feasible with today's observing platforms. Specifically, satellite retrieval algorithms, based on precipitation-rate profile retrievals, have recently been developed to estimate the vertical distribution of latent heating in TCs using Special Sensor Microwave Imager (SSM/I) and Tropical Rainfall Measuring Mission (TRMM) microwave imager measurements (e.g., Rodgers et al. 1998, 2000; Tao et al. 2006). With a numerical approach, Zhu et al. (2004) developed an algorithm to initialize TC vortices using the temperature (or heating) profiles retrieved from the Advanced Microwave Sounding Unit (AMSU-A) data. Parameters G_0 and ε can be calculated from (1.3.23') in the same way as that described in section 3.4, using an observed V_{max} at its corresponding altitude.

Fig. 1.7 shows an example of a TC vortex using the parameters given in Table 1, W_0 = 0.02 m s^{-1}, G_0 = 5.5 × 10^{-5} s^{-1}, and ε = 0.3 (the last two parameters are evaluated from Eq. (1.3.23') with an assumed value V_{max} = 30 m s^{-1} at z = 1 km, a = 100 km). It is apparent that except for small sharp changes at $r = a$ due to the first-

order matching of Eq. (1.51), the TC flow structures are reasonably constructed with the cyclonic winds decreasing upward and outward. Note particularly again that the time dependence of the above solutions shows that the higher the level of the maximal tangential wind, the slower the vortex will grow (cf. Fig. 1.2). Moreover, this peak will shift downward with time during the development of the vortex due to the rapid growth of the leading order at the surface (cf. Fig. 1.3). Therefore, one should be cautioned with the practical construction of the 3D vortex because different heights of the maximal tangential wind, which is controlled by the parameter ε in our model, will correspond to different stages of TC development and could impact to the subsequent growth rate of the vortex.

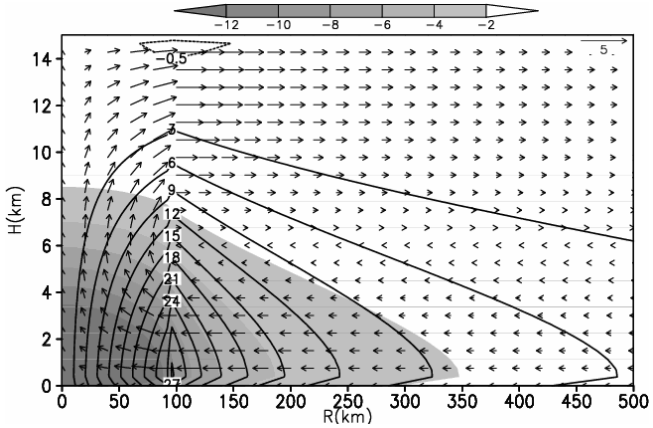

Figure 1.7. Radius-height cross section of the tangential wind (contoured) at intervals of 3 m s^{-1} and pressure perturbations (shaded at intervals of 2 hPa), superimposed by in-plane flow vectors, as constructed from the analytical solutions obtained in section 3.

The same procedures may be used to construct the 3D flow fields for a mature hurricane with diabatic heating in the eyewall. In this case, a smaller value of β may be assumed such that the storm would grow slowly during this stage. The vertical and radial structures, nonetheless, will not be much changed, except for vertical motion,

because we have to eventually take the limit of μ such that the tangential wind is finite at $z = 0$. This will be one of the objectives of our forthcoming work. Note, though, that due to the use of a top-hat heating function, there are some discontinuities in the solutions for the tangential wind at $r = a$ as the TC vortex intensifies with time. This type of discontinuities could be eliminated if one uses a smoother heating function, as shown by Hack and Schubert (1986).

b. The central pressure and maximum wind relationship

One of the important issues in reconstructing a hurricane database is how to obtain a faithful surface pressure-wind relationship (PVR). Such relationship is especially useful for early data archive where either the minimum sea-level pressure or the maximum surface wind is missing or the pressure and wind data over different basins are not consistent. Much of the past effort has focused on obtaining functional forms of PVR, often based on some physical arguments for choosing a set of recursive parameters (e.g., Atkinson and Holliday 1977; Knaff and Zehr 2007). An asymptotic PVR, based on the gradient-wind-balance relation, was presented by Knaff and Zehr (2007) and it is given by

$$\delta p_{\min} = P_{env} - MSLP = A_1 (V_{\max})^2 + A_2 V_{\max} + A_3 S + A_4 \Phi_L + A_5, \qquad (1.56)$$

where P_{env} is the environmental pressure, S is the translation speed, and Φ_L is latitude. The coefficients A_1 to A_5, varying from basin to basin, are obtained from the least-square fit with a set of the best track data.

Here we wish to show that our exact solutions can provide a dynamically consistent PVR at the surface or any level above. To this end, we set $r = 0$ in Eq. (1.45) to obtain $\phi_{\min}$, and $r = a$ in solution (1.42) to obtain V_{max} both at any level. Eliminating $e^{\beta t}$ from the two expressions, and noting that $\delta p_{min} = \rho \phi_{min}$, will give the

following PVR at $z = 0$

$$\delta p_{\min}(t) = \frac{\rho}{2}(V^2{}_{\max} + faV_{\max}) + \Lambda_1 \ln(\frac{2V_{\max} + fa}{4aG_0}) + \Lambda_2 \ln^2(\frac{2V_{\max} + fa}{4aG_0}) + \Lambda_3 \quad (1.57)$$

where the coefficients Λ_1, Λ_2, and Λ_3 are given by

$$\Lambda_1 = \frac{\beta Q}{W_0 \lambda}[\beta - a^2(\beta + \kappa)\ln\frac{R_m}{a}]$$

$$\Lambda_2 = \frac{\beta}{W_0 \lambda}[\frac{a^2 Q^2}{2}\left(1 - \frac{a^2}{R_m{}^2}\right) - Q^2 - H\frac{dQ}{dz}]$$

$$\Lambda_3 = Q\kappa\frac{a^2}{2} + \frac{C^2}{2}\left(1 - \frac{a^2}{R_m{}^2}\right) - fC\ln\frac{R_m}{a}$$

Apparently, relationship (1.57) shows the dependence of δp_{min} on V_{max} that is similar to that of Eq. (1.56) only when V_{max} becomes very large such that the first two terms on the rhs of (1.57) dominate. However, when V_{max} is small, the other three terms in (1.57) are not negligible, and they will contribute to the overall magnitude of δp_{min}. The different dependence from that in (1.56) occurs because our analytical solutions have included the other nonlinear terms in the horizontal momentum equations, rather than just the simple gradient wind equation. Although coefficients Λ_i are somewhat oversimplified due to the use of various assumptions herein, the functional form (1.57) actually provides a broader framework in deriving a more appropriate PVR using the statistical approach. Indeed, with a set of the observed δp_{min}, V_{max}, and RMW, the least square fit with (1.57) could yield a set of more reasonable recursive values for Λ_i.

3.5. Discussions

In this study, a theoretical model for TC development in response to an external heating source is revisited from an analytical perspective, using the full horizontal

momentum equations. By introducing the positive feedback between the vertical motion and buoyancy, the primitive equations can be divided into two subsystems: one associated with the vertical motion and buoyancy, and the other for the radial and tangential wind and geopotential height. This partitioning allows us to solve for the nonlinear primitive equations analytically with a top-hat heating function. It is demonstrated that the PC (or TC intensity) can be derived exclusively from a given SC (or heating distribution). This approach differs radically from the previous quasi-balanced studies in which the PC has to be *a priori* assumed to estimate its associated SC. The exact solutions so obtained exhibit a double-exponential growth of the rotational flow in the inner-core region consistent with observations, which to our knowledge has not been shown by previous studies. The solutions contain many important dynamical aspects of TCs, as verified against well-documented observations, including the three-dimensional structures and evolution as well as the intensity and growth of TCs from the early genesis to hurricane stages. Results show that the lower the level of the peak tangential wind, the faster the TC will grow. This is a consequence of the radial advection of the absolute angular momentum in the lowest inflow layer, and it helps explain why the rotational flow tends to grow from the bottom upward.

While the nonlinear terms in the thermodynamic and vertical motion equations, i.e., Eqs. (1.22') and (1.24'), are ignored to avoid the enormous complications related to thermodynamical processes, we should point out that the exact solutions for the PC do not depend critically on this assumption. One may start simply with solution (1.28) for w and all the subsequent derivations presented herein will be preserved. After all, few approximations have been made in the horizontal momentum and continuity

equations in our model.

The analytical solutions obtained herein are shown to be useful for constructing the 3D TC vortex for the initialization of TC models when the mean diabatic heating or the mean vertical motion can be approximated by top-hat profiles. Only a few case-dependent parameters need to be specified from observations. A key difference from the previous bogussing technique is that our vortex initialization does not require *a priori* specification of the structure of the rotational flows. We have also shown that the exact solutions provide a dynamically consistent functional relationship between the central pressure and maximal tangential wind at any level, facilitating the statistical analyses of TC intensity to overcome the obstacle posed by missing data.

It should be pointed out that due to the neglect of nonlinear terms in Eqs. (1.22') and (1.24'), the analytical solutions may not be valid when the mean vertical motion of TC becomes strong. In our future research, we will explore the effects of including all the nonlinear terms in the above two equations and using different heating functions on the 3D structures but through a numerical modeling approach.

PART II. A NUMERICAL STUDY OF TROPICAL CYCLOGENESIS

Chapter 4. Introduction

4.1. Background

Of the four TC development phases, TCG is the most difficult period to predict by numerical TC models and operational forecasters. While the newly developed theoretical model for TC development proposed in Part I sheds some insights into the growth rate as well as the structure of axisymmetric vortices, the realistic cyclones often show a much more complicated interaction with the surrounding environment, such as vertical wind shear, SST anomalies, or other atmospheric inhomogeneities. Such environmental factors have been neglected in our analytical model as they are typically asymmetric and difficult to predict, thus rendering the problem extremely challenging that analytical solutions may not exist at all. In this aspect, numerical studies provide us an invaluable tool to look detailed into the evolutions as well as structure of TCs realistically.

Despite the many processes involved during TCG, the recent successes of global models in predicting TC tracks indicate that the large-scale circulation is the key parameter in determining where TCG may occur. It is well known that the large-scale conditions conducive for TCG over different ocean basins include weak vertical wind shear (Gray 1968; McBride and Zehr 1982; DeMaria 1996), warm SST and deep moist layers (Emanuel 2000), well-organized angular momentum fluxes (Challa and Pfeffer 1990), easterly waves (Molinari et al 2000), active Madden-Julian Oscillations, and unstable background flows (Molinari et al. 1997). Some large-scale

influences on TCG, such as monsoon troughs, upper-level troughs, cold surges, elevated dust layers, and topographical effects, may be more relevant over one ocean basin than the others.

Although TCG may be mostly dictated by large-scale dynamics, recent observational and modelling studies show growing evidence of the important roles of mesoscale convective vortices (MCVs) in promoting TCG. The bottom-up and top-down hypotheses have been proposed as two of the possible processes leading to TCG from MCVs that often develop in the stratiform region of mesoscale convective systems (MCSs) (Zhang and Fritsch 1987; Bartels and Maddox 1991). Specifically, Zhang and Bao (1996a,b) find that an MCV provides the necessary quasi-balanced forcing for the initiation and organization of (parameterized) deep convection and for the initial concentration of the low-level cyclonic vorticity, and that it is deep convection that contributes to the amplification of the low-level cyclonic vorticity through stretching in the presence of intensifying flows. The associated absolute angular momentum is then advected upward by convective updrafts to intensify the cyclonic flows above (see Zhang et al. 2001).

This bottom-up mechanism was later advanced by cloud-resolving studies of Hendricks et al. (2004) and Montgomery et al. (2006), in which the concept of convective "hot towers" proposed by Riehl and Malkus (1958) was extended to that of "vortical hot towers (VHTs)" due to the development of intense cyclonic vorticity in convective cores. In their bottom-up hypothesis, Montgomery and Enagonio (1998) consider TCG as a result of the mean–eddy interaction, the so-called axisymmetrization. That is, a midlevel MCV provides necessary cyclonic background rotation at the low levels, and a set of vorticity anomalies associated with VHTs

contribute to the acceleration of the mean vortex through merging with neighboring VHTs and subsequent axisymmetrization. Montgomery and Kallenbach (1996) show that axisymmetrization can spin up a mean vortex even in a non-divergent barotropic model.

In contrast, the top-down hypotheses deal with two different scenarios: one is related to the merging dynamics of midlevel MCVs within a larger-scale low-level cyclonic background (Ritchie and Holland 1997, hereafter RH97; Simpson et al. 1997) whereas the other focuses more on the thermodynamics of a single MCV (Bister and Emanuel 1997). In the former case, merger of midlevel MCVs will accompany the downward extension of cyclonic vorticity due to the increase of the penetration depth and horizontal vortex size, leading to the amplification of surface rotation. In the latter case, the top-down hypothesis relies on the evaporative cooling as a mean to advect the midlevel MCV downward and replace the anticyclonic circulation near the surface. TCG occurs as soon as the WISHE process is initiated.

While TCG could occur over all tropical warm ocean basins, the eastern Pacific appears to experience the highest density of TCG events (Gray 1968). In the view of operational forecasters, many eastern Pacific TCs could be traced back to African easterly waves that propagate across the Atlantic and Central America and then into the eastern Pacific (Avila and Pasch 1992). Numerous studies showed that the eastern Pacific TCG could occur in association with MCSs (Bister and Emanuel 1997), easterly waves in the Inter-Tropical Convergence Zone (ITCZ, Molinari et al. 2000; Dickinson and Molinari 2002), and the interaction of easterly waves with the Central American mountains (Zehnder et al. 1999). Satellite observations revealed that the ITCZ may sometimes undulate and break down into a series of mesoscale

disturbances or MCVs, some of which may grow into TCs (Agee 1972; Hack et al. 1989; Wang and Magnusdottir 2006, hereafter WM06). Theoretical studies indicated that the ITCZ breakdown and its subsequent polarward rollup are closely related to the Charney-Stern (1962; i.e., combined barotropic and baroclinic) instability, and they could also be triggered by propagating easterly disturbances (Nieto Ferreira and Schubert 1997, hereafter as NS97; WM06).

A recent statistical study of TCG over the Eastern Pacific during the active seasons of 1999-2003 shows that most of the TCG events in this ocean basin are associated with the ITCZ breakdowns caused by easterly propagating tropical disturbances (WM06). While the ITCZ breakdowns could be attributed to the internal dynamical instability, the so-called roll-up mechanism discussed by NS97, WM06's study appears to suggest that merging MCVs associated with the ITCZ breakdowns are more efficient in generating mesoscale disturbances of tropical depression strength and initiating the TCG processes.

In spite of many important findings in the previous studies, few have examined multiscale processes involved in TCG over eastern Pacific and the other ocean basins. In particular, the exact nature of the interactions among the ITCZ, easterly disturbances or MCVs, vertical wind shear (VWS), cloud clusters, orography and TCG still remains elusive because of the lack of high-resolution, quality data over tropical oceans. For this reason, NASA conducted the Tropical Cloud System Processes (TCSP) field campaign in July 2005 using various state of the art observing systems, including aircraft measurements and satellite observations (Halverson et al. 2007).

4.2. The TCSP field experiment

The Tropical Cloud Systems and Processes (TCSP) mission is a field research investigation sponsored by the Science Mission Directorate of the National Aeronautics and Space Administration (NASA). The field experiment was from 1 July to 31 July 2005 in Costa Rica, an area that has the highest frequency of tropical cyclone genesis per unit area in the world (Halverson et al. 2006). TCSP is conducted mainly for studying the dynamical and thermodynamical aspects of precipitating cloud systems as well as TCs using aircraft, GOES satellite, and surface remote sensing instrumentation. TCSP was also supported by NOAA's Hurricane Research Division (HRD) and the National Meteorological Institute (IMN) of Costa Rica in gathering humidity and water vapor measurements from the convective through synoptic scales. The data obtained will be used to study 1) TC structures, genesis, intensity change, moisture fields and rainfall; 2) satellite and aircraft remote sensor data assimilation and validation studies pertaining to TC development; and 3) the role of upper tropospheric/lower stratospheric processes governing TC outflow, the response of wave disturbances to deep convection and the evolution of the upper level warm core.

There is a large collaboration among hurricane researchers and modeling community who use the WRF model and ensemble-based data assimilation techniques to investigate the dynamics of TC formation. The goals of research teams are to use the data collected from the TCSP experiment to understand the initiation of mature convective systems, how they transform to warm-core systems and their lifecycle, the potential of ensemble-based assimilation for tropical cyclones and remotely sensed observations. NCAR has also conducted real-time high-resolution forecasts for the TCSP field experiment.

The TCSP project has completed its mission successfully with valuable data collected from Hurricane Denis (4-10 July), Tropical Storm Gert (23-25 July), Tropical Storm Eugene (18-21 July), and Hurricane Emily (19-22 July). Of the four, Tropical Storm Eugene is the one that the pre-genesis phase was the least recorded (Halverson et al. 2005).

4.3. Objectives

Even in the most idealized case of axisymmetric TCs with the helps of scaling simplifications, it is still exceedingly challenging to solve for the exact solutions of the system of Eqs (1.1) - (1.5) analytically, especially for the real TCs with highly asymmetric environmental factors. The theoretical model presented in Part I focuses mostly on the rapid intensification from early TD to TS stage with the assumption that there exists initially a weak vortex of TD strength. The next issue is how such initial vortex is formed in the real atmosphere, and this will be the main subject of the numerical study in Part II. The purposes of this numerical study are to

- document the full life cycle of a TS from its pre-genesis to dissipation stages over a period of 11 days;
- investigate TCG from merging MCVs associated with the ITCZ breakdowns, and examine the kinematics of the vortex merger in relation to convectively generated vortices (CGVs) in the ITCZ and the associated multiscale interactive features;
- understand quantitatively how merger of the two midlevel MCVs could account for the formation of TS Eugene (2005) through the PV and vorticity budgets;
- examine whether the low-level cyclonic vorticity during the present TCG case

would occur from the bottom upward or the top downward; and

- study the impact of VWS and other processes on the structural changes in precipitation and vertical motion, the genesis and subsequent dissipation of the storm.

This will be achieved by using the National Centers for Environmental Prediction (NCEP) $1^o \times 1^o$ reanalysis and satellite data and performing 4-day (i.e., 0000 UTC 17 – 21 July 2005) cloud-resolving simulations of the life cycle of TS Eugene (2005) during the TCSP field campaign using the Weather and Research Forecast (WRF-ARW, V2.1.2) model with the finest grid size of 1.33 km. While studying TCG from a single case of TS Eugene may pose some questions of the validity of the findings in general, it is worth mentioning that there are currently few cloud-resolving numerical studies of cyclogenesis associated with 3D vortex merger in relation to the ITCZ breakdown,. Such 3D midlevel vortex merger is believed to be much more complicated and provide richer information than the simple merger from the 2D barotropic modelling studies. Therefore, results obtained from this case study will contribute toward a further understanding of TCG, specifically related to the ITCZ breakdown in Eastern Pacific. With the use of the PV dynamics equation as guidance and model outputs as verifications before detailed analyses are presented, it is expected that our findings can be applied for other cases of TCG associated with vortex merger in general.

Chapter 5. The control simulation

In this chapter, we first provide in section 5.1 some brief descriptions of the Weather Research and Forecast (WRF) model that will be used in this numerical study. An overview of Tropical Storm Eugene (2005) and the models setups will be given in sections 5.2 and 5.3, respectively. In section 5.4, some verifications of the model simulation will be presented to ensure that the model simulation is reasonable before further analyses are presented in Chapter 6.

5.1. WRF model

The WRF model has been developed and continuously improved for the past few years with the purposes of migrating to a new generation of numerical models for both operational applications and researches (see http://www.wrf-model.org/). The WRF model inherits the strengths while eliminates the drawbacks of previous numerical weather prediction (NWP) models. It is expected to compete with the current mature NWP models such as MM5, ETA, etc., in computational efficiency as well as accuracy and aims particularly at the expandability and portability on various platforms. The WRF model is developed and supported by NCAR's Mesoscale and Microscale Meteorology Division (NCAR/MMM), NCEP's Environmental Modeling Center (NCEP/EMC), and NOAA/FSL. Currently, there are two different versions of the WRF model: Advanced Research WRF (WRF-ARW) and Non-hydrostatic Mesoscale Model WRF (WRF-NMM), which were developed and maintained by NCAR/NMM Division, and NOAA/NCEP/EMC, respectively. The two versions share the same physical and software architecture but differ in the dynamical cores: the WRF-ARW employs staggered C-grid, whereas the WRF-NMM uses staggered

E-grid on hybrid coordinates. The latter is believed to better simulate baroclinic and nonlinear processes, which may be a problem with the C-grid in wave spectrum. In the meantime, NCEP is developing another version of the WRF applied specifically to hurricane researches (called HWRF), which incorporates the advantages of E-grid. The HWRF will be released in the near future. The latest version of the WRF-ARW model is V3.0, which supports 2-way interaction, movable nesting, and the latest version of the WRF-NMM is V3.0. The main features of these two versions of the WRF model include:

The WRF-ARW (V3.0)

- Fully compressible, nonhydrostatic with hydrostatic options
- Two-way movable nesting (manually or vortex-following automatically), one-way nesting option is also available
- Vertical spacing can vary with height (terrain following coordinates)
- Arakawa C-grid
- Runge Kutta 2^{nd} and 3^{rd} order split explicit time differencing
- Scalar-conserving flux form for prognostic variable
- 2^{nd} and 6^{th} order advection schemes
- Time-split, small steps for acoustic and gravity waves
- Four map projection options: Lambert, Conformal, Polar, and latitude-longitude (which can be rotated)
- Versatile microphysics options including Kessler, WRF Single Moment (WSM) 3, 5 and 6 class, Lin et al., Eta Ferrier, Thompson, Goddard 6 class, and Morrison 2-moment schemes
- Full physics options for land-surface, PBL, radiation, and cumulus

parameterization

- Unified (global/regional, multi-model, 3/4D-Var) model-space variational data assimilation system (WRF-Var)

The WRF-NMM (V3)

- Arakawa E-grid
- Terrain-following hybrid coordinates (combination of sigma and pressure)
- Explicit time differencing
- Conserve mass, kinetic, enstrophy and momentum
- Share the same parameterization schemes with WRF-ARW
- No nested grids in V3
- Map projection is in rotated latitude-longitude coordinates
- Capable of running on various platforms

The WRF user community is growing rapidly and new modules for physical processes are being developed and will be incorporated soon. The WRF model is suitable for a broad range of applications including idealized simulations of squall lines, baroclinic instability, parameterization research, real-time data assimilation, real-time forecasts, coupling with other models or educational purposes. The WRF has capability of simulating phenomena with a large range of scales from meters to thousands of km.

5.2. Overview of Tropical Storm Eugene (2005)

According to the official report of the National Weather Service/National Hurricane Center, TS Eugene (2005) had its origin from a traveling tropical wave entering the Caribbean Sea on 10 July 2005. However, multiple MCVs and vigorous convective activities within the ITCZ make the report questionable. The Hovmöller

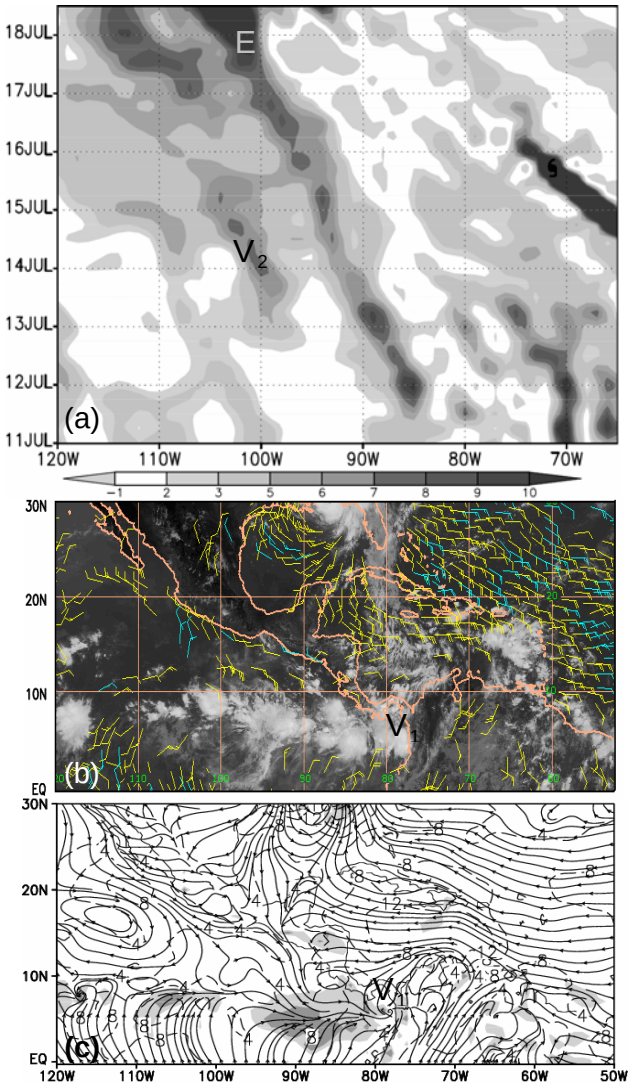

Figure 2.1. (a) Hovmöller diagram of the vertical absolute vorticity (unit: 10^{-5} s^{-1}) at 850 hPa during the period of 0000 UTC 11 - 1200 UTC 18 July 2005 and the longitudinal span of 120^0 – 65^0W that is obtained by meridionally averaging 3 slices (i.e., 3^0) of NCEP's reanalysis following V_1's center, starting at 8^0N; (b) *GOES-10/12 CIMSS* images of clouds, superimposed by the low-level winds valid at 0000 UTC 11 July 2005; and (c) NCEP's reanalysis of the 850-hPa streamlines (solid), isotachs (dashed, every 2 m s^{-1}), and relative humidity (shaded for 85% and 95%). Letters, "V_1" and "V_2", denote the two MCVs associated with the formation of TS Eugene (shown as "E"); similarly for the rest of the figures. Hurricane symbol marks the evolution of Emily (2005). Note that V_2 does not exist before 0000 UTC 13 July.

diagram of the 850-hPa relative vorticity field (Fig. 2.1a), satellite imageries (Fig. 2.2), and the model simulation to be presented in Chapter 7, show that Eugene, denoted by letter "E" after it was upgraded to TD, was actually growing out of two merging MCVs: a southeasterly disturbance or MCV initiated before 0000 UTC July 11 on the eastern end of the ITCZ offshore of Costa Rica (near 8^0N, 79^0E; see Figs. 2.1b,c), and an MCV spawned from the ITCZ on July 13 and about 1000 km to the west, hereafter referred to as V_1 and V_2, respectively (Fig. 2.1a). The associated TS watch, which appeared to be based just on the evolution of V_1, was first issued at 1500 UTC 18 July and about 200 km to the south of Manzanillo, Mexico. Speculating the possibility of the formation of a TC within this active area, the TCSP team conducted several experiments with NASA's ER-2 and NOAA's P-3 mission aircraft during the pre-genesis stage (July 15 - 16). Even though at many instances the aircraft captured several midlevel MCVs and deep convective towers in the ITCZ, the area covered by the aircraft (i.e., 5^0 - 11^0N, 91^0 - 85^0W) was nonetheless at the southeast of the actual region where Eugene developed (i.e., 9^0 - 14^0N, 104^0 - 99^0W). In addition, the precursor for Eugene was not well defined at this flight time (see Halverson et al. 2007, and Fig. 2.1 herein).

While V_1 could be traced back up to 7 days before Eugene's depression stage (Fig. 2.1), NCEP's $1^0 \times 1^0$ resolution reanalysis does not indicate any connection of V_1 to any propagating easterly wave with typical wavelength of 2000 - 3000 km from 0000 UTC 11 to 0000 UTC 16 July 2005. Instead, several MCVs entered Caribbean Sea during this period but they did not survive after propagating across the Central American continent. Both satellite and NCEP's reanalysis show that V_1 appeared to be related to one of the ITCZ breakdown episodes at 0000 UTC 11 July

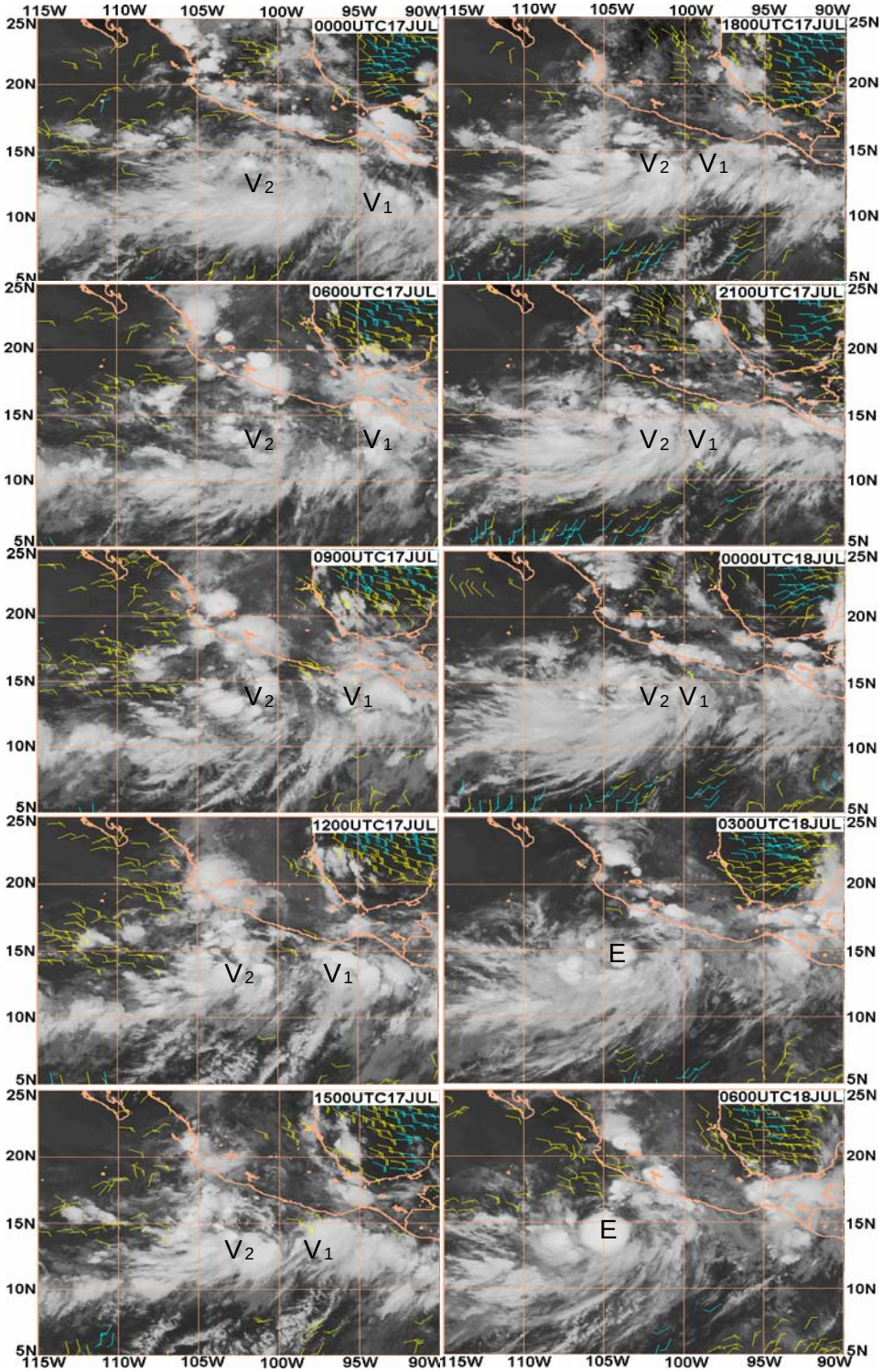

Figure 2.2. *GOES-10/12 CIMSS* images of clouds, superimposed by the low-level winds, from 0000 UTC 17 to 0000 UTC 21 July 2005. More frequent timeframes are shown during the period of 0600 UTC 17 – 0900 UTC 18 July in order to show better the merger of V_1 and V_2.

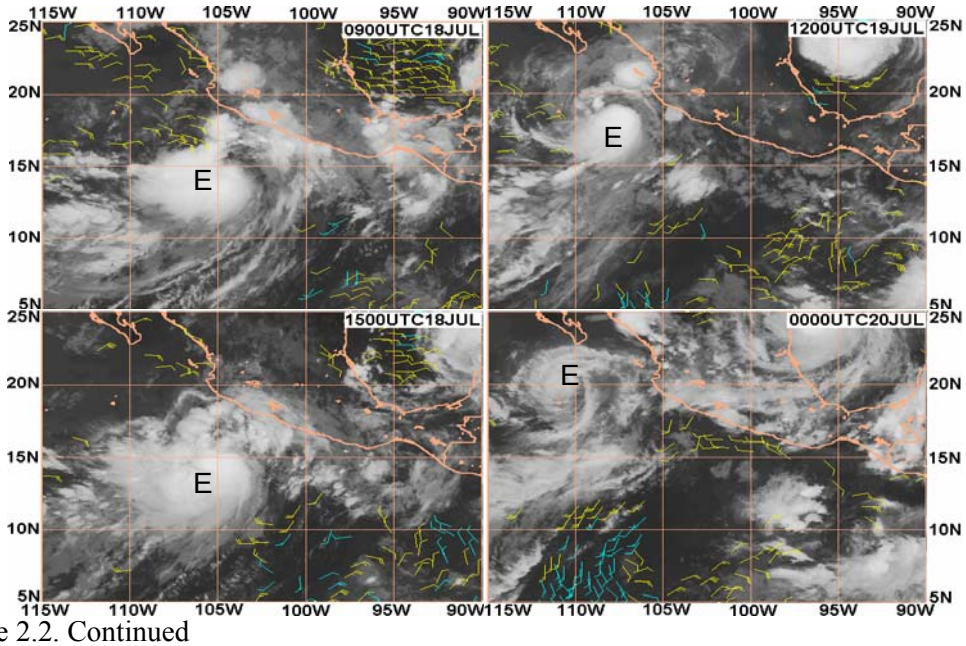

Figure 2.2. Continued

(Figs. 2.1b, c). However, it could not be further back traced due partly to its relatively small scale and partly to its weak intensity. One may note from Fig. 2.1a, plotted from the 6-hourly NCEP reanalysis, that Eugene looks as if it were grown out of V_1. But the 3-hourly satellite images show that the V_1-related cloud system, exhibiting rotational "solid" cloud signatures during the period of 0600 – 1500 UTC 17 July, shrank in size although it kept intensifying as it moved at a mean speed of about 3.3 m s^{-1} offshore along the Mexican coast under the influence of southeasterly flows plus the earth curvature (β) effect (see Li and Wang 1994). In contrast, V_2 moved at a speed similar to V_1 during the first 3 days after its formation, but it was quasi-stationary zonally after 0000 UTC 16 July (Fig. 2.1). Rather, V_2 began to move slowly northward as the rollup of the ITCZ. The V_2-related cloud system exhibits better mesoscale organization and more distinct rotation than V_1 at 0000 UTC 17 July, and then it expanded in size but likely weakened during its northward displacement. Both V_1 and V_2 possessed a comparable size and organization at 0600

UTC 17 July. It appears to be their subsequent merger (i.e., from 2100 UTC 17 to 0600 UTC 18 July) that caused the emergence of TD Eugene.

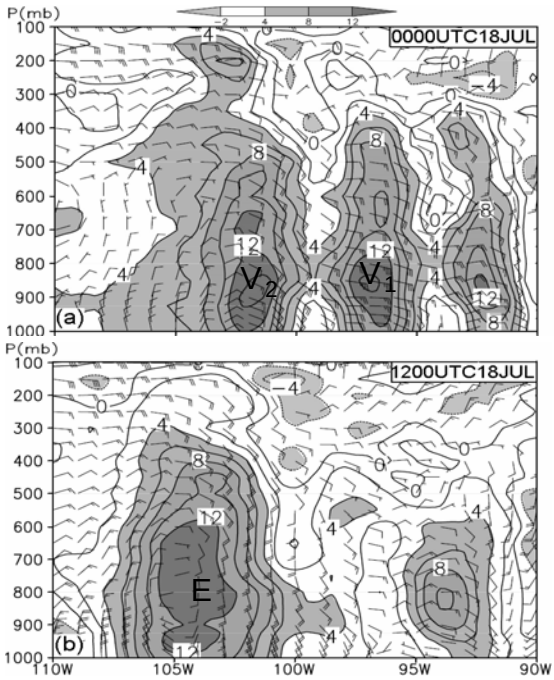

Figure 2.3. West-east vertical cross sections from NCEP's reanalysis of the vertical absolute vorticity that is area-averaged within a 3^0 latitudinal span centered along 14^0N, at intervals of 2×10^{-5} s^{-1}, superimposed by in-plane horizontal wind barbs, along the two vortex centers, valid at (a) 0000 UTC 18; and (b) 1200 UTC 18 July 2005. The absolute vorticity values of greater than 4, 8, and 12×10^{-5} s^{-1} are shaded.

Although the NCEP reanalysis may be too coarse to resolve properly the MCVs, especially V_1 at the later stages, we use Fig. 2.3 to show two distinct upright vortical columns corresponding to V_1 and V_2 at a few hours prior to the merger, and a single deeper and more robust vortex merger (E) afterward, in contrast to the other MCSs in the ITCZ which exhibit little or weak vortical signatures (cf. Figs. 2.1 - 2.3). The two MCVs have comparable magnitudes in relative vorticity and depth but V_2 displays a larger-scale rotation, which is consistent with those seen from satellite imageries (cf. Figs. 2.2 and 2.3a). However, the NCEP reanalysis does not show evidence of closed cyclonic circulations at the surface associated with V_1 and V_2 at 0000 UTC 17 July,

which is to be used as the model initial time, except for an elongated low-pressure region along the ITCZ (Fig. 2.4a). Figs. 2.4 and 2.5 show the large-scale conditions in which the genesis of Eugene occurred. The most distinct large-scale feature is the east-west oriented ITCZ over the tropical eastern Pacific and its associated converging flows between the south-easterly and the north-easterly trade winds from the southern and northern hemisphere, respectively. However, the trade winds (and the ITCZ) were no longer pronounced, at least in the boundary layer, over the landmasses of the southern Mexico and Central America. In particular, the complex topography and its associated temperature contrast across the coastline over the area between Equator and 15^0N distorted the trade wind pattern, and generated a weak pressure trough off shore (Fig. 2.4a). Because of the topographical effect, the southeasterly trade winds were shifted more to southwesterly landward to the south of the ITCZ.

Note that the lower sea-level pressure centers over the Mexican continent are fictitious because they result from the pressure reduction associated with high orography and high surface temperatures in the NCEP reanalysis. Nevertheless, the lee side of the high orography over the area appeared to be a favorable region for TCG in East Pacific, as discussed by Zehnder et al. (1999) and Molinari et al. (2000). Note also that the low pressure system moving over the Gulf of Mexico is Hurricane Emily (2005), a category-4 storm that occurred during TCSP (see Halverson et al. 2007). The other large-scale features include an intense anticyclonic circulation in East Pacific and an anticyclonic ridge extending westward along the southern coast of the U.S.

In a vertical plane, the trade wind convergence zone is characterized by

southwesterly flows turning clockwise with height and southeasterly flows turning anticlockwise to easterlies above 850 hPa to the south and north of the ITCZ,

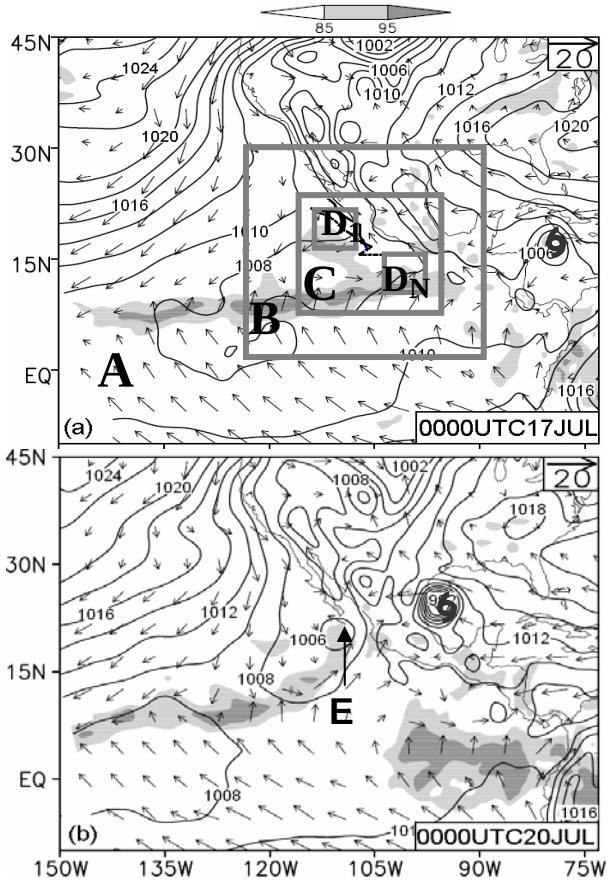

Figure 2.4. NCEP reanalysis of the sea-level pressure (solid, every 2 hPa), the horizontal flow vectors and relative humidity (shaded for 85% and 95%) at 900 hPa at (a) 0000 UTC 17; and (b) 0000 UTC 20 July 2005. The model meshes with horizontal resolutions of 36, 12, 4, and 1.33 km for domains A, B, C, and D are, respectively, sketched in (a), along with the observed (thick line) and simulated (thick-dashed) tracks. The finest domain D follows the movement of the storm, and D_1 and D_N denote the first and the last position of domain D.

respectively (Figs. 2.4 and 2.5a). Note the development of a midlevel jet of 10 – 12 m s^{-1} on each side, i.e., along 17^0N and 10^0N. The two jets are qualitatively supported by the thermal wind relation, as indicated by significant temperature gradients on both sides of the ITCZ (Fig. 2.5c). Such pronounced easterly and westerly flows imply the presence of significant cyclonic shear, i.e., an averaged shear vorticity of 3×10^{-5} s^{-1}

in the ITCZ, which was the important background vorticity for the genesis of Eugene. More importantly, they account for changes in the sign of potential vorticity (PV) gradients near the inflection point of the zonal flows (Fig. 2.5b), suggesting that the basic state in the vicinity of the ITCZ was both barotropic and baroclinic unstable (Charney and Stern 1962). NS97 show that the Charney-Stern instability is a necessary condition for the ITCZ breakdown and rollup as a result of the development of MCVs, while Molinari et al. (1997, 2000) indicate that the sign reversal of PV gradients is one of the important signals for TCG. Since diabatic heating in the ITCZ tends to generate a low-level PV maximum and a sign reversal in the meridional PV gradient (see NS97), the ITCZ is generally a favorable region for the development of mesovortices or TCG. In the present case, the zone of such a sign reversal was virtually upright, and collocated with a weak-sheared ITCZ environment in which the precursor of Eugene (i.e., V_2) was embedded (cf. Figs. 2.4a and 2.5a, b). Evidently, this ITCZ breakdown resulted from the growth of V_2, which differs from that associated with the development of V_1 more than 2 days earlier (i.e., before 11 July) and 1000 km to the southeast at 0000 UTC 13 July, and 750 km apart at the model initial time along the ITCZ (see Fig. 2.1).

Figs. 2.5a and 2.5c also show that the ITCZ was characterized by high humidity with a relatively cold pool below and warm air above as a result of continued deep convective overturning. The atmospheric conditions outward from the ITCZ are potentially unstable, with higher low-level equivalent potential temperature (θ_e) to the north where higher SST was distributed (Fig. 2.5c). These thermodynamic conditions are similar to the idealized initial conditions used by Bister and Emanuel (1997) in their axisymmetric modelling of a hurricane, in which a cold-cored midlevel

mesovortex with humid columns can be spun up into a hurricane within 3 days. They emphasized the critical roles of the initial vortex intensity and humid environment in the genesis of Hurricane Guillermo (1991). In the present case, Eugene appeared to be initiated from the merger of the two MCVs that were embedded in the moist ITCZ. Evidently, the high moisture content in the ITCZ is also the major energy source for the intensification of the storm.

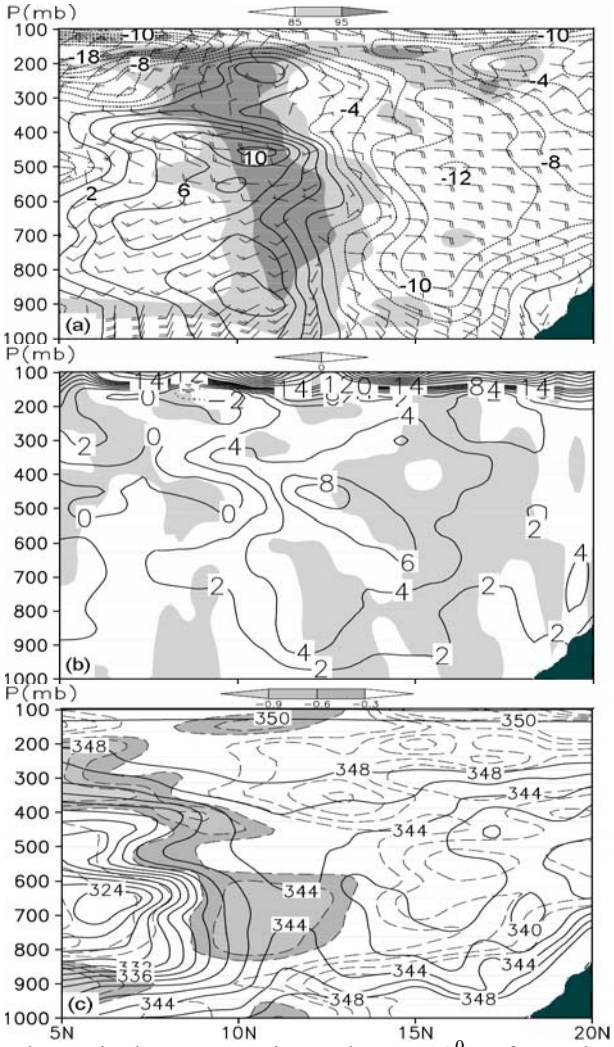

Figure 2.5. South-north vertical cross sections along 103^0W from the NCEP reanalysis at 0000 UTC 17 July 2005 of (a) the zonal wind speeds (at intervals of 2 m s^{-1}), superimposed with horizontal wind barbs (a full barb is 5 m s^{-1}) and relative humidity (shaded for > 85% and > 95%); (b) PV (at intervals of 0.2 PVU; 1 PVU = 10^{-6} m^2 s^{-1}K kg^{-1}) and meridional PV gradient (shaded for negative values); and (c) equivalent potential temperature θ_e (solid, at intervals of 2 K), superimposed by deviation temperature (dashed, at intervals of 0.3 K, shaded for negative values). Shading at the lower right corner denotes the terrain over Mexico.

Since Eugene moved northwestward after its formation, it is also of interest to examine the relation of Eugene's development to the midlevel easterly jet. NCEP's reanalysis reveals that this jet, occurring within the belt of 15^0 - 20^0N, was a persistent feature and it appeared nearly 10 days prior to Eugene's formation. The jet-related VWS appears to limit the growth of Eugene after reaching its peak intensity at 1200 UTC 19 July with the minimum sea-level pressure of 989 hPa and the maximum surface wind of 31 m s^{-1} (Figs. 2.2 and 2.7). In addition, colder SST, its separation from the ITCZ, dry intrusion and some other factors to be discussed in Chapter 9, all played important roles in weakening the storm. By late in the day of July 20, Eugene became a remnant low about 100 km southwest of Cabo San Lucas (see Fig. 2.2). It continued its northwestward movement until its dissipation 2 days later.

5.3. Experimental design

In this study, the processes leading to the genesis of TS Eugene (2005) are explicitly simulated using a two-way interactive, movable, multi-nested (36/12/4/1.33 km) grid version of the WRF model (V2.1.2; see Skamarock et al. 2005) with the finest grid size of 1.33 km. The model microphysics schemes used include (a) a modified version of the Kain-Fritsch (1990) cumulus parameterization scheme for the 36- and 12-km resolution domains in which deep convection and a broad range of shallow convection are both parameterized; (b) the Yonsei University planetary boundary layer (PBL) parameterization with the Monin-Obukhov surface layer scheme; (c) the Rapid Radiative Transfer Model (RRTM) scheme for both longwave and shortwave radiations with six molecular species (Mlawer et al. 1997); and (d) the Lin et al. (1983) cloud microphysics scheme containing six classes of hydrometeors, namely, water vapor, cloud water, rain, snow, graupel, and cloud ice. Note that no

cumulus parameterization is used in the 4- and 1.33-km resolution domains.

The four nested-grid domains have the (x, y) dimensions of 251 × 201 (A), 252 × 252 (B), 388 × 382 (C), and 451 × 451 (D) with the grid size of 36, 12, 4, and 1.33 km, respectively (see Fig. 2.4a for the nested domains A - D). There are 38 σ levels in the vertical; they are 1.000, 0.993, 0.980, 0.966, 0.950, 0.933, 0.913, 0.892, 0.869, 0.844, 0.816, 0.786, 0.753, 0.718, 0.680, 0.643, 0.607, 0.572, 0.538, 0.505, 0.473, 0.441, 0.409, 0.378, 0.348, 0.318, 0.289, 0.260, 0.232, 0.204, 0.176, 0.149, 0.122, 0.095, 0.068, 0.042, 0.018, and 0.000. The model top is defined at 30 hPa. To minimize the computational costs, domain D is activated at 24 h into the integration and it is moved within domain C every 15 minutes following the storm. In this control simulation, domain D's movement is performed manually because the storm's pressure center is too weak to be determined by the model prior to the merger of the two MCVs. Because of the limited computer power, domain D is configured to cover only the area where V_1 and V_2 are about 500 km apart rather than where they are initially present.

The WRF model is initialized at 0000 UTC 17 July 2005, which is about 36 hours prior to the depression stage of Eugene, and then integrated for 4 days until the storm is nearly dissipated. No bogus data is used. Despite its 1^0 resolution, the NCEP reanalysis appears to resolve marginally the two MCVs under study with diameters of about 400 km at the model initial time, as compared to those seen in satellite imaginaries. Nonetheless, a successful simulation of the case will allow us to examine the genesis of a TC from weak midlevel MCVs to a TS, and its subsequent dissipation in the East Pacific environment that could not be studied with the NCEP reanalysis data.

The model initial and lateral boundary conditions are taken from the NCEP reanalysis with the outermost lateral boundaries updated every 6 hours. NCEP's SST field is used and kept constant in time (Fig. 2.6); its magnitude decreases from 29^0 to 23^0C northwestward along Eugene's track. This choice of keeping SST constant is justified by little temporal variations of the SST during the model integration period, based on the analysis of the Tropical Rainfall Measuring Mission (TRMM) Microwave Imager (TMI) level-1 product (not shown). In addition, there is little evidence of the storm-induced cooling along its track, due to the generation of relatively weaker surface winds by the storm.

5.4. Model verifications

In this section, we validate the model-simulated results against the best track analysis and satellite observations since little field observations were available for this storm (Halverson et al. 2007). We will focus more on the storm-scale cloud/precipitation in relation to the evolution of the MCVs, their merger and the ITCZ. Due to the small domain size of the 1.33-km grid, some results will be presented from the 4-km grid in order to show better the storm-environment interactions.

Fig. 2.6a compares the simulated track of Eugene, based on the minimum sea-level pressure, to the best track analysis. It is evident that the WRF model reproduces reasonably well the track of Eugene, especially the timing and location of its genesis at 39 h into the integration. However, the simulated track tends to possess a southwestward bias at later stages, leading to about 380-km southwestward departure from the observed at the end of the 96-h simulation. This southwestward bias appears to be related to the southwestward (downshear) tilt of the storm's circulation center

with height (Fig. 2.6a), because a stronger storm than the observed is simulated (Fig. 2.7). This may be understood through the upper- and lower-level vortex-vortex interaction in the presence of VWS (see Wu and Emanuel 1995; Jones 1995). That is, the convectively generated upper-level PV anomaly tilted to the southwest of the storm under the influence of easterly VWS may induce a low-pressure circulation beneath, thereby "pulling" the surface low center southwestward from its normal track.

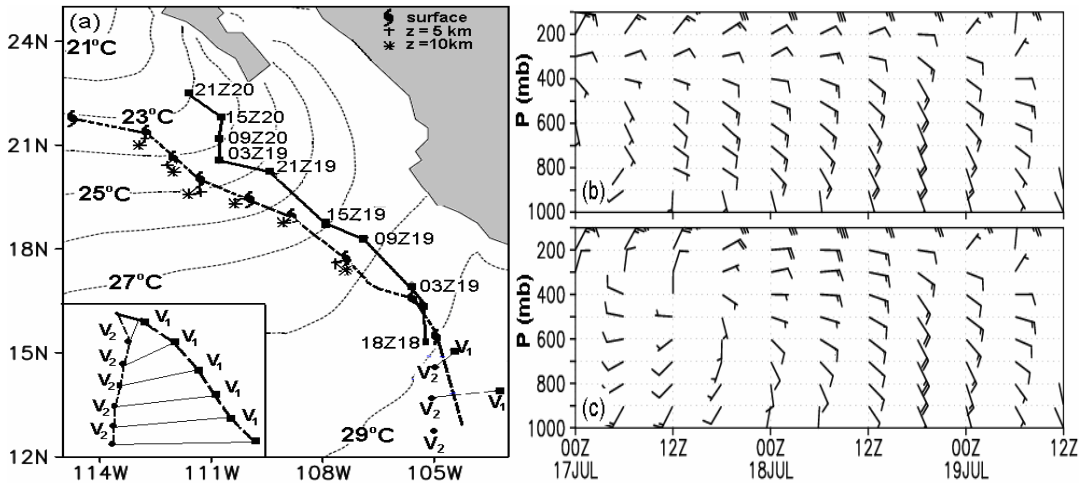

Figure 2.6. (a) Comparison of the simulated track (dashed) of Eugene to the best track analysis (solid), superimposed by the SST field (dotted) at intervals of 1^0C. The simulated minimum pressure positions of Eugene at the three selected model levels (z = 0, 5, 10 km) are also shown. Note that the model-data points are given at the corresponding best track analysis times. Lower left corner enlarges the tracks of both "V_1" and "V_2", based on their 850-hPa relative vorticity and surface pressure centers, from 18/00-24 to 18/18-39 at 3-h intervals. Time-height cross section of the (400 km x 400 km) area-averaged horizontal wind barbs centered at (b) V_1 and (c) V_2 from 17/00-00 to 19/12-60. Note that the wind barbs in (b) and (c) become more similar after 18/06-30 and identical after 18/18-39 due to their merging.

To validate the conjecture, a sensitivity experiment, in which both shortwave and longwave radiation schemes are switched off from the control run, is conducted in an attempt to obtain a weaker storm (not shown), based on the previous TC modeling studies (e.g., Liu et al. 1997). As expected, the model produces a weaker, shallower

TC but with its track closer to the observed because of the less influence of the upper-level flows. This indicates that the TC intensity, if not accurately predicted, could cause large errors in its predicted track in the presence of the larger-scale VWS. Note that the influence of VWS on the TC track presented herein differs from that in the previous studies in which the leftward or rightward biases of TCs movements in the presence of strong VWS are addressed (Wu and Emanuel 1993; Wang and Holland 1996). In those studies, TCs move along VWS vectors, whereas the VWS vector here is almost orthogonal to Eugene's track (cf. Figs. 2.6a and 2.12).

Fig. 2.6a also shows the relative positions of the simulated V_1 and V_2 during an 18-h period prior to their merger. One can see from Figs. 2.2 and 2.6a that V_2 moves north-northeastward on the eastern end of the ITCZ as the latter rolls up as a result of dynamical instability, whereas V_1 moves at a faster pace northwestward under the influence of the low- to mid-level southeasterly flow offshore along the Mexican coast (cf. Figs. 2.1, 2.2, and 2.6b,c). Thus, they appear to occur as the coalescence of two vortex entities, as described by Lander and Holland (1993), due to their different propagation speeds and directions associated with different larger-scale steering flows (cf. Figs. 2.6b,c), and then as the capture of a smaller vortex by a larger one (i.e., V_1 by V_2). Note that V_2 does not change its northward course (but its speed) until the two centers are less than 120 km apart at 1500 UTC 18 July or 39 h into the integration (hereafter referred to as 18/15-39), implying that V_1's RMW has intersected with V_2's. These scenarios appear to differ from the TCG cases observed by RH97 and Simpson et al. (1997) in which midlevel MCVs were merged within a low-level larger-scale cyclonic circulation. This implies that the merger would sooner or later take place within the larger-scale cyclonic system. However, in the present

case, only when V_1 and V_2 arrive in near proximity (e.g., less than 450 km between their centers), the vortex-vortex interaction tends to slow the north-northwestward movement of V_2, but accelerate slightly the northwestward displacement of V_1, both in spiral orbits, until the two MCVs completely merge. Clearly, they would not be merged if there are some changes in their tracks. To our knowledge, the coalescence and capture of MCVs leading to the formation of TD have not been reported in the literature. After the merger, both the observed and simulated storms move northwestward, following closely the tracks and speeds of V_1 but still behaving like the rollup of the ITCZ as V_2 for a while (see Figs. 2.2, 2.4b and 6a).

The simulated minimum sea-level pressure and maximum surface wind are compared to the observed in Fig. 2.7, which shows that the model captures the major characteristics of Eugene including its genesis, significant deepening and intensity changes as well as its final weakening. As expected, the simulated maximum intensity is stronger than the observed, i.e., about 2 hPa deeper and 8 m s^{-1} higher, because of the use of higher-resolution grid-point values; but it occurs 6 h earlier than the observed. Furthermore, the simulated storm weakens at a rate slower than the observed, due partly to its farther westward tracking out to the open ocean than the observed; this would cause the access of relatively less continental dry air masses (but more oceanic moist air) to suppress the storm development.

Of interest is that the (area-averaged) environmental VWS prior to the merger is 8 – 10 m s^{-1} for both V_1 and V_2 due to the opposite wind directions (i.e., east-northeasterly vs. west-southwesterly) between 200 and 900 hPa, but it drops to 2 - 3 m s^{-1} near 18/12-36 with the maximum surface winds exceeding 20 m s^{-1} (see Figs. 2.6b, 2.6c and 2.7). The local VWS within the ITCZ in which V_2 is embedded is

much smaller than the area-averaged, as can be seen by nearly upright isotachs in Fig. 2.5a. This abrupt drop in VWS during the merging period is not an artifact of the area average but a result of the merger. That is, both V_1 and V_2 are relatively shallow systems with more visible cyclonic flows up to 400 hPa and some directional shear above (see Figs. 2.3a and 2.6b,c). As soon as the two MCVs are merged, the storm is strengthened with a deep vortical column with little directional shear, i.e., nearly all southeasterly in the vertical, thereby decreasing VWS significantly (see Figs. 2.3b and 2.6b,c). The decreased VWS in Eugene's immediate environment in turn allows the storm to keep deepening for 30 – 36 h, albeit at a relatively slow rate of 0.3 hPa hr^{-1}. Subsequently, the storm begins to weaken, which coincides well with a steady increase in VWS up to 18 m s^{-1} as it moves northwestward away from the moisture supply of the ITCZ.

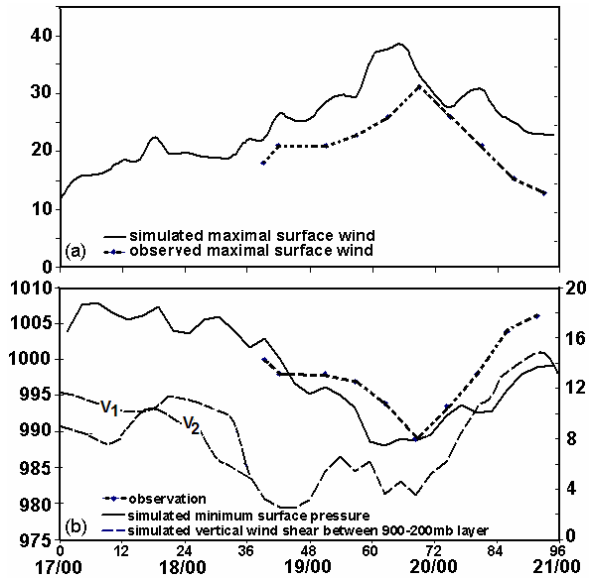

Figure 2.7. Time series of (a) the simulated maximum surface wind (solid, m s^{-1}) versus the observed (dotted); and (b) the simulated minimum sea-level pressure (solid, hPa) versus the observed (dotted) during the 4-day period of 17/00-00 to 21/00-96. Note that the best track analysis is only available during the final 54 hours. The time evolution of the area-averaged (800 km × 800 km) VWS (long-dashed, m s^{-1}) in the layer of 200 – 900 hPa is also shown in (b). VWS during the first 36-h simulation is taken around V_1's and V_2's center within an area of 400 km × 400 km because of their reducing distance with time.

Fig. 2.8 compares the model-simulated 6-h accumulated rainfall at 12-h intervals during the genesis and deepening stages of Eugene (i.e., 1200 UTC 17 – 0600 UTC 20 July) to the corresponding TRMM satellite product at 0.25^0 resolution. It is evident that although the WRF model could not reproduce all the rainfall details, it simulates reasonably well the general magnitude and structures of the observed rainfall. They include the ITCZ-related rainfall belt to the south (Figs. 2.8a – 2.8c), its subsequent northward rollup to form a "comma-shaped" rainfall pattern as a closed surface cyclone develops (Figs. 2.8c - e), the more organized and intense rainfall over the "comma-head" region with less rainfall distributed along the "comma-tail" (Figs. 2.8d – f), and the suppressed deep convection over the coastal regions at the later stages (Figs. 2.8c – f). Note that the northward rollup on the eastern end of the ITCZ is similar to that described by NS97 and WM06. The simulated 6-h maximum rainfall rate exceeds 90 mm, which is comparable to the observed. Of importance is that both the simulation and TRMM observations show (a) several localized rainfall centers around the surface cyclone, with much greater magnitudes than those in the ITCZ, and (b) significant rainfall asymmetries with little rainfall occurring to the north of the surface cyclone. As will be shown in the upcoming chapter, the more localized rainfall centers tend to occur on the downshear left (Frank and Ritchie 2001; Black et al. 2002; Zhang and Kieu 2006). Moreover, if the localized rainfall centers associated with the surface cyclone are traced in time (e.g., Figs. 2.8a – c), one can see that major convective cells are initiated to the south and then moved cyclonically to the west and east of the surface cyclone, though with reduced magnitudes. More intense rainfall occurs when two convective complexes merge (Figs. 2.8a – c), which is consistent with the merger of the two MCVs mentioned earlier.

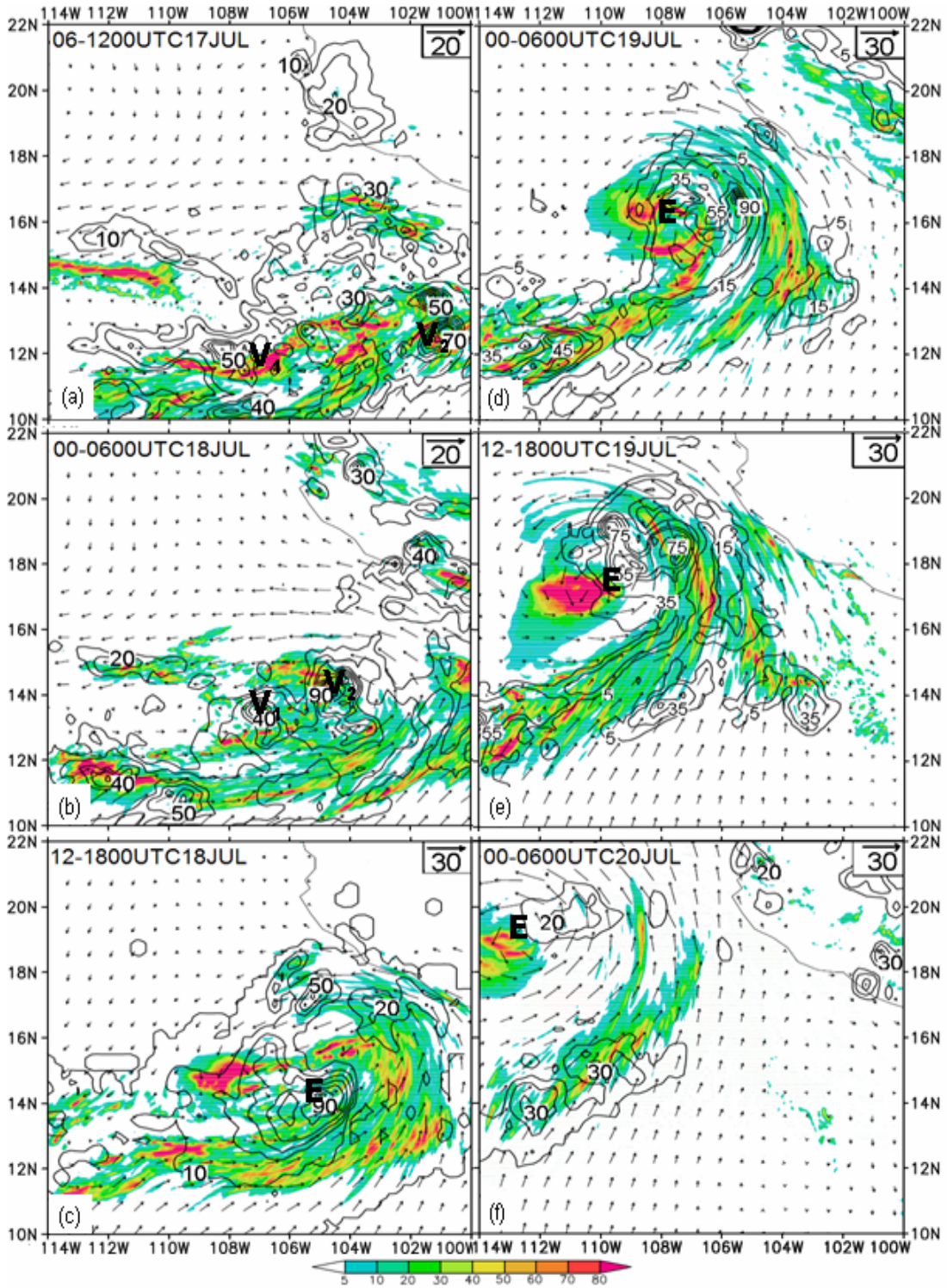

Figure 2.8. Comparison of the 6-h accumulated rainfall (mm) valid at the (a) 17/06-06; (b) 18/00-24; (c) 18/12-36; (d) 19/00-48; (e) 19/12-60; and (f) 20/00-72 simulations over a subdomain of C to the corresponding 6-h TRMM satellite-estimated (contoured). The simulated surface flow vectors are also provided.

While the WRF model reproduces many rainfall features of Eugene, there are significant errors in the position of local rainfall centers (and timing) associated with the "comma-head" due to the westward bias of the simulated track (Fig. 2.7). These errors are more pronounced during the weakening stage, so the simulated and observed rainfall fields are not compared after the 72-h integration. Despite these errors, the general agreements of tracks, intensity and rainfall patterns between the simulation and observations indicate that the model reproduces the basic sequence of any processes involved in the genesis and development of Eugene. Thus, the model-simulated high-resolution hourly output data could be used to examine some non-observable features, and the effects of VWS on the rainfall distribution during the life cycle of Eugene.

Chapter 6. Vortex-merger cyclogenesis

In this chapter, detailed kinematical and dynamical processes associated with vortex merger that lead to the formation TS Eugene will be presented. In section 6.1, we show first the vortex merging kinematics in the context of PV in order to facilitate the subsequent discussion of the roles of merging MCVs and CGVs in TCG. Section 6.2 describes the theoretical framework, and section 6.3 examines the effects of PV sources in the ITCZ during the development of Eugene through the analyses of PV budgets. Section 6.4 explores the dynamics of vortex merger, and some possible mechanisms by which the bottom-up or top-down growth of cyclonic vorticity is operative during the merging phase through the vertical absolute vorticity budgets are given in section 6.5. In the last section, we shall present some sensitivity experiments to illustrate further the roles of vortex merger in triggering the early intensification.

6.1. Vortex merging kinematics

Since the 3D coalescence and capture phenomenon as seen in Figs. 2.2- 2.3 is not well understood, let us examine how the two MCVs interact and merge in three dimensions to cause the genesis of Eugene, in order to compare its pertinent scenarios to the merging MCVs cases documented in the previous studies. Fig. 2.9 shows that the simulated MCVs begin to spin up at 17/18-18 over the 4-km grid. Moreover, they show reduced widths, especially V_1 after the 1.33-km grid domain is activated at 18/00-24. The two MCVs commence to merge at 18/09-33, about 3 -6 hours later than the observed (cf. Figs. 2.9 and 2.2); the merging processes are, as expected, much better resolved temporally and spatially than the NCEP reanalysis (cf. Figs. 2.9 and 2.1). The (north-northeastward) drift of V_2 associated with the rollup of the ITCZ

compared to the (northwestward) propagation of V_1, and their relative sizes prior to the merger are also evident in Fig. 2.9, which are to a certain degree consistent with the satellite imageries and the associated rainfall field (Figs. 2.2 and 2.8). Note the increased width at the time of merging (i.e., 18/12-36), but its reduced width immediately afterward is due mainly to the longitudinal averaging of the merging MCVs as V_1 moves cyclonically from the east to north side of V_2 (see Fig. 2.6) by 18/18-42. As will be seen in the next, the complete merging does not occur until 19/00-48, taking a total of 15 hours (i.e., from 18/09-33 to 19/00-48). Note also that V_2 is not as well structured as V_1 because of their different locations of the peak relative vorticity in the vertical, i.e., 800 hPa for V_1 and 700 hPa for V_2 (not shown).

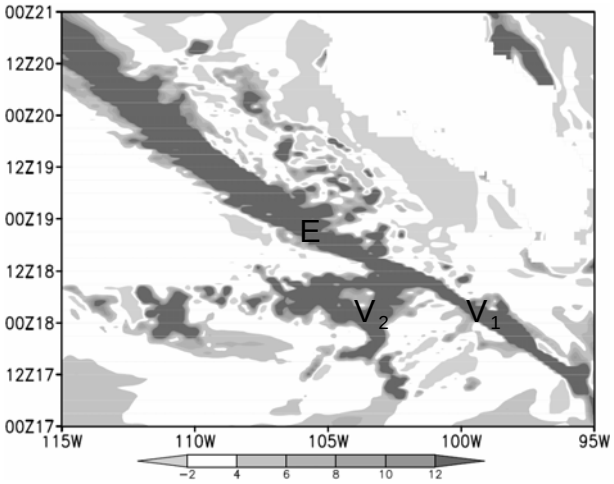

Figure 2.9. As in Fig. 1 but for the model-simulated during the period of 0000 UTC 17 - 0000 UTC 21 July 2005 (i.e., 17/00-00 to 21/00-96) and the longitudinal span of $115^0 – 95^0$W. It is meridionally averaged within a 1^0 zone centered through the MCV V_1 and later Eugene.

Fig. 2.10 shows the simulated flow and reflectivity fields at the surface and 200 hPa, and PV at 500 hPa before, during, and after the merging stage, while Fig. 2.11 shows the corresponding vertical cross sections of the tangential flows and PV through the MCVs/storm centers. The WRF simulates an intense but small-sized V_1 with the minimum surface pressure of 1004 hPa and an RMW of about 100 km, and a

relatively weak and broad scaled V_2 with a closed isobar of 1007 hPa and an RMW of 200 km prior to the merger (Fig. 2.11a). Note that the size of V_1 has been shrunk by half, as it intensifies, from that at the model initial time (cf. Figs. 2.1 – 2.3 and 2.10). These features conform more or less to those seen from satellite imageries (see Fig. 2.2). Organized deep convection associated with the two MCVs produces significant concentration of PV in banded structures in the layer of 600 - 400 hPa, where the latent heating and upward motion are peaked. Of interest is that in spite of the pronounced PV, one could only see the two closed cyclonic circulations of the MCVs above 700 hPa but little closed rotation below (Fig. 2.11a, b). This is because the penetration depth (Δz) is still shallow for dynamically small vortices ($L << L_R$, where L_R is the radius of Rossby deformation) and small magnitudes of PV or the absolute vorticity (ζ_a) anomalies, i.e.,

$$\Delta z = (f \zeta_a)^{1/2} L/N, \qquad (2.1)$$

where f is the Coriolis parameter, and N is the static stability (see Hoskins et al. 1985).

At the lower levels, the two MCVs appear to compete each other for convective available potential energy (CAPE) for convective developments on their southern semicircles, when they are near proximity (e.g., 450 km). More higher-θ_e air in the ITCZ is converged into the convective regions of V_1 (Fig. 2.10), generating the most intense convection in its southeastern quadrant, as can be seen at 200 hPa. The intense convective cells coincide with the strong signals seen in satellite imageries at 0300 and 0600 UTC 18 July (cf. Figs. 2.2 and 2.10). In this regard, V_1 intensifies at the expense of V_2, and the latter has soon become a wake MCV of the former. Note that deep convection always occurs some distance away from the surface cyclone center,

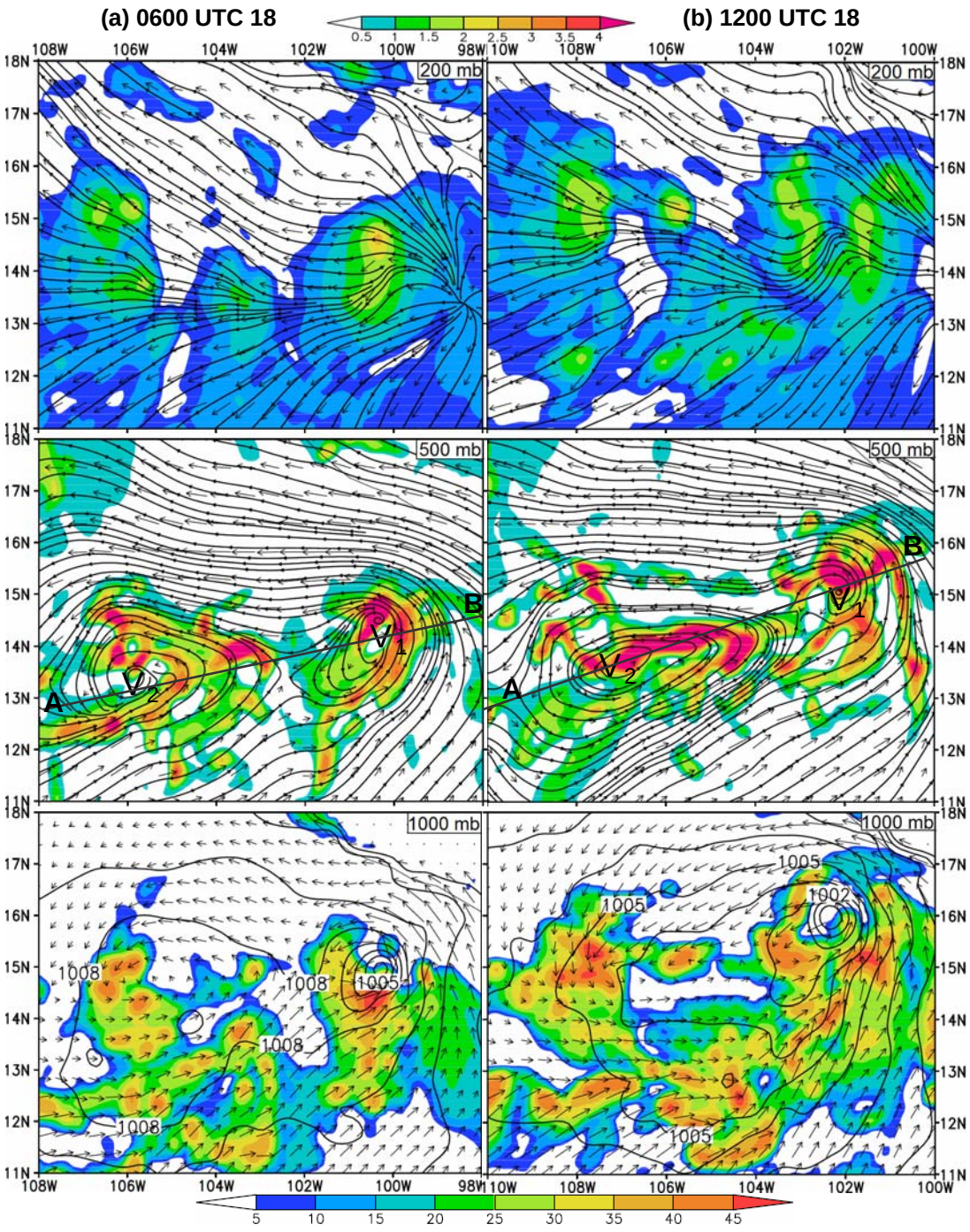

Figure 2.10. Horizontal distribution of the sea-level pressure (at intervals of 1 hPa) and flow vectors (bottom); flow vectors and streamlines at 500 hPa (middle); and flow vectors and streamlines at 200 hPa (top) over a subdomain of C at (a) 18/06-30; (b) 18/12-36; (c) 18/18-42; and (d) 19/06-54. Shadings in the top and bottom panels are for the simulated radar reflectivity, at intervals of 5 dBz, and in the middle panels are for PV, at intervals of 0.5 PVU. Line "AB" shows vertical cross sections used in Fig. 2.11. All flows are system relative.

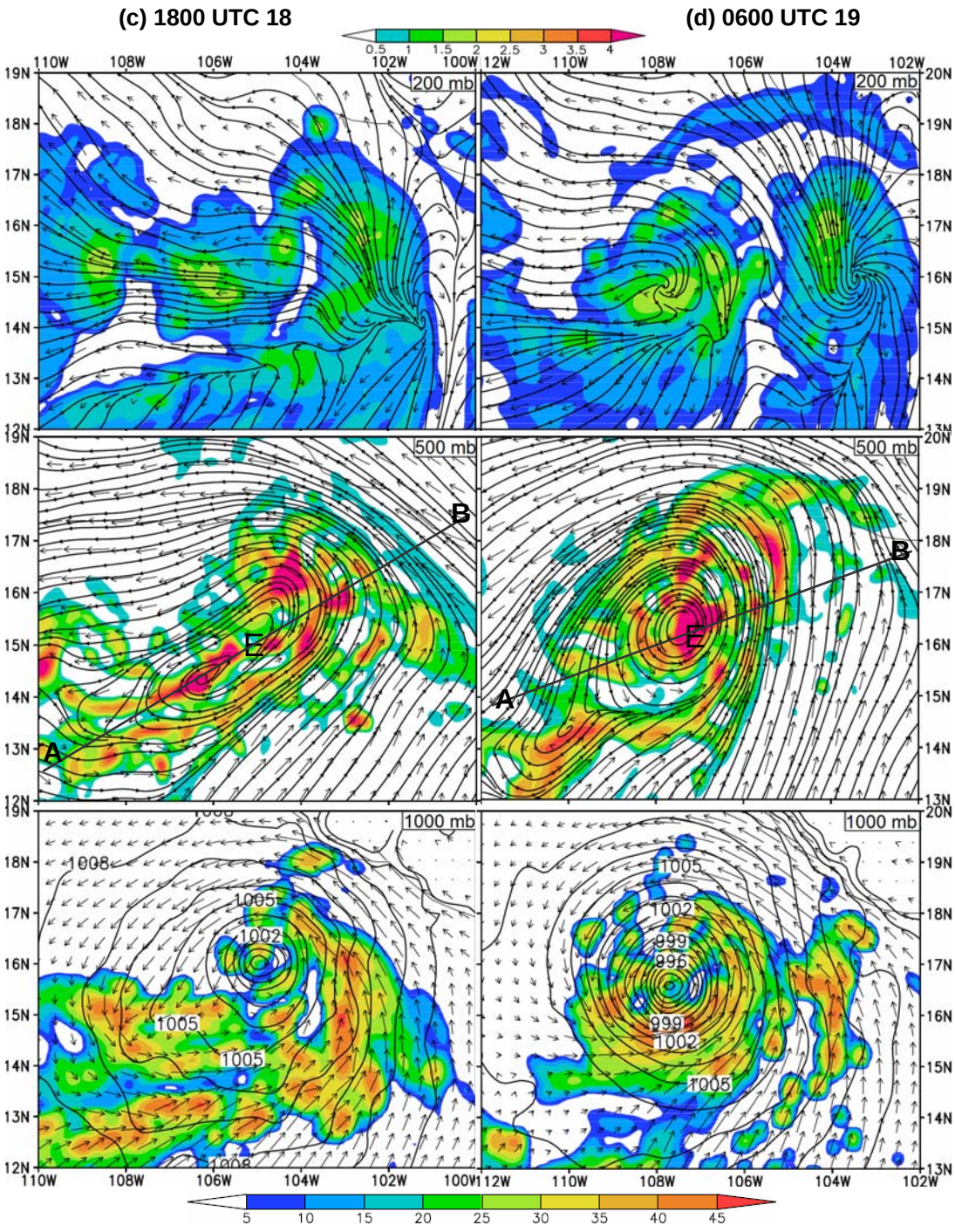

Figure 2.10. Continued.

suggesting that convectively generated compensating subsidence warming accounts for the formation of a rain-free, "eye-like" region at the storm center. Higher up, both MCVs generate strong divergent winds aloft that are superimposed on the upper-level easterly flows.

At 18/12-36, V_2 has almost lost its identity in reflectivity and surface circulations in the wake of a to-be-formed TD, as the low- to mid-level PV increases in magnitude and volume and the distance between the two MCVs shortens by half (Fig. 2.10). Clearly, the increased surface winds (up to 22 m s^{-1}, see Fig. 2.7) help initiate the WISHE process leading to the subsequent TCG (Rotunno and Emanuel 1987). Of importance is that despite its weakness the general midlevel flow pattern is still dominated by the V_2-related circulation due to the larger volume it occupies. As a result, the V_2-related southerly flow tends to offset the northerly flows associated with V_1 in the vertical before their complete merger (see Fig. 2.11).

By 18/18-42, a well-organized surface cyclone has developed, and the two MCVs would be considered having merged if only the surface circulations are concerned. However, we can still see an elongated circulation with identifiable V_2's remnant flow and PV at the midlevel. Evidently, despite its stronger intensity, it is V_1 that is "impinged" upon V_2's circulation and later absorbed by V_2 because of the slower pace and larger volume of V_2. Nevertheless, the volume of the merged circulation has shrunk substantially during the previous 12-h period, with the distribution of concentrated PV stripes within it, leading to the pronounced deepening of the storm at the broad scale (Fig. 2.10).

Although the two MCVs are completely merged at 19/00-48, the merged circulations are better defined 6 h later, so the results at 19/06-54 are shown herein.

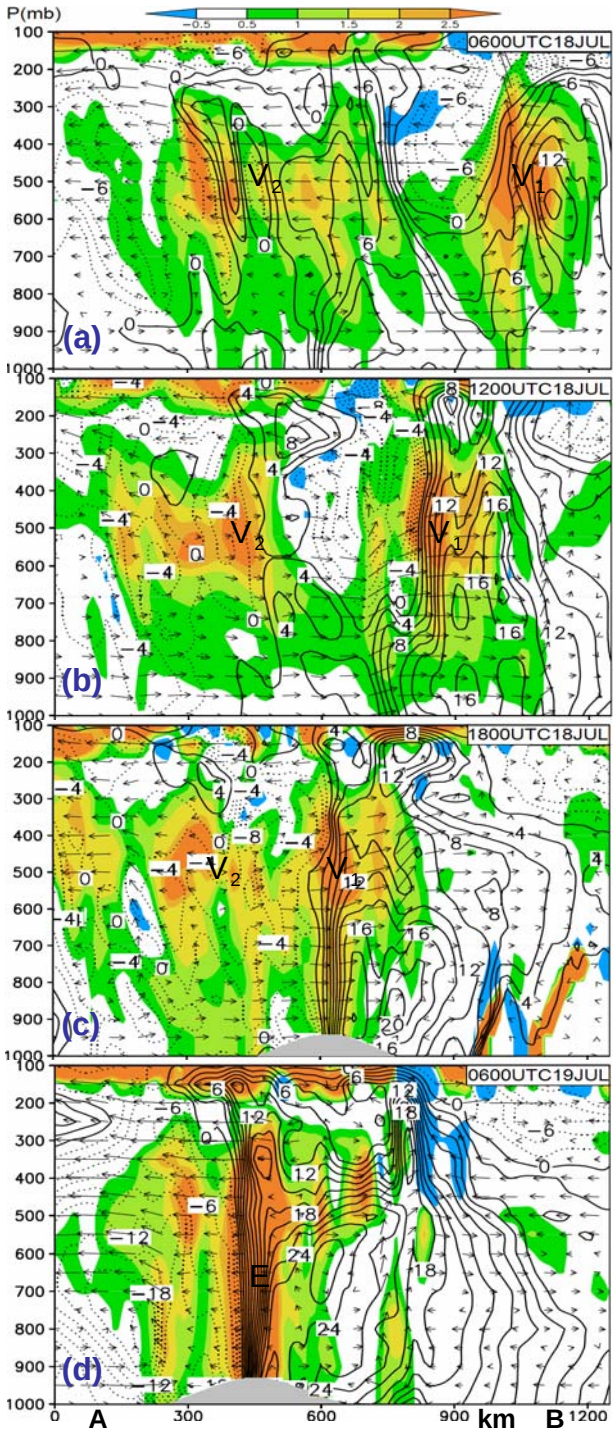

Figure 2.11. As in Fig. 2.10 but for the the 3-slice-averaged (i.e., 4-km) vertical cross sections of the normal component of horizontal winds (at 2 m s^{-1} intervals), PV (shaded at intervals of 0.5 PVU), superimposed by the system-relative in-plane flow vectors along the centers of V_1 and V_2 (see Fig. 10 for their locations). Note that the vertical wind component has been amplified by a factor of 10.

At this latter time, the merger is characterized by the development of deep convection in all quadrants, though still as a "comma head" of the ITCZ rollup, and a deep column of PV near the vortex center with well-defined tangential flows around it and anticyclonic outflows aloft. It has an RMW of about 200 km, which is similar to that of V_2 (Fig. 2.11). Note that a spiral rainband in the southeastern quadrant produces intense anticyclonic outflows aloft that appear to block the influence of upper-level easterly flows, thus protecting the vortex core temporally from VWS or dry-air intrusion (Figs. 2.10 and 2.11). This seems to be consistent with the development of deep convection in all quadrants when the MCVs are merged at 19/06-54, in contrast to the wavenumber-1 structures seen at the other hours. Note also that the storm has begun to experience the influence of approaching outflows associated with Hurricane Emily (2005), as indicated by limited eastward expansion of its anticyclonic flows aloft along the east boundary (Fig. 2.10). It should be noted that the tangential flows are peaked at the midlevel prior to the merger (Fig. 2. 11a). During the merging period, the tangential flows increase much more rapidly in the lower troposphere than at the midlevel (cf. Figs. 2.11a-2.11d), in pace with the deepening of the storm; similarly for the PV (or relative vorticity) in the "eye". This scenario differs from the simple "downward growth of the midlevel relative vorticity" proposed by RH97 when merging MCVs occur within a low-level larger-scale cyclonic system.

To look more detail into this downward growth issue, Fig. 2.12 shows the east-west vertical cross sections of the longitudionally averaged PV and its local tendencies during the period of 18/09-33 and 18/23-47 encompassing the vortex merger and part of the subsequent intensification. It is obvious that the two MCVs consist of many meso-γ scale PV patches or CGVs tilting cyclonically downshear

with their PV centers located in the midtroposphere. These features have not been previously shown due to the use of coarse-resolution observations and simulations. These vortices appear to be the collected smaller-scale VHTs after the longitudional averaging. Because major convective developments in the ITCZ occur on the southern half of the MCVs circulations prior to merger, most γ-scale vortices in V_2 are seen moving cyclonically eastward (cf. Figs. 2.12 and 2.13), as indicated by the PV tendencies occurring ahead of CGVs. The MCV-merging processes are marked by the gradual capture of each of the γ-scale vortices within the quasi-stationary V_2 by the northwestward propagating V_1, and by the organized upward motion at increasingly larger scales with the peak magnitudes in the upper troposphere (see Figs. 2.9 and 2.13). Some patches of large positive PV tendencies are associated with the diabatic generation of PV, as will be seen in the next chapter. Note that although the longitudional-averaged vertical motion is upward near the merger's center, horizontal maps show little radar reflectivity, just like an "eye," over the central portion of the TC circulation.

In general, the longitudional-averaged PV traces reasonably well the evolution and interaction of CGVs and their merging into the PV volume of V_1 leading to the genesis of Eugene, except for a few PV patches in V_2 (e.g., the leftmost one at 18/11-35) which appear to change sharply in magnitude with time due to the diabatic destruction of PV to be shown in the next chapter. Note that due to the smaller size, V_1's circulations at individual levels are seen being absorbed by V_2's as V_1 coalescences and enters the northern half portion of V_2's circulation (see Figs. 2.6 and 2.13), so V_1 may be viewed horizontally as a "comma head" that rolls up PV-containing vortices in V_2 (and later in the ITCZ) in the tail (Fig. 2.13).

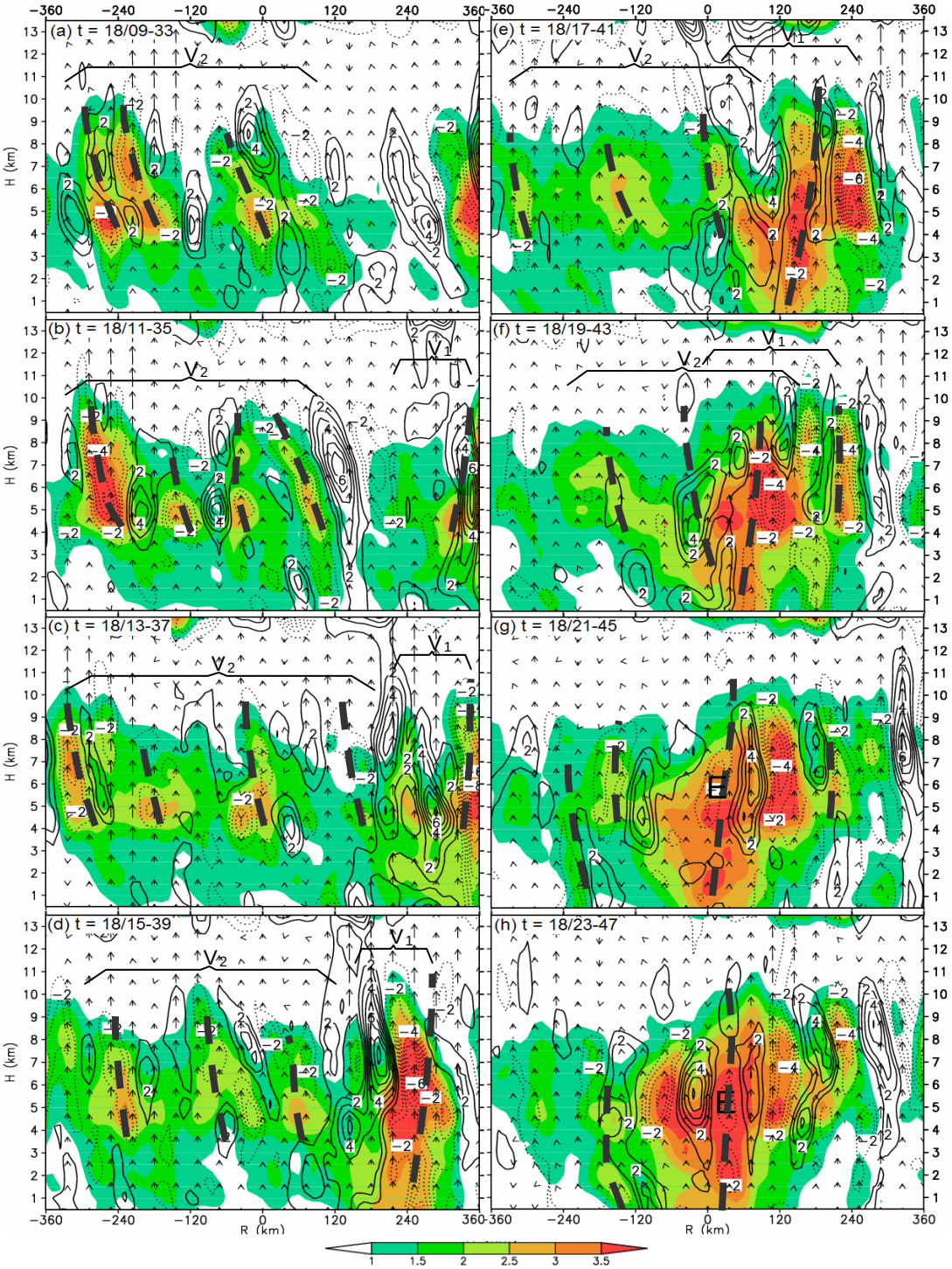

Figure 2.12. Vertical cross sections of the north-south average of PV (shaded, every 0.5 PVU) within ± 360 km along the line through the centers of V_1 and V_2, and the corresponding PV tendency (contoured, every 10^{-4} PVU s^{-1}), superimposed with the vertical motion vectors, from 18/09-33 to 18/23-47. Bold-dashed lines are for convectively generated vortices spawn within V_2 and V_1.

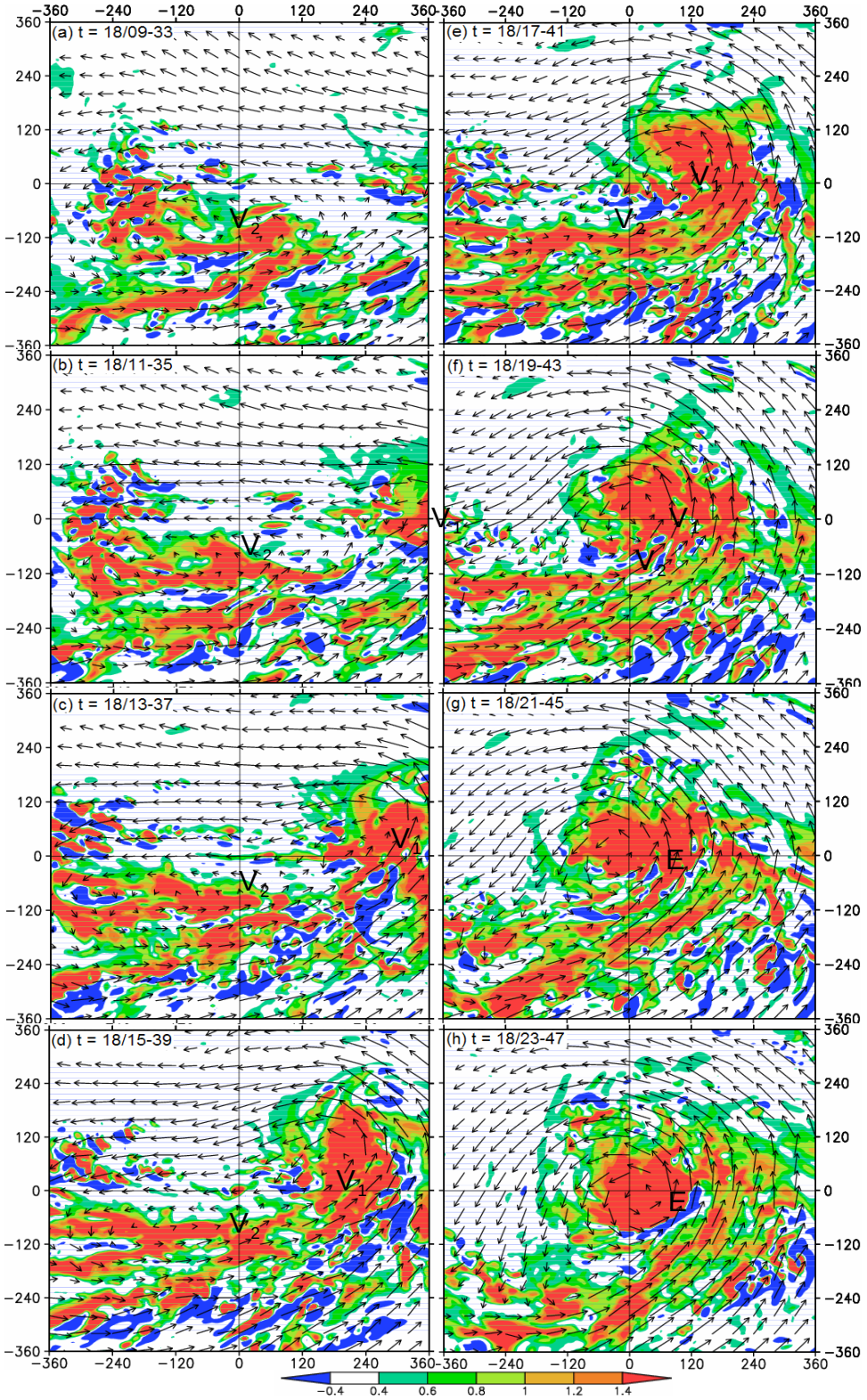

Figure 2.13. As for Fig. 2.12 but for horizontal distribution of the vertically averaged PV (shaded, every 0.2 PVU), superimposed with flow vectors at z = 3 km.

Of importance to this study is a significant increase in intensity and three-dimensional (3D) volume of high PV as V_1 captures each γ-scale vortex after 18/15-39. This increase is especially pronounced in the midtroposphere where the peak PV associated with most of the γ-scale vortices is located. The lower-level PV also increases in magnitude and area coverage, which results mostly from the merging of the lower-level PV sources, as indicated by positive PV tendencies in the lower troposphere. This indicates that the vertical PV distribution of these γ-scale vortices may determine to some extent the corresponding vertical PV structures of TCs after being merged. This could be understood simply using the mass-weighted PV (i.e., PV substance) conservation for a domain bounded by two closed isentropic surfaces, according to Hayes and McIntyre (1987; hereafter HM87), i.e.,

$$\frac{d}{dt}\left(\int_{V(t)} \rho q dV \right) = 0, \tag{2.2}$$

where $q = \rho^{-1}\vec{\omega} \bullet \nabla\theta$, ρ is air density, $\vec{\omega}$ is the 3D absolute vorticity vector, ∇ is the 3D gradient operator, θ is the potential temperature, and V (t) is a 3D control volume moving with the storm. Assuming that isentropic surfaces above the planetary boundary layer (PBL) are near-horizontally distributed prior to the hurricane stage, the lower-level PV substance in the merger within a layer enclosed by the two neighboring isentropic surfaces could only come from that of the γ-scale vortices within the same layer through the horizontal advection even in the presence of friction and diabatic heating. Note that while the volume-integrated PV substance is conserved, the local PV could change significantly, depending on the time variation of air density. In fact, the point value of PV increases from a few PVUs prior to merger to 35 PVUs after reaching TS intensity (not shown).

In addition to their effects on the vertical distribution of PV, those γ-scale vortices propagating cyclonically in the merger become more upright as they reach TS intensity (e.g., at 18/23-47). As will be shown in the next chapter, some other dynamical processes will also contribute to the lower-level increased PV. By 18/23-47, a robust vortex-merger emerges with higher-PV values but a smaller V_1-V_2-collected circulation size; namely, the west-east width of the merger has shrunk by half during the past 10 h (i.e., 18/13-37 to 18/23-47). Clearly, the shrunk circulation size, and the increased PV amplitude and high-PV volume associated with the vortex merging, caused mainly by latent heat release, are all favorable for the deepening of the surface cyclone (Figs. 2.7 and 2.9). Note that the merger's circulation size is greater than either V_1's or V_2's (see Fig. 2.13). It is evident that these merging processes could not be adequately described by nondivergent barotropic models (e.g., Montgomery and Kallenbach 1996).

Fig. 2.13 shows that these γ-scale PV patches associated with V_2 are aligned along the mean sheared flows into linear PV bands. Of significance is that these convectively generated PV bands are the "feeder" of PV into V_1 as the "comma head" rolls up northwestward. Specifically, prior to merger (e.g., at 18/09-33), the dominant larger-scale flows are easterly and westerly on the respective northern and southern side of the ITCZ, with considerable shear vorticity. As more PV bands are fed into V_1's circulation and locally concentrated in the "comma head", more shear vorticity is converted to curvature vorticity (see Bell and Keyser 1993; Zhang and Bao 1996b), leading to the generation of an intensifying TC circulation with the weakest flow at its center. The associated TC circulation also increases in size and intensity with time as more PV substance is "absorbed". The complete merging of the two MCVs near the

end of the merger, i.e., after 18/21-45, gives rise to the formation of Eugene. Note the continued PV fluxes associated with deep convection in the westerly flows from the ITCZ into Eugene's circulation that play an important role in increasing the high-PV volume near the circulation center and facilitating the continued deepening of the storm long after the vortex merger scenario.

6.2. Dynamical framework

We have seen from Figs. 2.12 and 2.13 the considerable concentration of PV near the vortex center and the increased high-PV volume during the vortex-merging period. In this and the next sections, we attempt to quantify the dynamical processes accounting for the vortex-merging scenarios and the roles of CGVs in the ITCZ in the genesis of TS Eugene through the PV budget analysis. So far, the low- to midlevel concentration of PV has been discussed more or less in the context of PV-substance conservation.

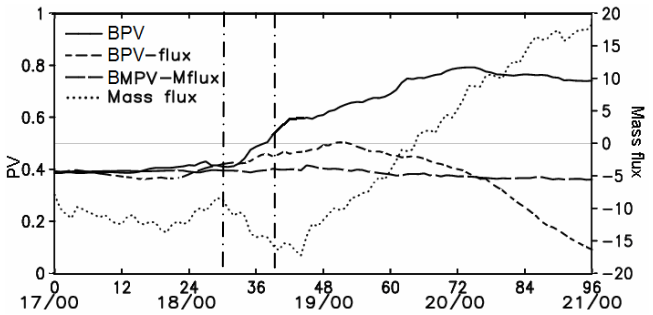

Figure 2.14. Time series of the BPV (in PVU unit) from the hourly model outputs: BPV (solid), BPV after subtracting the net PV flux at the boundaries (short-dashed), BMPV after subtracting the net mass-weighted PV flux at the boundaries (long-dashed) for a control volume of 720 km × 720 km × 10 km following V_2 until 18/18-42 and then Eugene. The corresponding total mass flux is also plotted (dotted, 10^7 kg s^{-1}).

Indeed, Fig. 2.14 shows that the volume-integrated (or bulk) mass-weighted PV (BMPV) is nearly conserved for a control volume of 720 km × 720 km × 10 km either

prior to (with the same horizontal domain as shown in Figs. 2.12 and 2.13) or after the merger, provided that the mass-weighted PV fluxes through all the boundaries are subtracted, including the PV fluxes of V_1 into the control volume. This BMPV conservation, however, does not imply the conservation of the total PV within the control volume or any grid box. In fact, one can see immediately from Eq. (2.2) that even if there is no flux of BMPV across the lateral boundaries, the total PV could change substantially if there is net mass loss or gain in the volume. Moreover, different rates of the mass changes in the vertical could determine the vertical redistribution of PV, particularly during the deepening stage of TCs. Apparently, while the BMPV results are useful for the understanding of its conservative properties, they do not quantify the dynamical processes associated with the PV changes shown in Figs. 2.12 and 2.13.

In this study, we choose to examine the PV budgets following the storm, starting from the nonhydrostatic PV equation of HM87:

$$\frac{\partial q}{\partial t} = -\vec{u} \bullet \nabla q + \frac{1}{\rho} \nabla \bullet (H\vec{\omega} + \vec{F} \times \nabla \theta), \tag{2.3}$$

where $\vec{u}$ is the 3D wind field, H is the 3D diabatic heating rate, and $\vec{F}$ is the 3D frictional force. Although Eq. (2.3) is useful for estimating the spatial structures of PV budgets in TCs, it would be more meaningful to use the area- or volume-averaged PV budgets that could distinguish internal PV forcing processes from the boundary fluxes, especially when the time evolution of the storm-scale integrated quantities in a storm-relative system is examined. In the latter case, Eq. (2.3) has to be written as the volume-averaged or bulk PV (BPV) following the storm,

$$\frac{d}{dt}\left(\int_{V(t)} qdV\right) = \int_{V(t)} \frac{\partial q}{\partial t} dV + \int_{S} q\vec{U} \bullet \vec{n} dS$$

$$= -\int_{V(t)} (\vec{u} \bullet \nabla q) dV + \int_{V(t)} \frac{\nabla \bullet (H\vec{\omega})}{\rho} dV + \int_{V(t)} \frac{\nabla \bullet (\vec{F} \times \nabla \theta)}{\rho} dV + \int_{S} q\vec{U} \bullet \vec{n} dS, \quad (2.4)$$

where $\vec{U}$ is the movement of the lateral boundaries and a volume averaging [i.e., dividing by *V(t)*] has been implicitly assumed for all the terms. The area-averaged PV budgets can also be estimated by applying the area integration to all the terms in Eq. (2.4). After reorganizing the first and last terms on the rhs and using $\nabla \bullet \vec{\omega} = 0$, Eq. (2.4) can be rewritten in a more meaningful form as

$$\frac{d}{dt}\left(\int_{V(t)} qdV\right) = \int_{V(t)} (q\nabla \bullet \vec{u}) dV + \int_{V(t)} \frac{\vec{\omega} \bullet \nabla H}{\rho} dV + \int_{V(t)} \frac{\nabla \bullet (\vec{F} \times \nabla \theta)}{\rho} dV + \int_{S(t)} q(\vec{U} - \vec{u}) \bullet \vec{n} dS. \quad (2.5)$$

Eq. (2.5) states that the time rate of BPV changes (QTEN) is determined by the terms on its rhs, which are from left to right the condensing or diluting rate of PV due to the 3D velocity divergence (QCON), the diabatic PV-production rate (QH), the divergence of $\vec{F}$x$\nabla\theta$, and the net across-boundary PV fluxes (QBND) between the 3D normal-to-boundary flows (QFLX) and the control volume's movement (QMOV). Note that because 3D divergence is proportional to minus the time rate of density changes (i.e., - d lnρ/dt), QCON is related ultimately to the mass exchange of the control volume with its surrounding environment. All the rhs terms are averaged with the total volume and calculated with the hourly, 1.33-km resolution model output, including the heating rate *H*.

In this study, the control volume, following V_2 prior to merger and then Eugene after its formation, is defined with the top boundary at z = 11.5 km to minimize the

impact of high PV in the stratosphere on the budget calculations and the bottom boundary at z = 1.5 km, which is slightly above the PBL, to eliminate the PBL effects (i.e., $\vec{F}$x$\nabla\theta$) on the PV budgets (2.5). It is evident that QCON and QH represent the internal sources/sinks of PV in the absence of the PBL effects and that diabatic heating is the driving force for the generation of PV, whereas QBND denotes external sources or sinks of PV. To make sure that the budget residues are small for the purpose of this study, we have compared the rates of the BPV changes calculated from the lhs term of Eq. (2.5), given in Fig. 2.15a, to those obtained by summing up all the rhs forcing terms during the 4-day integration, and noticed that the differences between the two approaches are small (not shown). In the next, we will refer to Eqs. (2.3) and (2.5) as simply the PV budget and the bulk PV budget, respectively; similarly for the vertical absolute vorticity budgets to be discussed in Chapter 10.

It should be mentioned that the budget equations (2.3) and (2.5) would differ considerably when they are written in isobaric or isentropic coordinates. That is, because of the use of hydrostatic approximation, only the vertical component of the absolute vorticity is often considered in these coordinate systems. As will be seen in the next subsection, the horizontal components of the relative vorticity become increasingly important in intensifying TCs, particularly in hurricanes, due to the presence of large vertical wind shear. Without the representation of horizontal vorticity, PV, defined as a scalar multiplication of the 3D absolute vorticity vector and the gradient of potential temperature, might not be meaningful to the understanding of PV structures and evolution of TCs, especially to its conservative property. Thus, PV in height coordinates is used in the present study since it is treated most completely with both the vertical and horizontal components of absolute

vorticity.

6.3. PV budget analysis

To see to what extent the PV equation can be used to characterize the vortex-merging processes and the role of CGVs in the ITCZ during the life cycle of Eugene, we consider first the time series of the bulk PV budget. It is evident from Fig. 2.14 that the BPV associated with V_2 increases slowly prior to merger (i.e., 18/06-30), moderate to sharply during its merging with V_1 (i.e., from 18/12-30 to 18/18-42), steadily until Eugene reaches its maximum intensity at 19/18-66, and slowly decreases shortly after; these sequences correspond reasonably well to the aforementioned four phases of Eugene's life cycle (cf. Figs. 2.14 and 2.11b). Similar scenarios can also be seen from the time series of the BPV tendency (cf. Figs. 2.14 and 2.15a). The BPV doubles in magnitude, i.e., from 0.4 to 0.8 PVUs in about 40 h during the intensifying period. Note that the sharp increase in BPV (i.e., 0.2 PVUs in 9 h) coincides well with the amplification of PV in the low- to mid-troposphere during the merging phase (cf. Figs. 2.14 and 2.12). Of importance is that about 30% of the increased BPV during this phase is generated by internal dynamics, after taking into account the PV fluxes through the lateral boundaries (i.e., the BPV-Mflux curve in Fig. 2.14). Note also that the increased BPV rates coincide well to the net mass loss in the control volume, which is peaked after the merger at 18/21-45. As will be shown in the next, these mass losses imply the important roles of QCON in determining the evolution and changes of the BPV and TC intensity.

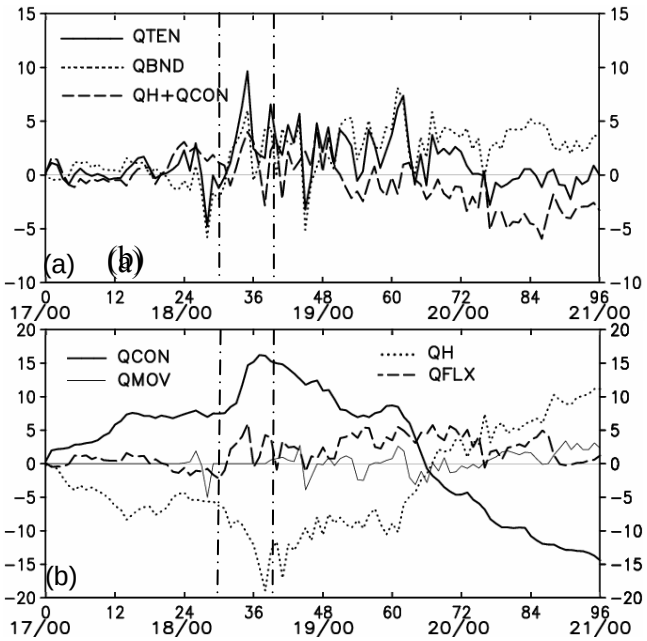

Figure 2.15. As in Fig. 2.14 but for (a) the BPV tendency (solid), the net boundary PV fluxes (dotted), and the sum of the PV condensing and heating-generation rates (dashed); and (b) the PV condensing rate (solid), the PV generation rate by diabatic heating (dashed), the PV boundary flux due to normal flows (dotted) and to the movement of the control volume (thin solid). The unit is 10^{-6} PVU s^{-1}.

Since the BPV time series could describe well the genesis and dissipation of Eugene, it is desirable to quantify the contributions of different forcing terms on the rhs of Eq. (2.5) to the time rates of the BPV changes. First, it is necessary to understand the contributions of the net boundary PV fluxes (i.e., QBND), due to the advection of VHTs and meso-γ vortices in the ITCZ mostly through the western boundary (see Figs. 2.12 and 2.13). Fig. 2.15b shows pronounced inward PV fluxes (QFLX) into the control volume at all times, with a sharp jump occurring between 18/06-30 and 18/12-36 as V_1 moves continuously into V_2's circulation (see Fig. 2.13). Because of the intermittency of vortices at different scales entering the control volume, QFLX (and QTEN) exhibits significant fluctuations. In contrast, the PV fluxes due to the movement of the control volume (QMOV) are relatively small, and vary smoothly with time. Thus, in general, the net PV boundary fluxes (i.e., QBND =

QFLX + QMOV) contribute positively to the intensification of Eugene due to the inward fluxes of vortices in the ITCZ, even during decaying phase (Fig. 2.15a). Despite such continuous contributions of the PV fluxes to QTEN, the BPV decreases slowly after 20/00-72, suggesting that some internal dynamical processes may determine the weakening of Eugene.

The internal dynamical processes are closely related to the following two distinct forcing terms of the BPV: QCON and QH, which are similar in magnitude but opposite in sign (Fig. 2.15b). That is, QCON is a net source (sink) when the mass in the control volume decreases (increases) (cf. Figs. 2.15b and 2.14) whereas QH is a net sink (source) during the intensifying (weakening) stage (cf. Figs. 2.15b and 2.16). The time series of QH looks somewhat noisier than that of QCON due to the large variability in diabatic heating gradients associated with deep convection within the ITCZ. Of interest is that QCON contributes positively to the total budget from the early development to the maximum intensity of Eugene near 19/18-66, after which time it switches to a negative sign. In particular, QCON exhibits a sharp increase as V_1 moves northwestward and rolls up the PV bands within V_2 during the merging phase. This sharp increase implies the rapid increase of 3-D divergence that results from the rapid expansion of air parcels as they ascend in the intensifying vortex circulation in which the motion is mostly upward. This is consistent with the rapid mass loss and the increased condensing rate of PV during the merging phase (cf. Figs. 2.15b and 2.14). Similarly, the more negative contribution of QCON after 19/18-66 is closely associated with the increasing mass gain or the dilution of PV in the control volume during the decaying stage.

By comparison, the forcing term QH associated directly with diabatic heating

shows the time rates of changes that are opposite to QCON, i.e., with negative contributions during the early and intensifying periods and positive contributions at the decaying stage (i.e., after 19/18-66) during which stratiform rainfall with an upper-level heating maximum tends to dominate. Such negative contributions of QH to the BPV production during the intensifying stage appears at first to contradict our common intuition. This issue could be understood by decomposing QH into vertical and horizontal components during the three different phases, as related to the 3D heating gradients and vorticity vectors (see Fig. 2.16). For example, the horizontal part of QH [i.e., $QH_{xy} = (\vec{\omega}_{xy} \bullet \nabla_h H)/\rho$ where $\vec{\omega}_{xy}$ and $\nabla_h H$ are the horizontal component of the relative vorticity and heating gradients, respectively], often neglected in previous studies, turns out to be very significant and is mostly negative (see Figs. 2.16d – 2.16f). Specifically, $\vec{\omega}_{xy}$ and $\nabla_h H$ are highly asymmetric during the genesis stage in which diabatic heating occurs mostly in the eastern portion of the control volume (Fig. 2.12). As will be seen in the next subsection, this tends to generate positive horizontal vorticity (i.e., $\vec{\omega}_{xy}$ points outward) and negative heating gradients in the eastern half volume, and opposite signs in the western half volume in the low- to mid-troposphere during the genesis stage. In contrast, the vertical part of QH, i.e., $QH_z = (\eta \partial H/\partial z)/\rho$ where η is the vertical component of absolute vorticity, is relatively easier to visualize for the given vertical profiles of H and η (see Figs. 2.16a – 2.16c). That is, QH_z exhibits positive (negative) contributions below (above) the peak heating level, with larger magnitudes in the PBL and near z = 5 km where, as will be seen later, the melting level is located. Because air density decreases exponentially with height, a skewed vertical distribution of $(\eta \partial H/\partial z)/\rho$ would result, with comparable magnitudes aloft despite the presence of small η; similarly for the

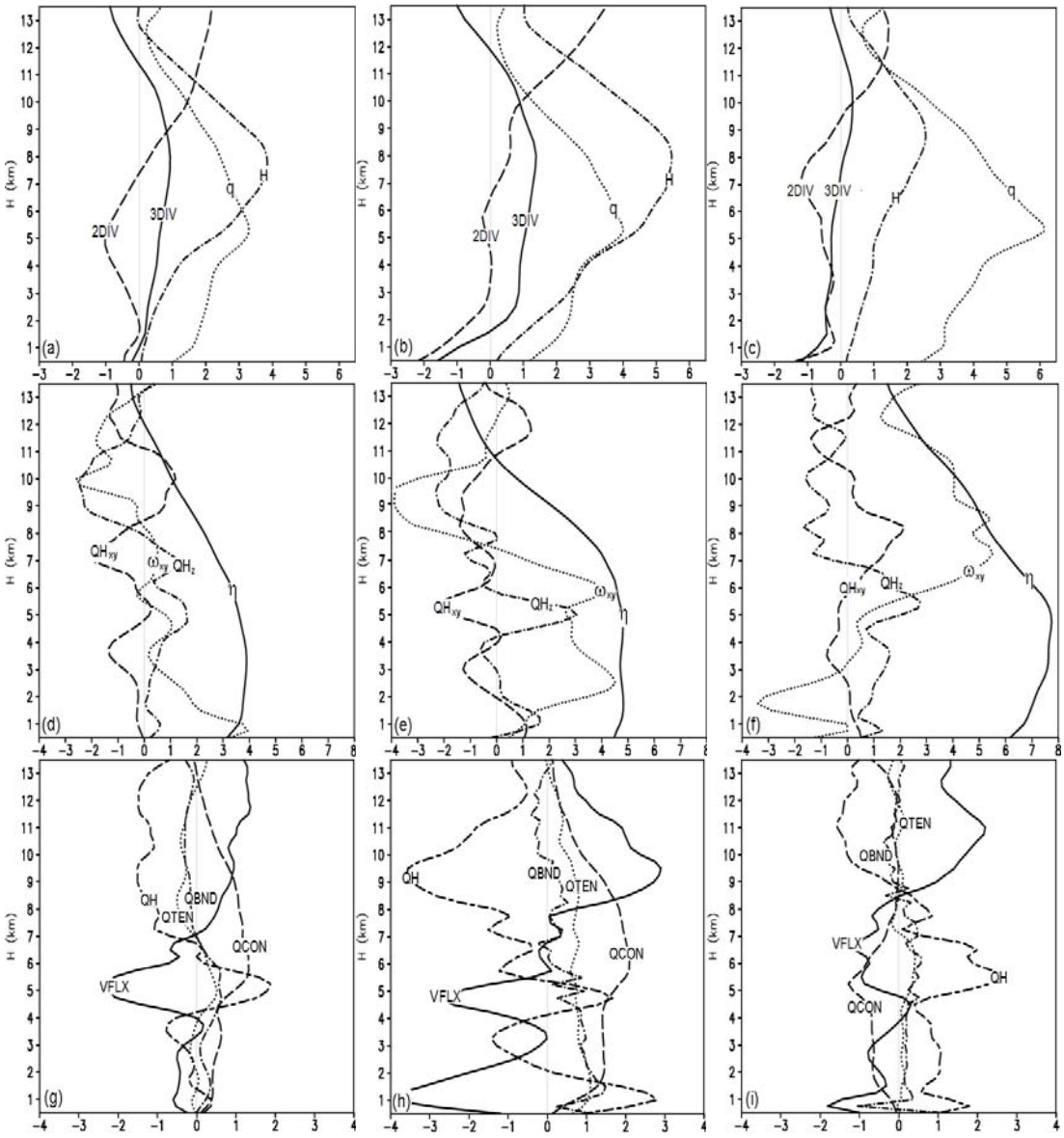

Figure 2.16. Vertical profiles of the control (720 km × 720 km) area-averaged quantities. Upper panel: PV (q, dotted, unit: 0.2 PVU), 3D velocity divergence (3DIV, solid, unit: 10^{-5} s^{-1}), and diabatic heating rates (H, dot-dashed, unit: 2×10^{-4} K s^{-1}), and 2D divergence (2DIV, dashed, unit: 10^{-5} s^{-1}); Middle panel: the vertical (η, solid, unit: 10^{-5} s^{-1}) and horizontal (ω_{xy}, dotted, unit: 5×10^{-4} s^{-1}) components of the absolute vorticity, the vertical (Q_z, dashed) and horizontal (Q_{xy}, dot-dashed) contributions of QH; Bottom panel: QH (short-long dashed), QCON (dashed), the net boundary PV flux divergence (QBND, dot-dashed), vertical PV flux divergence (VFLX, i.e., $\partial(wq)/\partial z$, solid) and QTEN (dotted). All the PV forcing terms have the unit of 10^{-5} PVU s^{-1}. The left, middle and right columns are for 18/03-27, 18/12-36, and 20/00-72, respectively.

vertical distribution of $QH_{xy} = (\vec{\omega}_{xy} \bullet \nabla_h H)/\rho$. Summing up the vertical and horizontal parts of QH gives the diabatic-PV destruction in most portions of the troposphere during the genesis stage except in the PBL and near the melting level due to the large positive contributions of $(\eta \partial H/\partial z)/\rho$. This is consistent with the net negative QH contributions to QTEN up to Eugene's maximum intensity at 19/18-66 (cf. Figs. 2.16h, 2.15b and 2.11b). During the decaying stage (see Figs. 2.16c and 2.16f), the vertical part of QH tends to dominate its horizontal part, due mostly to the decreasing tangential winds and increasing ratio of $(\partial H/\partial z)/\nabla_h H$. Thus, QH switches to a positive sign in the deep troposphere, whereas QCON becomes negative, after reaching the maximum storm intensity (cf. Figs. 2.16i and 2.15b). Note that during the weakening stage (i.e. after 20/00-72), Eugene has a well-defined flow structure but with the peaked absolute vorticity around z = 5km (Fig. 2.16f). This indicates that the tangential flow overall increases from the surface to the level of the peaked vorticity before it decreases, thus implying that ω_{xy} is pointing inward below z = 5 km. Due to the weakening of Eugene as it migrates into the colder SST, latent heating decreases substantially (cf. Fig. 2.16c), and such negative ω_{xy} could not have much contribution to QH_{xy} as seen in Fig. 2.16f.

It should be pointed out that unlike their volume-integrated counterparts, QCON and QH do not cancel out at individual levels, but show significant differences in their vertical distributions. That is, QH flips signs above and below the melting level during the intensifying stage whereas QCON remains positive throughout the troposphere with its peak located slightly above the melting level (see Figs. 2.16g and 2.16h). Nevertheless, the two forcing terms are either directly or indirectly related to diabatic heating, and should be treated as one net diabatic forcing in the bulk PV

budget. One can see from Fig. 2.15a that on average the net forcing (QCON + QH) contributes positively to QTEN prior to 19/03-51 but negatively afterwards. Clearly, the storm could still experience a further deepening period, i.e., from 19/03-51 to 19/18-66 (cf. Figs. 2.15a and 2.11b), because of the continued supply of high PV from the ITCZ through the western boundary of the control volume. This implies that without the contribution of QBND, Eugene would become much shorter-lived, under the influence of intense vertical wind shear. Subsequently, the destructive effects of QCON due to the dilution of PV are more or less balanced by the positive contributions of QBND and QH, thereby keeping the BPV tendency nearly null during the decaying stage (cf. Figs. 2.14 and 2.15a,b). This implies that the BPV is not a good indicator for TC intensity during the decaying phase due to the storm-environment interaction.

While QCON and QH should be treated as one net forcing term in the bulk PV budget, it is necessary to consider them separately for the PV budget since they do not cancel out at individual levels. Figs. 2.16g-2.16i show that the residues between QCON and QH are balanced by the vertical PV flux divergence included in QBND (i.e., $\partial wq/\partial z$, where w is the vertical motion in height coordinates), which accounts for the upward transport of PV. Evidently, the vertical PV flux divergence is negative (positive) below (above) the peak PV and vertical motion level, which is opposite in sign but similar in magnitude to the sum of QCON and QH. The net result is that PV increases slowly only in a shallow layer near the melting level prior to merger and during the decaying stage (Figs. 2.16g and 2.16i), but *at larger rates in the deep troposphere with the peak magnitude near the top of the PBL during the merging period* (Fig. 2.16h). The latter result is important for the examination of the previous

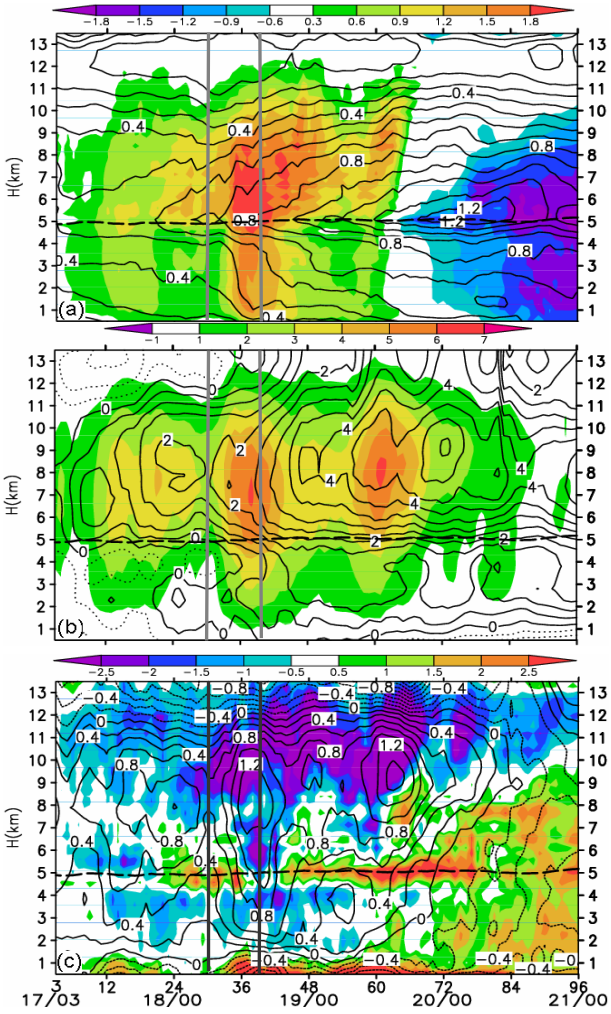

Figure 2.17. Height-time cross sections of the (720 km × 720 km) area-averaged quantities from the hourly model outputs: (a) PV (solid, every 0.1 PVU), and QCON (shaded, every 0.3 × 10^{-5} PVU s^{-1}); (b) diabatic heating rates (shaded, every 0.2 × 10^{-3} K s^{-1}) and the potential temperature deviation from its initial value (solid, every 0.5 K); and (c) 3DIV (solid, every 0.2 × 10^{-5} s^{-1}) and QH (shadings, at intervals of 10^{-5} PVU s^{-1}). Thick-dashed lines denote the melting level.

top-down versus bottom-up hypothesis in the case of vortex merger, namely, *the positive PV tendency tends to be greater in the lower troposphere rather than at the midlevel*. The continued midlevel positive PV tendency during the intensifying period is consistent with the development of the peak PV near the melting level, e.g., from

0.6 PVU at 18/03-27 to 0.8 PVU at 18/12-36, and 1.2 PVUs at 20/00-72 (cf. Figs. 2.16a-2.16c).

6.4. Vortex-merging dynamics

To see how representative the vertical distribution of the above area-averaged PV budget is, Fig. 2.17 shows the height-time cross sections of the area-averaged PV, potential temperature perturbation (θ') with respect to the initial vertical profile, and 3D divergence, superimposed by the PV forcing terms on the rhs of Eq. (2.5). First, the storm's PV keeps increasing in the deep troposphere, coinciding with the positive forcing of QCON (but mostly negative forcing of QH), until shortly after the intensifying stage. As mentioned before, the peak PV amplitudes always remain slightly above the melting level (i.e., z = 5 km) with large vertical gradients below (Fig. 2.17a). All the other variables also exhibit larger vertical gradients in the vicinity of the melting level, e.g., H, QH, 3DIV and θ'. This is because the melting cooling below and freezing warming above tend to produce locally large vertical gradients in heating rates (H) and the net warming (θ') profiles, which in turn increases QH through $(\eta \partial H/\partial z)/\rho$, as have also been shown in Fig. 2.16, assisting partly in the growth of PV above the melting level. Larger vertical gradients also appears in the decreasing density rates (3DIV) and PV condensing rates through QCON (Figs. 2.17b,c). All these indicate the important roles of melting and freezing in affecting the vertical structures of PV, diabatic heating and mass convergence during TCG and the life cycle of TCs.

Of relevance to the merger dynamics is the substantial PV increases in the lower troposphere during the merging phase, i.e., with higher PV extending downward to the PBL. This is consistent with the positive PV tendency in both the

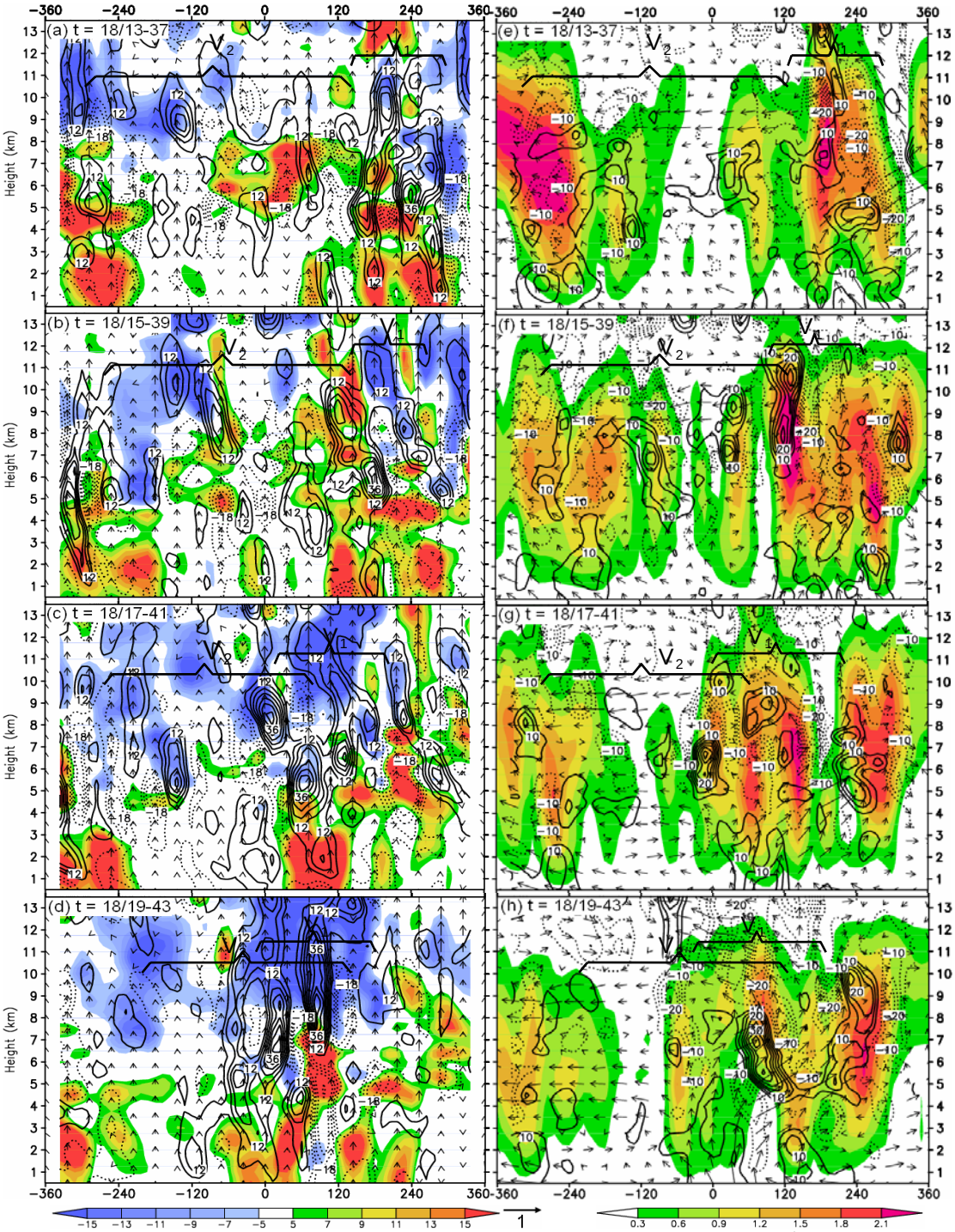

Figure 2.18. As in Fig. 2.12, but (a) – (d) for the 3D advection of PV (i.e., $-\vec{u}\bullet\nabla q$, every 5 × 10^{-5} PVU s^{-1}), superimposed with the vertical component of the diabatic PV generation rates (i.e., $\rho^{-1}\eta\partial H/\partial z$, shadings); and (e) –(h) for the diabatic PV generation rate (i.e., $\rho^{-1}\vec{\omega}\bullet\nabla H$, every 5 × 10^{-5} PVU s^{-1}), superposed with the diabatic heating rates (shaded at intervals of 3 × 10^{-4} K s^{-1}) and in-plan absolute vorticity vectors ($\vec{\omega}_{xz}$) during the merging period between 18/13-37 and 18/19-43. Note that η has been multiplied by 10 in constructing the $\vec{\omega}_{xz}$ vectors. Solid (dashed) lines are for positive (negative) values.

bulk and area-averaged vertical profiles (cf. Figs. 2.15 and 2.16e). As shown earlier, the low-level PV increases could be attributed mostly to the merging CGVs at different scales in V_2 and the subsequent decreases in air density through QCON (cf. Figs. 2.12, 2.13, and 2.17a,c), and partly to the positive contributions of QH in the PBL through $(\eta \partial H/\partial z)/\rho$ (cf. Figs. 2.17b,c and 2.16e). In other words, most of the lower-level increases of PV are not the "downward growth" of the midlevel PV associated with the merging MCVs, but caused by the decreasing air mass associated with the same amount of PV substance within the same isentropic layers.

To help understand better the diabatic generation of PV, Fig. 2.18 shows the vertical cross sections of the PV budget terms of Eq. (2.3) during the merging phase. A comparison of Figs. 2.12 and 2.18a-d reveals some similarities between the local PV tendencies and the PV advection, as shown by couplets of positive and negative patches ahead of and behind propagating CGVs, respectively. This indicates that a large portion of local PV changes is related to the redistribution of PV within the storm, as more PV patches move toward the merger's center. The PV advective patterns become well organized after 18/17-41 when PV patches wrap around Eugene (Fig. 2.18d). Similarly, the diabatic generation rates also exhibit couplets of positive and negative patches, but around the local heating maximum (see Figs. 2.18e-h). This is understandable when the diabatic generation is examined in the form of $\rho^{-1}\vec{\omega} \bullet \nabla H$, which can be seen through vertical cross sections of in-plan absolute vorticity vectors ($\vec{\omega}_{xz}$) and diabatic heating rates given in Figs. 2.18e-h. Apparently, the vorticity vectors exhibit more upward (i.e., positive) component in the vicinity of the merger, especially in the lower and upper troposphere. Most of them turn eastward (i.e., positive) in the midtroposphere or westward aloft due to the increase and decrease of

tangential winds with height, respectively. When coupled with the diabatic heating gradients (∇H), we can see PV generation in the lower troposphere and between the melting and peaking heating level, and large PV destruction aloft due to the contributions of its vertical component (i.e., $\eta \partial H/\partial z)/\rho$) (also see Figs. 2.18a-d), as mentioned before. Large PV destruction also occurs ahead of the heating center along the vorticity vectors, which are attributable to the horizontal component (i.e., $\omega_x \partial H/\partial x)/\rho$). Clearly, the PV magnitude can increase rapidly in air parcels when they are advected through the diabatic generation regions, e.g., in the lower troposphere, between the melting and peak heating levels. On the other hand, air parcels would experience rapid decreases in PVUs when they are advected above the peak heating level or ahead of active convective regions along the vorticity vector (cf. Figs. 2.17c and 2.18). Despite the net negative contributions in the BPV, mostly at the upper levels, diabatic heating accounts for the rapid increase of local PV, peaked near the melting level.

6.5. Bottom-up cyclogenesis

The bottom-up and top-down hypotheses of TCG associated with MCVs, discussed by Zhang and Bao (1996), Bister and Emanual (1997), Ritchie and Holland (1997), and Hendrick et al. (2004), are based on the vorticity dynamics, which could not be easily derived from the PV budgets presented in the preceding chapter. Thus, in this chapter, we examine the budgets of the vertical absolute vorticity (η) to determine which of the above mechanisms is operative in the present vortex merger case.

The time-height cross section of the control-area averaged η, given in Fig. 2.19a, shows the presence of larger cyclonic vorticity (about 3×10^{-5} s^{-1}) below the

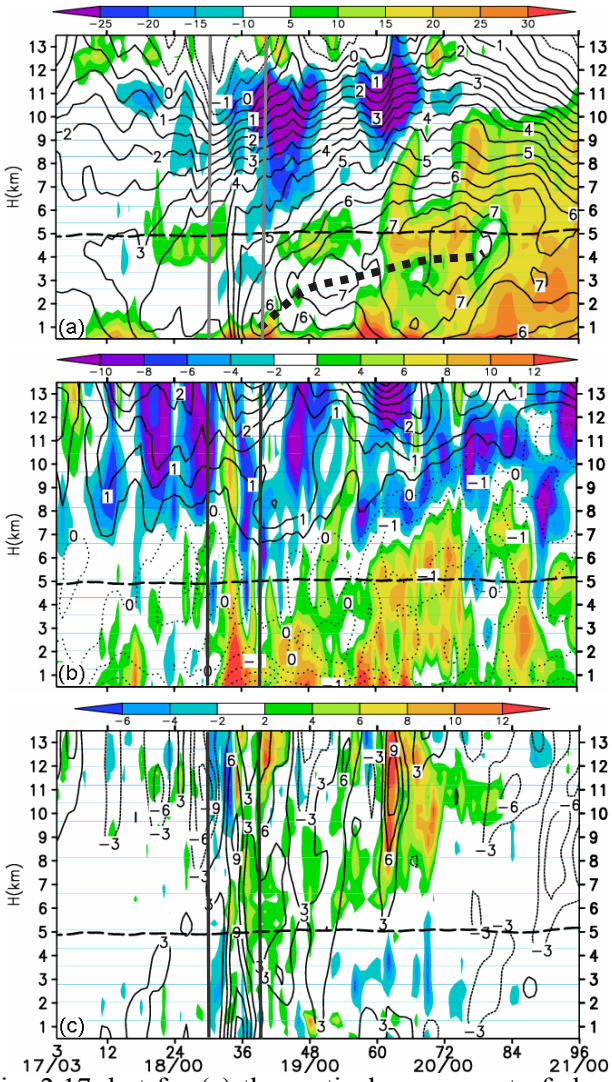

Figure 2.19. As in Fig. 2.17, but for (a) the vertical component of absolute vorticity (every 10^{-5} s^{-1}), and the stretching rates (shaded, every 5×10^{-10} s^{-2}); (b) the bulk stretching rates (shaded, every 10^{-10} s^{-2}) and 2DIV (contoured, every 10^{-5} s^{-1}); and (c) the bulk tilting rates (shaded, every 10^{-10} s^{-2}) and the absolute vorticity tendency (solid, every 3×10^{-10} s^{-2}). Bold-dashed lines in (a) are for the ridge axis of the absolute vorticity.

melting level associated with V_2 and slow growth during the pre-genesis phase, but significant vorticity growth as V_1 and V_2 are merging, followed by continued slower amplifications until reaching the maximum vorticity of greater than 7.5×10^{-5} s^{-1} near 20/00-72. Like the PV structure, η-isopleths also become upright from the peak η level down to the surface during the merging phase. However, this η-isopleth

structure could not tell whether or not such η-growth occurs from the top downward or the bottom upward. Thus, the local vorticity tendency is provided in Fig. 2.19c, which shows that the vorticity growth occurs in the deep troposphere during the merging phase, but *the most rapid rates appear in the PBL* due to the important contribution of stretching associated with the frictional convergence (Figs. 2.19a,c). In general, the vortex stretching has a secondary maximum at the melting level where midlevel convergence is pronounced, but this secondary maximum appears to be insignificant during the merging phase due partly to the more dominant condensational heating than the melting cooling associated with less falling precipitation particles. Of interest is that the peak absolute vorticity, growing with time, is elevated from the PBL at the time of merging to a layer near the melting level at 20/00-72. Unlike in Zhang and Bao (1996), the peak vorticity could not be maintained in the PBL because of the negative impact of the vertical shear-induced moist downdrafts on the mass convergence in the PBL.

Since the time evolution of the area-averaged local vorticity tendency, shown in Fig. 2.19c, includes the internal vorticity forcing, 3D advection and external vorticity fluxes through the lateral boundaries, it is more meaningful to estimate the absolute vorticity budgets in flux form following HM87, like the bulk PV budgets, i.e.,

$$\begin{aligned}\frac{\partial \eta}{\partial t} &= -\frac{\partial}{\partial x}\left(u\eta + w\frac{\partial v}{\partial z} - F_y\right) - \frac{\partial}{\partial y}\left(v\eta - \frac{\partial u}{\partial z} + F_x\right) + SOL \\ &= -\left[\frac{\partial (u\eta)}{\partial x} + \frac{\partial (v\eta)}{\partial y}\right] - \left[\frac{\partial}{\partial x}\left(w\frac{\partial v}{\partial z}\right) - \frac{\partial}{\partial y}\left(w\frac{\partial u}{\partial z}\right)\right] + \left[\frac{\partial F_y}{\partial x} - \frac{\partial F_x}{\partial y}\right] + SOL\end{aligned} \tag{2.6}$$

where the rhs terms of Eq. (2.6), upon taking volume integration and averaging, represent the fluxes of vorticity forcing through the lateral boundaries, which may be viewed as the bulk stretching, tilting, frictional and solenoidal contributions,

respectively, to the rates of change of the circulation over the control area. Because the last two rhs terms appear to be much smaller than the first two terms except in the lowest boundary layers, they are ignored for the purpose of our vorticity budget analysis.

Fig. 2.19b shows that the elevation of the peak absolute vorticity with time could be attributed mainly to the bulk stretching in the presence of 2D convergence growing in depth below the heating maximum. Again, the bulk stretching is peaked in the PBL with a secondary maximum near the melting level, but on average it grows smoothly in depth with time, as does the 2D convergence, as the storm-scale precipitation evolves from convective to stratiform. Moreover, the merging phase is dominated by the positive bulk stretching in the deep troposphere, unlike the area-averaged stretching, with the maximum rate occurring at the surface (cf. Figs. 2.19a,b). *This deep layer stretching could be clearly attributed to the rapid increase in diabatic heating during this phase*. This result conforms to the vertical structures of the bulk local η-tendency (cf. Figs. 2.19b,c), and confirms further the more rapid growth of cyclonic vorticity in the bottom layers. By comparison, the bulk tilting generally contributes much less to the η-tendency, except at the merging stage (i.e., 18/10-34) and peak intensity (19/15-63) at which it accounts for the significant cyclonic tendencies in the upper troposphere due to the development of strong upward motion (or latent heat release) and larger differences in vertical wind shear between the inner and outer regions (cf. Figs. 2.19c, 2.11b and 2.17b).

Fig. 2.20 shows how the vertical structures of the absolute vorticity (η) evolve with time as the two MCVs approach, and then merge to form TS Eugene. The η structures prior to merger are featured with a midlevel volume of intense vorticity

associated with V_1 and a loosely defined V_2 (Figs. 2.20a,b). As shown in Chapter 8, V_1 intensifies at the expense of V_2 through enhanced deep convection, leading to the development of a surface low beneath V_1 (see Fig. 2.20 therein). As a result, the frictional and convectively induced 2D convergence begins to generate cyclonic vorticity in the PBL, and the enhanced divergence above tends to weaken the cyclonic vorticity of V_1 centered at z = 7 km. Thus, the largest positive local η-tendencies first appear in the bottom layers (Fig. 2.20a) and then extend upward during the merging and intensifying period (Figs. 2.20b – 2.20f); there is little evidence of the η-growth tendency from the midlevel downward. The depth of positive η-tendencies grows with time, and reaches z = 10 km, which is consistent with intense convective developments in the eastern half circulation of the storm (cf. Figs. 2.10 and 2.20f). Similarly, the intensifying cyclonic vorticity begins from the PBL (Fig. 2.20a) and extends to a deeper layer with time (Figs. 2.20b-2.20f); there is little physical connection between the lower-level η-growth and the midlevel vortices until the merger is completed. Clearly, this bottom-up η-growth contradicts the top-down η-growth hypothesis of Ritchie and Holland (1997) during the MCVs merging period.

In contrast, negative η-tendencies occur in a layer in the upper troposphere that is much deeper than that of the positive η-tendencies. This explains why the midlevel cyclonic vorticity weakens due to the presence of strong 2D divergence during the initial merging stage (Figs. 2.20b,c,d), and then appears to intensify slightly due to the upward vorticity advection in the presence of strong updrafts. Nevertheless, the vertical distribution of a shallow-layer positive η-tendencies below a deep-layer negative η-tendencies accounts for the generation of a well-defined deep mesoscale

vorticity field with the peak intensity near the top of the PBL (Figs. 2.20e,f). The vertical cross-sectional η-structures, shown in Fig. 2.20f, are similar to those obtained by Zhang and Bao (1996b).

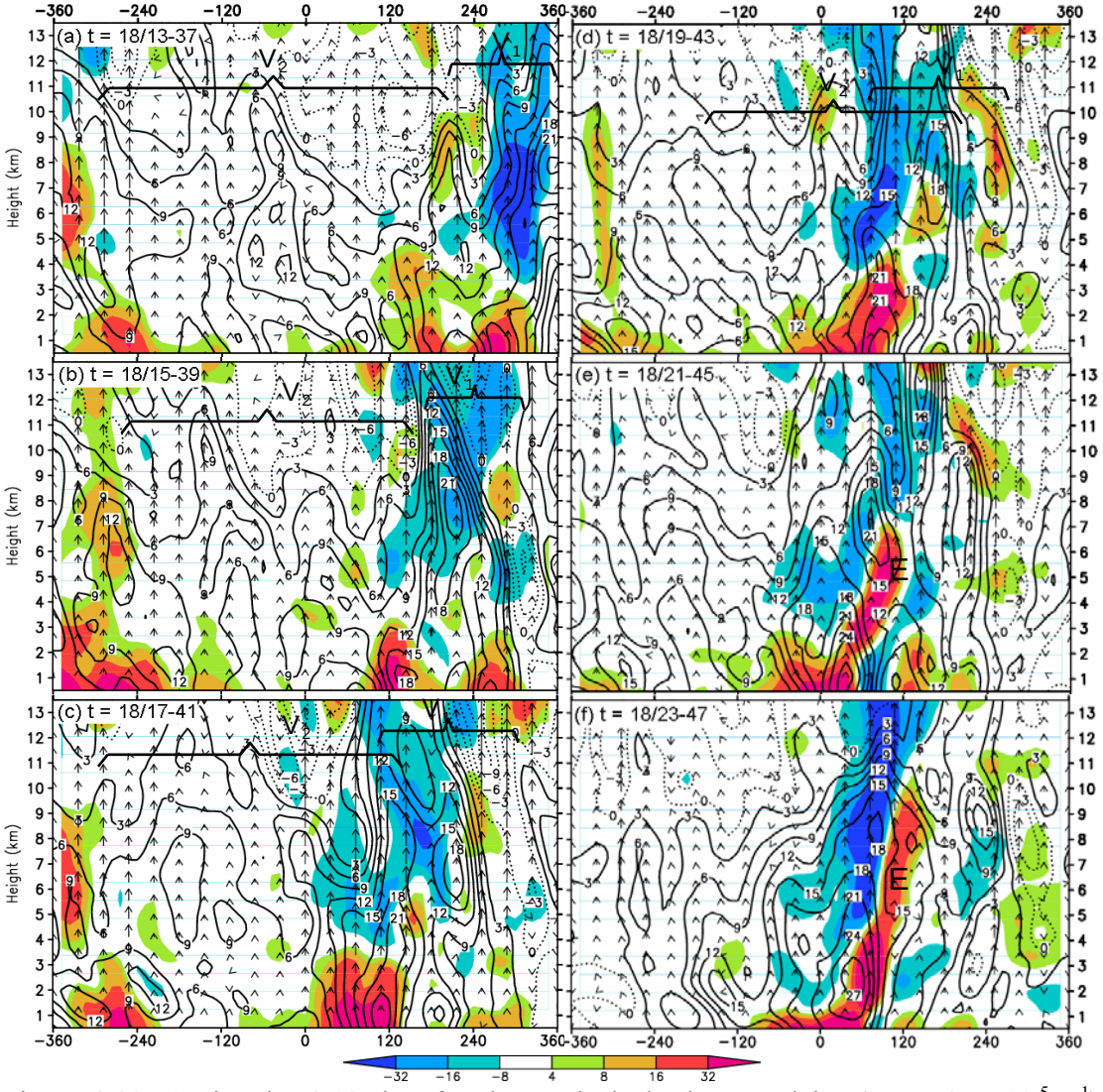

Figure 2.20. As in Fig. 2.12, but for the vertical absolute vorticity (every 3×10^{-5} s^{-1}) superimposed with its total tendency (shaded at intervals of 4×10^{-9} s^{-2}) during the period of 18/13-37 – 18/23-47. Solid (dashed) lines are for positive (negative) values.

Of particular relevance to this study is that unlike PV, *the vortex merger does not cause an increase of the midlevel absolute vorticity* (cf. Figs. 2.12 and 2.20) since it cannot adiabatically lead to the midlevel convergence or any other positive vorticity forcing. In fact, Fig. 2.19a exhibits near-vanishing to negative net stretching of the absolute vorticity between the melting level and the PBL during the merging phase. This confirms further that the downward growth of cyclonic vorticity would unlikely occur either adiabatically or diabatically during the merging phase. However, as shown in Chapter 8, the tangential winds at the rim of the merger (and its circulation scale) do increase from the midlevel downward with weak flows near the TC center (see Fig. 2.10), which presumably occurs after the merged CGVs are symmetrized. Obviously, without deep convection, even when two MCVs are perfectly superposed in the vertical, stronger horizontal convergence would likely take place in the PBL where larger surface pressure falls occur with cross-isobaric flows, and the cyclonic vorticity would grow first in the PBL. The midlevel flows would still remain rotational with little cross isobaric component.

While there is little physical connection between the η-growth in the PBL and midlevel MCVs or peak PV, they are all indirectly related through the dynamical balance. Specifically, as a deep layer (i.e., from the PBL to the peak heating level) of PV increases in magnitude during the intensifying stages (Fig. 2.17a), both the mass and wind fields will adjust to the increased PV according to the invertibility principle (Hoskins et al. 1985). This adjustment takes place throughout the vertical column, but with the maximum downward deformation of isobaric surfaces at the lowest levels, especially in the presence of a warm core from low- to upper- levels (Fig. 2.17b). This is consistent with the more rapid central pressure falls during the merging phase (Figs.

2.9 and 2.10). Based on the quasi-balanced PV-omega system (e.g., Wang and Zhang 2003), we may expect the low-level convergence induced by friction and latent heating to generate cyclonic vorticity in the bottom layer first. Since the η-growth through vortex stretching is exponential, especially in the presence of intense updrafts at the MCV scale, the intensifying absolute vorticity would extend upward to form a deep layer of cyclonic rotation. As PV becomes more dominated by its vertical component (i.e., $\eta\partial\theta/\partial z$) during the weakening stage, the peak absolute vorticity is elevated close to a level (i.e., the melting level) where the peak PV is located (cf. Figs. 2.17a and 2.19a). In this case, both η and $\partial\theta/\partial z$ are large below the melting level (also see Figs. 2.16e,f). In other words, the vertical distribution of PV would differ from that of η when the peak rotation occurs at the lower levels due to the important contributions of the horizontal vorticity (see Fig. 2.16).

Based on the above results, we propose a conceptual model for the genesis of Eugene resulting from the merging MCVs (see Fig. 2.21). Assuming that as the two MCVs approach each other adiabatically without the influence of vertical shear, both the isentropic and isobaric surfaces will be bowl-shaped below and upward-deformed above the merging midlevel warm anomalies, facilitating the formation of a midlevel mesotrough (Figs. 2.21a,b). This trough would help reduce pressure below and induce quasi-balanced lifting in the lower troposphere, thereby leading to the low-level mass and moisture convergence and triggering of deep convection (cf. Figs. 2.21c and 2.12).

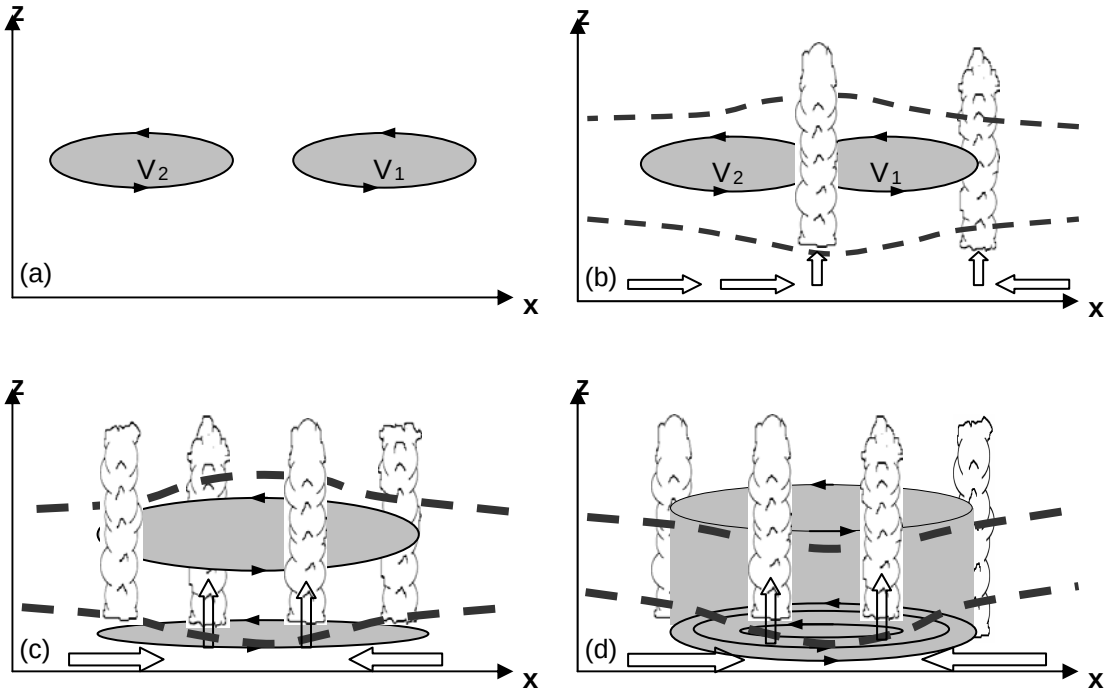

Figure 2.21. A schematic description of tropical cyclogenesis from two merging MCVs: (a) prior to the merger; (b) during the initial merging phase; (c) complete merging of the midlevel MCVs; and (d) the formation of a tropical storm. The shaded areas with thin arrows denote MCVs; dashed lines show isobaric or isentropic surfaces; and large shaded arrows represent lower-level flow directions.

It is the subsequent positive feedback between latent heat release, surface pressure fall and low-level convergence that could more efficiently cause the rapid growth of cyclonic vorticity in the bottom layers through stretching, thus triggering the WISHE processes leading to TCG. In the absence of deep convection, the vortex merger would show little growth of the storm-scale vorticity. The midlevel trough associated with the merger only plays an important role in organizing the development of deep convection, as also noted in Zhang and Bao (1996a,b). The storm-scale cyclonic vorticity will then grow from the bottom upward in convective towers distributed in the "eyewall," after the midlevel and low-level circulations are locked (cf. Figs. 2.21c,d and 2.20e,f). The merging phase is characterized by the increased rates in latent heating (and upward motion), the low-level convergence and cyclonic vorticity

growth, surface pressure falls, and particularly the large PV (and cyclonic vorticity) increases occurring in most portion of the troposphere with the peak magnitude near the top of the PBL (in the PBL).

6.6. Sensitivity experiments

In the preceding sections, we have shown the important roles of the vortex merger in the transformation of a weak tropical disturbance (i.e., V_2) to TS Eugene (2005) in the context of PV and vorticity budgets, and of the stretching in the PBL in the bottom-up growth of cyclonic rotation. One may ask: how critical the vortex merger is for the genesis of Eugene? Will the initial disturbance sooner or later grow to a TS, since the vortex-merger and frictional convergence may just affect the initial growth rates of the storm?

To address the above questions, the following three sensitivity experiments are conducted, using the results shown above as a control run (Exp. CTL). In the first experiment, V_1 is removed, due to its much small volume of high-PV concentrations than V_2's (see Figs. 2.12 and 2.13), from the model initial conditions using the PV inversion approach (Exp. NOV1), following Huo et al. (1999) but with the algorithm of Wang and Zhang (2003). Although the initial condition is modified in NOV1 experiment, the boundary conditions of the outermost domain will be kept unchanged, that is, it will be continuously updated from the global NCEP reanalysis. Strictly speaking, because of the use of such global boundaries, this NOV1 experiment is not truly solving an initial value problem. However, allowing for updated boundaries from the NCEP reanalysis will ensure consistent time-dependent large-scale flow for the experiment, and the main purpose is to focus on how the remaining vortex, i.e. V_2, responses within that same environment, e.g., whether it will grow or decay, how the

intensification is, or what is the peak intensity,. Examining the large-scale analysis, nonetheless, shows little changes of the flow pattern in the genesis area during the course of integration (not shown), and outermost boundaries are thus fairly stationary. Fig. 2.22 compares the horizontal distribution of the vertical relative vorticity for the CTL initial conditions to that with the removal of V_1. Clearly, little vortical flows are present over the area originally occupied by V_1. Note that although the temperature field is modified after the removal to ensure the balanced dynamics, the relative humidity is kept unchanged from the CTL initial conditions.

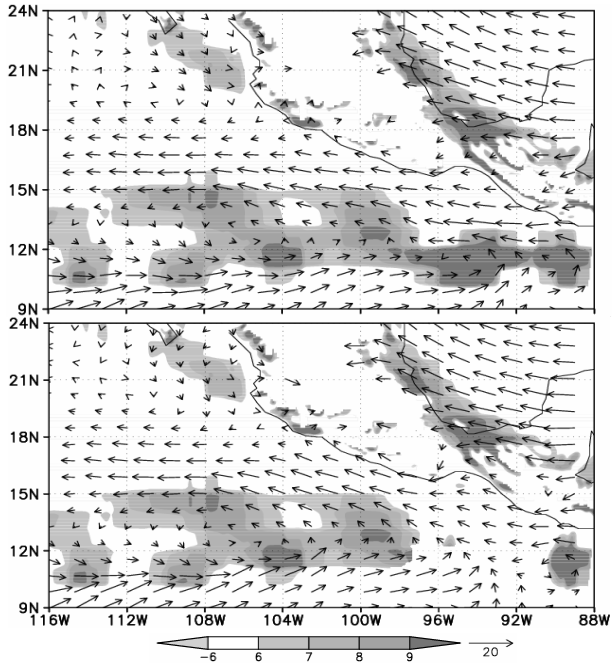

Figure 2.22. Initial condition of the vertical component of the absolute vorticity field at z = 3 km (shaded in the intervals of 10^{-5} s^{-1}) for (a) control run; and (b) after the MCV V_1 is removed from the initial condition valid at 17/00-00. Superimposed is the flow field (vectors) at the corresponding level.

A comparison of Exps. NOV1 and CTL will allow us to examine the relative importance of the vortex merger and vortex roll-up in the genesis of Eugene. In the second experiment (Exp. NFRC), the surface frictional forcing in the horizontal momentum equations is gradually reduced while keeping the calculations of surface

sensible and latent heat fluxes in the thermodynamic and moisture equations the same as those in Exp. CTL. A friction-reduction parameter of μ is used, according to $\mu = e^{-\alpha t}$ where α is the inverse of an e-folding time scale chosen to be $(18\ \text{h})^{-1}$, to provide a smooth transition long before the vortex merging occurs. This simulation will help understand the relative importance of not only the frictional convergence versus the vortex merger but also WISHE versus CISK in Eugene's genesis. In the third experiment, the 12-km nested domain is shifted to the east to enhance the influence of Hurricane Emily (2005) on the track of V_1 because of their close distance at the initial time (Exp. SHIF). As shown in Chapter 6, a less-than-100-km difference in V_1's CTL track may miss its coalescence and capture scenarios with V_2. This different track may be caused by even slight increases in intensity and the westward movement of Emily as a result of the increased horizontal resolution. Each of the above sensitivity simulation is performed with all the model conditions identical to the control run except for the treatment of each of the three different parameters.

Figs. 2.23 and 2.24 compare the tracks, and the circulation fields at 18/06-39, and the time series of the sensitivity-simulated storm intensities to those in Exp. CTL. With the removal of V_1, V_2 tends to evolve mainly as a result of the ITCZ breakdown and its subsequent polarward roll-up (Fig. 2.23). The MCV moves slowly along its initial north-northeastward track at the eastern end of the ITCZ prior to 18/06-39, and then turns westward to the south of the CTL track under the steering of the larger-scale southwesterly flow. But during the later stage the storm still moves at a slow speed, as compared to that in CTL, owing to the absent momentum of the fast-moving V_1. Without the PV contributions of V_1, the storm also evolves at the same slow rate in intensity as before, as can be expected (Fig. 2.24). Moreover, there are little

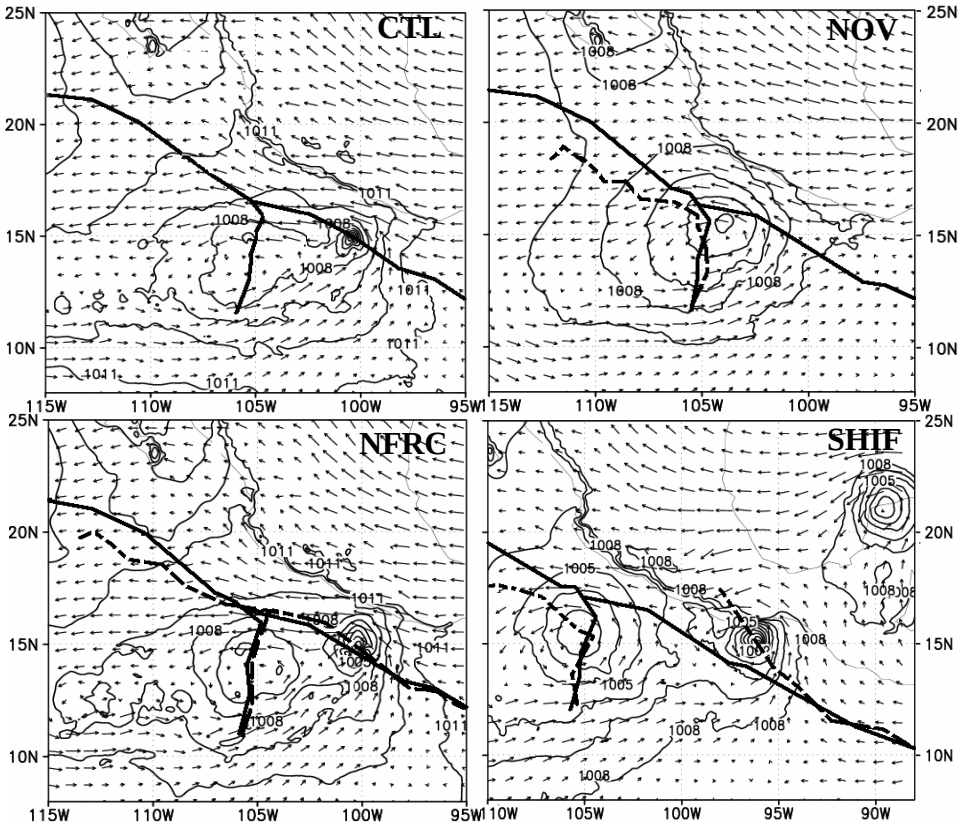

Figure 2.23. Simulated tracks for the control run (solid) and three sensitivity experiments (dashed): V_1 is removed from the initial condition (NOV1), no frictional convergence (NFRC), and 12 km domain is shifted 500 km to the east to include Hurricane Emily nearby (SHIF). Superimposed are the 700 hPa flow field (vectors) and sea level pressure (contour, intervals of 1 hPa) valid at 18/06-39. Note that dash line in CTL panel is for the best track.

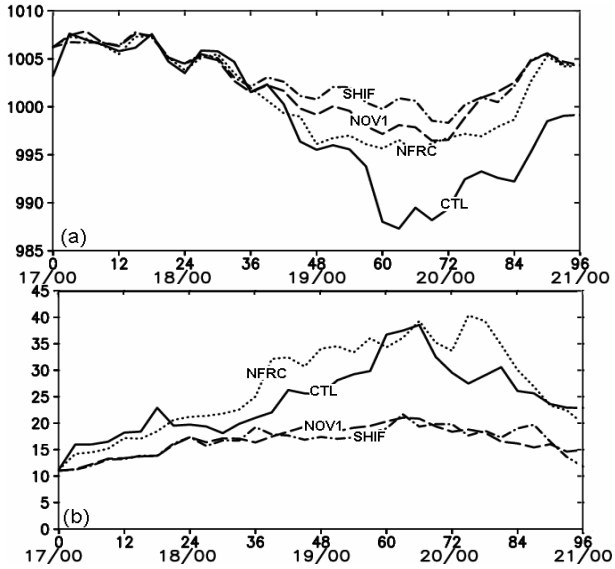

Figure 2.24. Time series of the simulated minimum sea-level pressure (hPa) during the 4-day period of 17/00-00 to 21/00-96 for the sensitivity experiments: control run (solid), NOV1 (dashed), NFRC (dotted), SHIF (dotted-dashed).

evidences of sharp increases in QCON and QH and other forcings in the PV and vorticity budgets during its life cycle (not shown). Clearly, the vortex merger accounts for a sharp drop in central pressure and an increase in surface wind starting at 18/18-42, and the subsequent WISHE process is responsible for about 11 hPa pressure drops and over 15 m s^{-1} wind speed increases at the mature stage (cf. Figs. 2.24 and 2.7). The result indicates that the ITCZ breakdown and its subsequent roll-up mechanism due to the Charney-Stern instability, as discussed in WM06 and Nieto Ferreira and Schubert (1997), could not alone initiate the WISHE process leading to the genesis of Eugene.

Without the surface frictional effects in Exp. NFRC, the two MCVs could still be merged with the tracks similar to those in CTL (see Fig. 2.23). In contrast, removing the surface friction tends to cause the faster growth of horizontal winds and more upward surface fluxes of sensible and latent heat (Figs. 2.24b and 2.25), as could be expected. The maximum surface wind and the area-averaged latent heat flux in Exp. NFRC are, respectively, about 5 m s^{-1} and 70 W s^{-1} greater than those in CTL at the storms' peak intensity. Despite the vortex merging, removing the frictional forcing tends to eliminate its associated mass and moisture convergence, i.e., the Ekman pumping effects. Then the NFRC storm could only intensify, but at much smaller rates, with the convergence as induced by diabatic heating, as demonstrated in Zhang and Kieu (2006). Thus, the vortex merger could also cause the corresponding growth of the storm, albeit at smaller rates; its maximum intensity is 8 hPa weaker than the CTL storm. The result suggests that while the vortex-merging dynamics is important to the initiation of WISHE, CISK provides an important mechanism by which the surface sensible and latent heat fluxes through WISHE could be transported

into the inner-core region through the frictional convergence for the more significant deepening of the storm.

When the nested domain is shifted (Exp. SHIF), V_1 moves at a much slower speed toward Hurricane Emily instead of V_2 due to its vortex-vortex interaction with Emily. At 18/15-39, V_1's track is about 300 km to the east of the CTL one (Fig. 2.23), and it is not possible for the two MCVs to be merged. So, V_2 behaves somewhat similar in track to that in Exp. NOV1, and V_1 gets landfall and weakens with time. Without the merger with V_1, the time series of storm intensity follows closely that of the CTL storm (Fig. 2.24). This result reveals further the critical roles of the vortex merger in triggering the WISHE process leading to the genesis of Eugene.

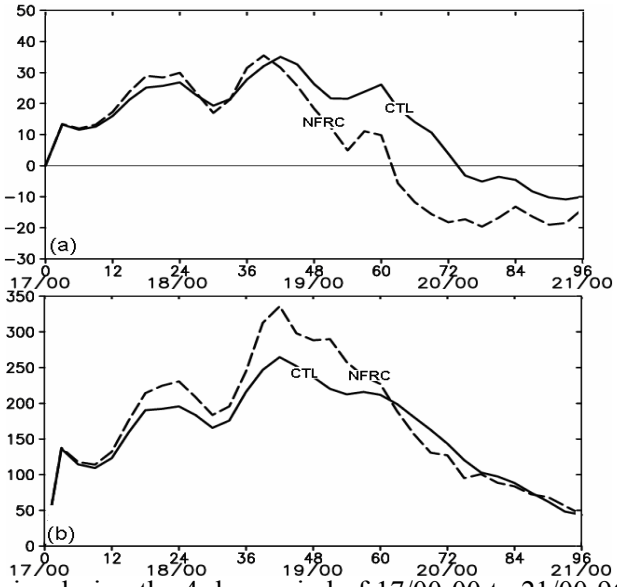

Figure 2.25. Time series during the 4-day period of 17/00-00 to 21/00-96 of the area average of (a) the sensible heating flux; and (b) latent heat flux for the CTL (solid) and NFRC experiments (dashed). The unit is W s^{-1}.

Chapter 7. Roles of vertical wind shear

Previous studies have shown the effects of VWS on the development of wavenumber-1 precipitation structures of hurricanes in which isentropic surfaces across the eye are markedly deformed (Frank and Ritchie 2001; Black et al. 2002; Zhang and Kieu 2006). It is unclear to what extent such a conceptual model could be applied to a weak tropical storm like Eugene, in which isentropic surfaces are weakly deformed. For this purpose, Fig. 2.26 shows the evolution of the simulated radar reflectivity, horizontal flows and the area-averaged hodographs at 12-h intervals from the 36 – 96 h simulations. One can see the development of more (small scale) intense convective cells during the genesis stage, as indicated by the radar reflectivity of greater than 50 dBz. This is particularly true in the southern semicircle at 19/12-60 when the storm reaches its peak intensity. As can be seen from Figs. 2.26-2.28, this active convection region around the rain-free "eye" is similar in many characters to the eyewall associated with a hurricane. (Of course, the simulated "eye" is not free of clouds because they have little contribution to radar reflectivity.) After reaching the storm's peak intensity, weaker and larger-sized convective cells develop in the "eyewall," with most precipitation being stratiform during the decaying stage, e.g., at 21/00-96.

On the other hand, the large-scale mean flows have been substantially disturbed, including the midlevel jet, due to the upstream influence of Emily and the development of Eugene (cf. Figs. 2.5a and 2.26). For example, the northwestward rollup of the ITCZ by Eugene brings in tropical large-scale southwesterly flows and

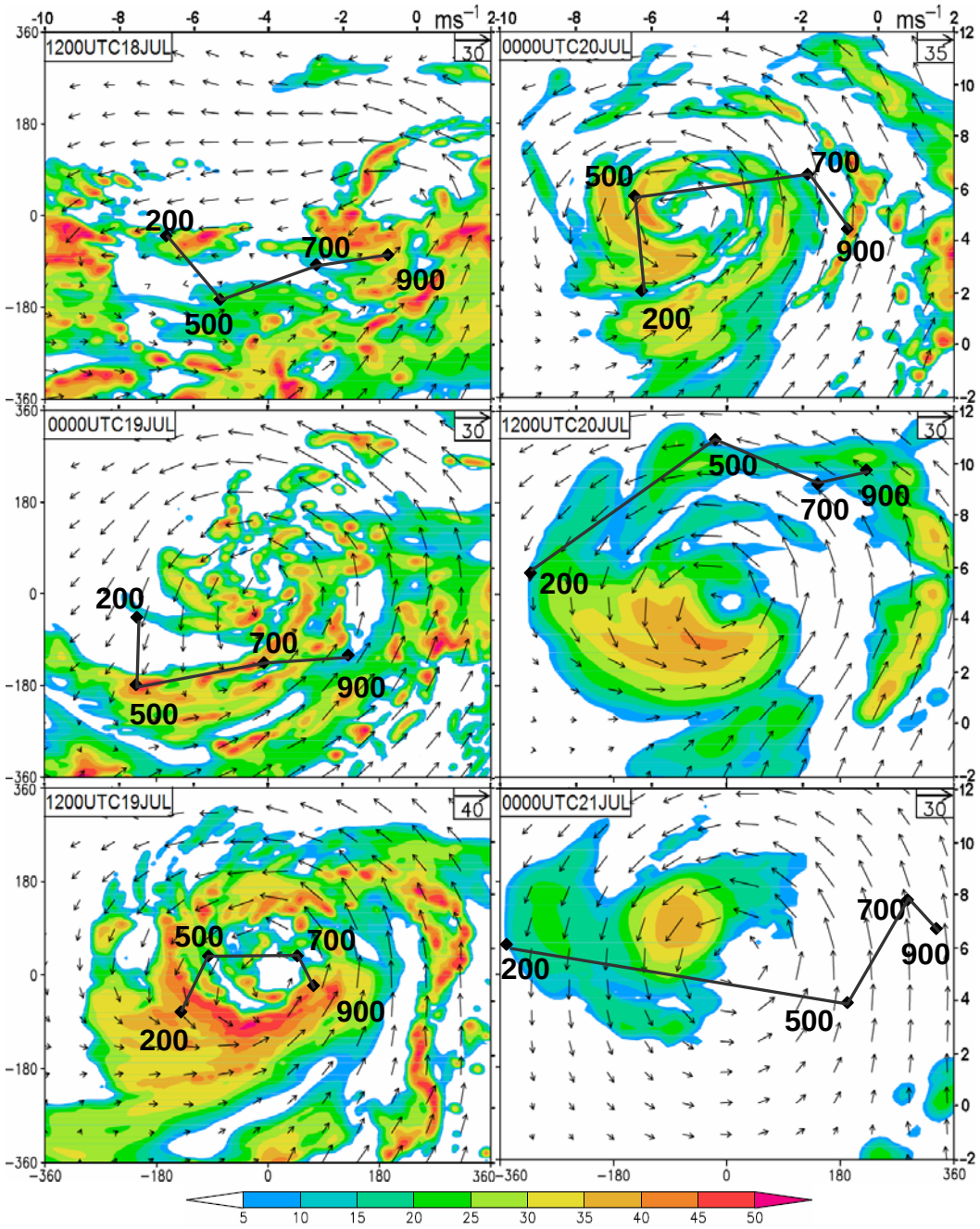

Figure 2.26. Horizontal distribution of the radar reflectivity (shaded at 5-dBz intervals) and flow vectors at 850 hPa at 18/12-36, 19/00-48, 19/12-60, 20/00-72, 20/12-84, and 21/00-96 over a subdomain of C. Hodographs with vertical shear vectors (solid) between 900 and 200 hPa, that are obtained by averaging them over an area of 800 km × 800 km at the storm center, are sketched with the speed scale given on the top and right frames.

forces the midlevel easterly flows to go northwestward, thereby giving rise to northwestward wind shifts in the mean flows at 700 and 500 hPa between 19/12-60 and 20/12-84. As a result, the mean VWS shifts from easterly at 8 m s^{-1} prior to the merger to northeasterly at 12-14 m s^{-1} near the end of the 4-day integration.

Given the VWS in the selected layers, it is important to note that more intense precipitation in the inner-core region occurs more or less in the southwestern quadrant or on the downshear-left side of the storm except at the final dissipated stage (i.e., at 21/00-96), particularly when the 500 – 900 hPa layered VWS representing better the effects of the midlevel jet is considered. The development of a warm-core structure, as shown in Figs. 2.27 and 2.28, supports the downshear-left distribution of precipitation at this early stage of a TS. Such a downshear-left asymmetry is not applicable at 21/00-96 with respect to the deep-layer VWS, but still valid when the 700 - 900 hPa VWS is considered. This consideration is justifiable in view of the fact that Eugene has become a weak and shallow MCV at this time. Moreover, the weak convective rainfall on the downshear-right still occurs in the favorable semicircle of uplifting, according to Zhang and Kieu (2006).

Note that the VWS vectors rotate with height at 19/12-60 and 20/00-72, which appears to complicate the simple relationship between the mean VWS and its induced vertical motion. According to Zhang and Kieu (2006), the VWS-induced vertical motion at any vertical layer results from the summed vertical motion induced by the VWSs from all the vertical layers, although it is more dominated by the VWS at the same layer. Thus, the vertical rotation of VWS may account to a certain extent for the generation of downshear-right precipitation. Of course, convective developments in the outer region (i.e., about 200 km outward from the center) are more related to the

rollup of the ITCZ feeding CAPE into the storm, but they weaken as propagating cyclonically to the northern semicircle where the atmospheric conditions are less favorable, including the presence of strong VWS.

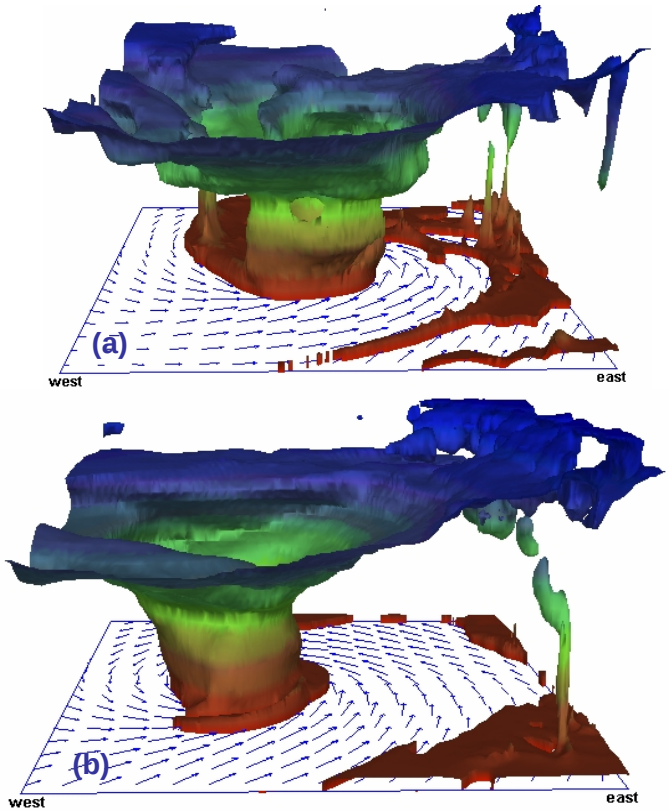

Figure 2.27. Three-dimensional view (800 km × 800 km × 12 km) of the θ_e = 352 K isosurface superimposed by the storm-relative surface flow vectors from a subdomain of C at (a) 19/18-66; and (b) 20/06-78.

Fig. 2.27 shows the three-dimensional distribution of a constant θ_e surface (i.e., 352 K) denoting roughly the "eyewall" at two different stages in order to gain insight into the effects of VWS on the vertical structures of the storm. Evidently, Eugene exhibits little vertical tilt at the most intense stage during which VWS is less than 5 m s^{-1} (cf. Figs. 2.7b and 2.27a). In addition, we can see pronounced convectively generated warming and moistening (i.e., high-θ_e air) in the inner-core region in the upper

troposphere, as also shown in vertical θ_e cross sections in Fig. 2.28. By comparison, the storm begins to tilt west-to-southwestward as VWS increases. Meanwhile, the volume of high-θ_e air in the PBL shrinks, feeding less CAPE to the "eyewall" for convective developments. As a result, the volume of high-θ_e air in the upper outflow layer decreases, which coincides with less convective developments in the "eyewall" and the subsequent weakening of the storm (cf. Figs. 2.7, 2.26 and 2.27b).

Fig. 2.28 shows the effects of VWS on the initiation of moist downdrafts, more significantly in the midlevel minimum-θ_e layer (i.e., near 700 hPa herein), on the upshear side of the storm, which coincides with downward motion as induced by vertical shear (see Zhang and Kieu 2006). As in Fig. 2.26, one can see the high-θ_e air in the inner-core region, but the highest θ_e values (i.e., $\theta_e > 354$ K) appeared in the "eyewall" result from the convective transport of high-θ_e air from the PBL in "vortical hot towers" (Fig. 2.28a). This is in contrast to the low-θ_e intrusion (i.e., $\theta_e <$ 342 K) from the vast source region to the west of the storm. Of relevance here is the development of wide downdraft bands outside the "eyewall," more significantly on the upshear side with respect to the shear vector in the 700-900 hPa layer (Fig. 2.28a). Similar features have also been observed in the upper troposphere in the simulation of Hurricane Bonnie (1998) due to the presence of an intense deep-layer (200 – 900 hPa) unidirectional VWS of 18 m s^{-1} (see Figs. 8 and 16 in Zhu et al. 2004).

Vertical θ_e-cross sections show that the downdraft bands are generated by convergence of the midlevel lower-θ_e air towards the "eyewall" clouds, i.e., the dry intrusion (Figs. 2.28b, c). These downdrafts do not seem to be (dry) isentropically induced by VWS as described by Raymond and Jiang (1990) and Fritsch et al. (1994),

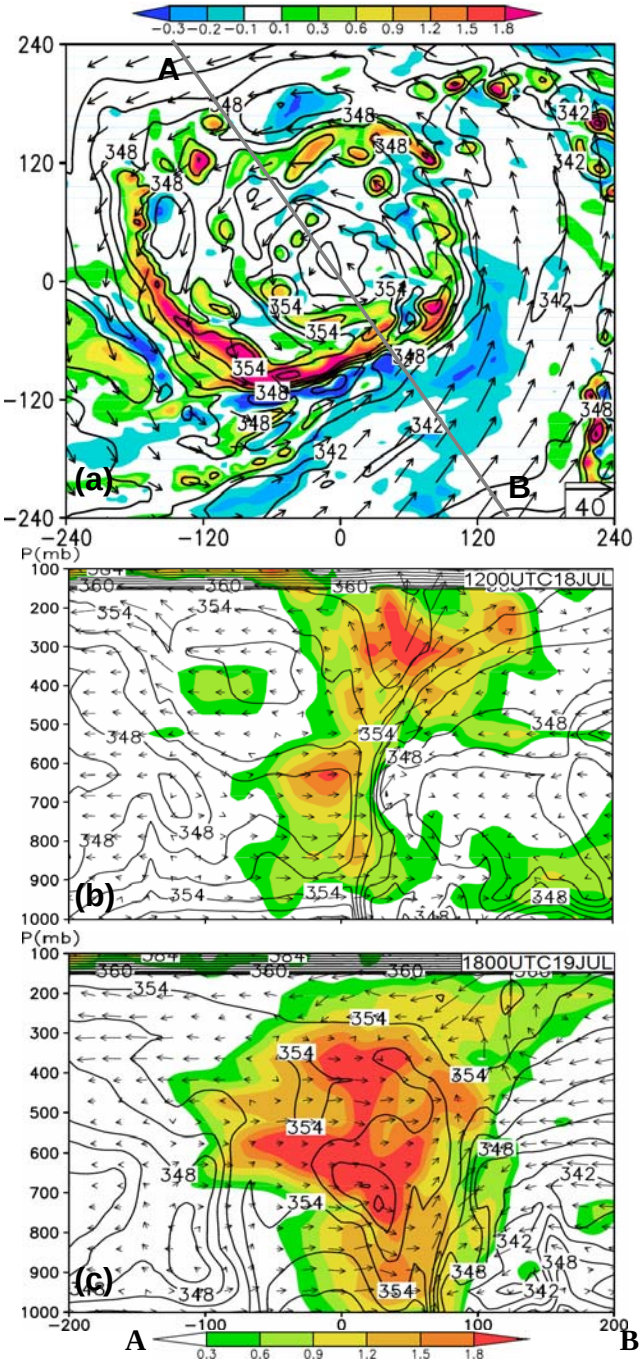

Figure 2.28. (a) Horizontal distribution of θ_e (at intervals of 2 K), flow vectors, and vertical motion (shaded at intervals 0.1 m s^{-1} for descending and 0.3 m s^{-1} for ascending motion) at 700 hPa at 19/12-60; (b) as in (a) but for vertical cross section through the storm center of θ_e (at intervals of 2 K) and deviation potential temperature (θ', shaded); and (c) as in (b) but for 19/18-66. Superimposed in (b) and (c) are the storm-relative in-plane flow vectors. Note that the vertical motion has been amplified by a factor of 10. Line A-B in (a) shows the 3-slice-averaged (i.e., 4-km) vertical cross sections used in (b) and (c).

but evaporatively driven, because (positive) potential temperature perturbations (θ') only occur in the "eye" close to active "eyewall" convection (see Figs. 2.28b, c). The penetrative moist downdraft air carrying the midlevel lower-θ_e values would be advected cyclonically in the PBL such that deep convection could be suppressed downstream in the "eyewall," likely enhancing the precipitation asymmetry in the "eyewall" and weakening of the storm. Obviously, the midlevel convergence of low-θ_e air is unfavorable for TCG, in contrast to the typical low-level convergence of higher-θ_e air. Furthermore, the cold moist downdrafts, occurring side by side with the "eyewall" updrafts, tend to strengthen the θ_e (and temperature) gradients across the "eyewall" (cf. Figs. 2.28b, c). Thus, the upshear generation of moist downdrafts through dry intrusion may be considered as the thermodynamical impact of VWS on TCG as well as on MCSs and deep convection, in contrast to the VWS-induced dynamical (isentropic) lifting in MCSs and TCs (Raymond and Jiang 1990; Zhang and Kieu 2006).

Note the bifurcation of vertical circulations associated with the midlevel convergence of lower-θ_e air in the environment: one branch entering the "eyewall" updrafts above the minimum-θ_e layer and the other branch forming the moist downdrafts below. The upper-level intruding lower-θ_e air can be cyclonically advected into the storm, due to the presence of less inertial stability aloft. This will cause the weakening of the convective updrafts in the "eyewall," and in some cases induce moist downdrafts in the upper levels as shown by Zhu et al. (2004). Note also the strong asymmetries in the subsidence warming and secondary circulations in the vicinity of active convection, which are different from those seen in hurricanes (e.g., Liu et al. 1999; Zhu et al. 2004; Zhang and Kieu 2006). The pronounced converging

flows in the lower-level inner-core region should not be considered as radial flows, but being caused mostly by the vertical tilt and asymmetries of the "eyewall."

Chapter 8. Summary

8.1. Discussions and conclusions

In Part II, TCG from merging MCVs associated with the ITCZ breakdowns is examined through a case study of the processes leading to the genesis of TS Eugene (2005) over the eastern Pacific from its pre-genesis to dissipation stages. This is achieved by using the NCEP reanalysis, satellite data and the best-track analysis, and by performing 4-days (0000 UTC 17 – 0000 UTC 21 July 2005) two-way interactive, movable, multi-nested cloud-resolving simulations using the WRF model with the finest grid size of 1.33 km. The dynamical and thermodynamic effects of VWS associated with a midlevel easterly jet on the genesis and dissipation as well as the three-dimensional structures of the storm are also explored.

Observational analyses reveal that Eugene grew out of two merging midlevel MCVs: one (V_1) initiated before 0000 UTC 11 July on the eastern end of the ITCZ breakdown, and a second one (V_2) spawned 2 days later from the ITCZ with a distance of 1000 km apart from V_1; both had an initial size of about 400 km in diameter. The earlier ITCZ breakdown appeared to be associated with the interrupting moisture convergence by trade winds over the Central American continent, whereas the growth of V_2 resulted in another ITCZ breakdown and its subsequent polarward rollup due to the presence of the Charney-Stern instability. The two MCVs moved at similar speeds northwestward, while keeping a distance of 900 – 1100 km between, offshore along the Mexican coast during the first 3 days after the formation of V_2. But later V_2 began to move slowly north-northeastward in association with the polarward

rollup of the ITCZ while V_1 moved at nearly the same velocity as before. It was the track change of V_2 that allowed the two MCVs to merge 2 – 3 days afterward, leading to the genesis of Eugene.

Although the WRF model is initialized at 0000 UTC 17 July with the NCEP reanalysis without any bogus data, it reproduces the different movements of the two midlevel MCVs with little surface signals, the intensification and size shrinkage of V_1 at the later stages, their merging interactions at nearly the right timing and location at 39 hours into the integration, and the subsequent track and intensity of the merger in association with the polarward rollup of the ITCZ. Model results show that the two MCVs interact and merge in a coalescence and capture mode, namely, V_1 is impinged upon V_2's circulation and then captured by V_2. However, the vortex merger is shown in the context of PV not simply as the capture of one MCV (V_1) by another (V_2) but as the gradual capture of each of γ-scale CGVs, including VHTs, in the slowly northward-moving V_2 by the fast northwestward propagating V_1. Results show that the ITCZ, in which V_1 and V_2 are embedded, is distributed with many PV patches or CGVs. During the merging phase, V_1 acts as a "comma head" to roll up PV-containing CGVs in V_2 and then in the ITCZ, leading to the concentration of high PV near the center of cyclonic circulation with its peak amplitude slightly above the melting level and eventually to the formation of TS Eugene. Of importance is that the low-level PV also increases in magnitude and coverage, resulting from the advection of PV substance associated with the above-mentioned CGVs on isentropic surfaces.

The above PV changes are quantified for the life cycle of Eugene through the bulk PV budget, showing that the bulk PV doubles in magnitude during a 24-h intensifying period, due partly to the net internal dynamical forcing between the PV

condensing and diabatic production and partly to the continuous PV fluxes from the ITCZ. Without the latter, the storm would be much shorter-lived under the influence of intense vertical shear. Unlike the bulk PV budget in which the PV condensing and diabatic production are similar in magnitude but opposite in sign, the area- and slice-averaged PV budgets show markedly different 3D distributions between the two forcing terms, which are more or less balanced by the vertical and horizontal PV flux divergence. Results show that the melting and freezing appear to affect markedly the vertical structures of diabatic heating, mass convergence, vertical vorticity, PV and its production during TCG and the life cycle of TCs. Results also show the significant horizontal contributions to PV and its production due to the presence of horizontal vorticity that is 30 – 40 times greater than the vertical absolute vorticity.

It is shown that the vertical absolute vorticity (η) exhibits initially midlevel maxima associated with MCVs, followed by the rapid growth of cyclonic vorticity in the PBL during the merging phase and the subsequent elevation of the peak vorticity to a level close to the melting level at the early decaying phase. The latter could be attributed to the positive bulk stretching in the presence of 2D convergence growing in depth below the heating maximum. The bulk η-budget reveals that the vorticity growth occurs in the deep troposphere during the merging phase, but the most rapid rates appear in the bottom layers due to the important stretching contributions associated with the frictional convergence and latent heat release. Of particular importance is that unlike PV, the vortex merger does not increase midlevel cyclonic vorticity because of lacking midlevel convergence. Thus, we conclude that the cyclonic vorticity must grow from the bottom upward as a route to TCG in the case of vortex merger.

The merging of the two relatively shallow systems reduces rainfall asymmetries with deep convection in all quadrants, likely accounting for the pronounced reduction of larger-scale VWS in a deep layer and allowing the merger to deepen quickly into TS (Eugene) intensity. As the two MCVs are being merged, the low- to mid-level PV and tangential flows increase substantially; the latter occurs more rapidly in the lower troposphere, helping initiate the WISHE process leading to the genesis of Eugene. Subsequently, Eugene moves northwestward with characters of both MCVs. The merging scenarios appear to differ from those presented in RH97 in which MCVs merged within a larger-scale cyclonic system. It is found from sensitivity simulations that in spite of the presence of the Charney-Stern instability in the vicinity of the ITCZ none of the MCVs could grow into tropical depression strength when they either fail to merge or merge too late.

We have also demonstrated that the simulated tropical storm exhibits many features that are similar to a hurricane, such as the warm-cored "eye" and the rotating "eyewall" as seen from the radar reflectivity, strong thermal gradients across the "eyewall," RMW, and spiral rainbands. It is found that strong VWS associated with the midlevel jet could also force the storm to tilt downshear and produce the typical wavenumber-1 rainfall structures during the genesis stage, which are similar to those found in hurricanes. In addition, VWS has the thermodynamical impact on the upshear generation of moist downdrafts in the vicinity of the "eyewall" as a result of dry intrusion, particularly in the minimum-θ_e layer. Based on the above-mentioned results, we may conclude that the ITCZ breakdown provides a favorable environment with dynamical instability, high humidity and background vorticity, but the merger of the two MCVs is critical for the genesis of Eugene. The storm decays as it moves

northwestward, farther away from the ITCZ, into an environment with increasing VWS, dry intrusion, colder SST and dynamical stability. Because the ITCZ breakdown occurs frequently during the warm season, the above results appear to have some important implications to the high density of TCG events over the eastern Pacific.

8.2. Future research plans

To explore further the cyclogenesis associated with vortex-vortex interaction, we plan to perform more sensitivity experiments, using the same WRF model with the same and/or modified model configurations. These experiments are designed to help illustrate the roles of ITCZ and its associated PV fluxes in the formation of Eugene. A specific focus will be whether the genesis and intensification of Eugene could occur if the PV fluxes from the ITCZ through the lateral boundaries are eliminated and, if so, is it true that Eugene will soon become short-lived in the absence of PV fluxes even with the help of WISHE mechanism. The ultimate goals are to obtain a better understanding of TCG associated with multiple-vortex merger in Eastern Pacific, an area which currently has the highest density of TCG events on Earth. Addressing such issue will provide some answers toward the connection between TCG and global changes.

In addition to numerical studies of TCG, my future objectives are to expand the theoretical model presented in Part I to study the dynamics and thermodynamics of the TCG in response to the organized deep convection. These objectives can be achieved by including all the nonlinear terms in the thermodynamic and the vertical momentum equations. This will allow us to have a more complete picture of the roles of the SC in controlling the development of TCs without the unbounded growth that

our current theoretical model encounters. Some preliminary numerical results appear to suggest that the inclusion of such nonlinear terms can eliminate the exponential growth, and TCs will approach a stationary mature stage after a period of few days. Also, the eyewall pattern emerges gradually during TC development, and this seems to provide some new insights into the formation of hurricane eyewalls. In addition, we plan to develop a numerical program, based on our analytical solutions, that allows us to construct a 3D vortex structure for operational purposes of TC initialization, given an initial profile of diabatic heating (or the vertical motion) as well as few point-values of the tangential wind. The same procedures in deriving the exact solutions as presented in Chapter 3 can also be applied to different initial profiles of the diabatic heating beyond the top-hat function, e.g., smoother Gaussian profile or the eyewall-shape profile during the mature stage. This will be the subjects in our upcoming works.

Appendix I. Derivation of solution (1.36)

To obtain Eq. (1.36), substituting Eq. (1.33) into Eq. (1.32) and manipulating for a few steps, a differential equation for *G(z)* is obtained:

$$\frac{dG}{G} = \frac{W_0\lambda\cos(\lambda z) - W_0 S\sin(\lambda z) - \mu\beta}{W_0\sin(\lambda z)}dz. \qquad \text{(A1.1)}$$

Integrating (A1.1) with respect to z gives:

$$\ln(G) = \ln[\sin(\lambda z)] - \frac{\mu\beta}{W_0\lambda}\ln[\tan(\frac{\lambda z}{2})] + \ln(G_0) - Sz, \qquad \text{(A1.2)}$$

from which Eq. (1.34) is followed readily as

$$G(z) = G_0\sin(\lambda z)e^{-Sz}/[\tan(\frac{\lambda z)}{2})]^{\frac{\mu\beta}{W_0\lambda}}. \qquad \text{(A1.3)}$$

Note at $z = 0$, $G(z)$ may be singular. To eliminate this singularity, there must be some restriction on λ, β, μ, and W_0. Using L'hopital's rule, one will obtain the criteria (1.38), i.e., $\mu\beta < \lambda W_0$.

Appendix II. Derivation of solution (1.41)

Let $F^{(1)}(z,t) = \Gamma(z,t)F_h(z,t)$, from Eqs. (1.31) – (1.32), we have

$$F_h\frac{\partial\Gamma}{\partial t} = -e^{\beta t}HF_h\frac{\partial\Gamma}{\partial z} - F^{(0)}, \qquad \text{(A2.1)}$$

or

$$e^{-\beta t}\frac{\partial\Gamma}{\partial t} + H\frac{\partial\Gamma}{\partial z} = -\frac{F^{(0)}e^{-\beta t}}{F_h}. \qquad \text{(A2.2)}$$

After performing coordinate transformation from (z, t) to a pair of new dependent variables (p, q) defined by

$$p = \int e^{\beta\tau}d\tau = \frac{1}{\beta}e^{\beta t} \quad \text{and} \quad q = \int\frac{1}{H(\tau)}d\tau = \frac{1}{\lambda W_o}\ln[\tan(\frac{\lambda z}{2})], \qquad \text{(A2.3)}$$

Eq. (A2.2) can be rewritten as

$$\frac{\partial \Gamma}{\partial p} + \frac{\partial \Gamma}{\partial q} = R(p,q) \equiv -\frac{F^{(0)}(p,q)e^{-\beta t(p)}}{F_h(p,q)}, \tag{A2.4}$$

where

$$F_h(p,q) = \sin(\lambda z)e^{-Sz}\exp(\mu e^{\beta t})/[\tan(\frac{\lambda z}{2})]^{\frac{\mu\beta}{W_0\lambda}}, \tag{A2.5}$$

where the implicit dependence of z on q and t on p will be obtained from (A2.3). The solution of (A2.4) can be found by first finding its homogeneous solution, and then using the method of variational coefficients (see e.g., Polyamin et al. 2001), we obtain

$$\begin{aligned}\Gamma(p,q) &= \int_{p_0}^{p} R(\tau, q-p-\tau)d\tau + G(p-q) \\ &= \int_{p_0}^{p} \frac{F^{(0)}(\tau,q-p-\tau)e^{-\beta t}}{F_h(\tau,q-p-\tau)}d\tau + G(p-q)\end{aligned}, \tag{A2.6}$$

where $G(p\text{-}q)$ denotes a function of $(p\text{-}q)$. To eliminate the singularity of $q(z)$ at z = 0, $G(p\text{-}q) = G[e^{\beta r}/\beta - \ln(\tan(\lambda z/2))/\lambda W_0]$ will be chosen as a constant G_1. Then, solution for (A2.4) is given by

$$F^{(1)}(z,t) = \int_0^{\mu_{\max}} \left\{ [G_1 + \int_{p_0}^{p} \frac{F^{(0)}(\tau,q-p-\tau)e^{-\beta t}}{F_h(\tau,q-p-\tau)}d\tau] \frac{\sin(\lambda z)e^{-Sz}}{[\tan(\frac{\lambda z}{2})]^{\frac{\mu\beta}{W_0\lambda}}} \exp(\mu e^{\beta t}) \right\} d\mu. \tag{A2.7}$$

Note that the term G_1 is the most weighted contribution to $F^{(1)}(z,t)$ as the second term in the first-pair brackets of (A2.7) tends to decay exponentially with time. The integration over μ can be done if one notes the following straightforward integration

$$\int_0^c \frac{e^{ax}}{b^{x/c}}dx = \frac{c(e^a - b^{1/c})}{(ac - \ln(b))}. \tag{A2.8}$$

Keeping only the most weighted term G_1 in (A2.7) and use of (A2.8) gives us

$$F^{(1)}(z,t) \approx \frac{2G_1W_0\lambda}{\beta}\cos^2(\frac{\lambda z}{2})e^{-Sz}\frac{[\exp(W_0\lambda e^{\beta t}/\beta) - \tan(\lambda z/2)]}{[W_0\lambda e^{\beta t}/\beta - \ln(\tan(\lambda z/2))]}. \tag{A2.9}$$

REFERENCES

Agee, E. M., 1972: Note on ITCZ wave disturbances and formation of Tropical Storm Anna. *Mon. Wea. Rev*., **100**, 733–737.

Atkinson, G.D., and C.R. Holliday, 1977: Tropical Cyclone Minimum Sea Level Pressure/Maximum Sustained Wind Relationship for the Western North Pacific. *Mon. Wea. Rev*., **105**, 421–427.

Avila, L.A., and R.J. Pasch, 1992: Atlantic tropical systems of 1991. *Mon. Wea. Rev*., **120**, 2688–2696.

Bister, M., and K. A. Emanuel, 1997: The genesis of Hurricane Guillermo: TEXMEX analyses and a modeling study. *Mon. Wea. Rev*., **125**, 2662–2682.

Black, M.L., J.F. Gamache, F.D. Marks, C.E. Samsury, and H.E. Willoughby, 2002: Eastern Pacific Hurricanes Jimena of 1991 and Olivia of 1994: The effect of vertical shear on structure and intensity. *Mon. Wea. Rev*., **130**, 2291–2312.

Bosart, L.F., and F. Sanders, 1981: The Johnstown flood of July 1977: A long-lived convective storm. *J. Atmos. Sci.*, **38**, 1616-1642.

Challa, M., and R. L. Pfeffer, 1990: Formation of Atlantic hurricanes from cloud clusters and depressions. *J. Atmos. Sci.*, **47**, 909-927.

Charney, J. G., and A. A. Eliassen, 1964: On the growth of the hurricane depression. *J. Atmos. Sci.*, **21**, 68-75.

_____., and M. Stern, 1962: On the stability of internal baroclinic jets in a rotating atmosphere. *J. Atmos. Sci.*, **19**, 159–172.

DeMaria, M., 1996: The effect of vertical shear on tropical cyclone intensity change. *J. Atmos. Sci.*, **53**, 2076-2087.

_____, J.A. Knaff, and B.H. Connell, 2001: A tropical cyclone genesis parameter for

the tropical Atlantic. *Wea. Forecasting*, **16**, 219–233.

Dickinson, M., and J. Molinari, 2002: Mixed Rossby–gravity waves and Western Pacific tropical cyclogenesis. Part I: Synoptic evolution. *J. Atmos. Sci.*, **59**, 2183–2196.

Emanuel, K. A., 1986: An air-sea interaction theory for tropical cyclone. Part I: Steady state maintenance. *J. Atmos. Sci.*, **43**, 585-604.

_____, 1989: The finite-amplitude nature of tropical cyclogenesis. *J. Atmos. Sci.*, **46**, 3431–3456.

_____., 2000: A statistical analysis of tropical cyclone intensity. *Mon. Wea. Rev*., **128**, 1139–1152.

Eliassen, A. 1952: Slow thermally or frictionally controlled meridional circulation in a circular vortex. *Astrophys. Norv*., **5**, 60pp.

Frank, W. M., and E. A. Ritchie, 2001: Effects of vertical wind shear on the intensity and structure of numerically simulated hurricanes. *Mon. Wea. Rev*., **129**, 2249–2269.

Fritsch, J.M., J.D. Murphy, and J.S. Kain, 1994: Warm core vortex amplification over land. *J. Atmos. Sci.*, **51**, 1780–1807.

Gray, W. M., 1968: Global view of tropical disturbances and storms. *Mon. Wea. Rev*., **96**, 669-700.

Hack, J.J., W.H. Schubert, and D. E. Stevens, and H.-C. Kuo, 1989: Response of the Hadley circulation to convective forcing in the ITCZ. *J. Atmos. Sci.*, **46**, 2957–2973.

_____, and W. H. Schubert, 1986: Nonlinear response of atmospheric vortices to heating by organized cumulus convection. *J. Atmos. Sci.*, **43**, 1559–1573.

Halverson, J., M. Black, and Co-authors, 2007: NASA's Tropical Cloud Systems and Processes Experiment. *Bull. Amer. Meteor. Soc*., **88**, 867–882.

Haynes, P., and M. McIntyre, 1987: On the Evolution of Vorticity and Potential Vorticity in the Presence of Diabatic Heating and Frictional or Other Forces. *J. Atmos. Sci.*, **44**, 828–841.

Hendricks, E. A., M. T. Montgomery, and C. A. Davis, 2004: The role of "vortical" hot towers in the formation of tropical cyclone Diana (1984). *J. Atmos. Sci.*, **61**, 1209–1232.

Holland, G. J., 1997: The maximum potential intensity of tropical cyclones. *J. Atmos. Sci.*, **54**, 2519–2541.

Hoskins, B. J., M. E. McIntyre, and A. W. Robertson, 1985: On the use and significance of isentropic potential vorticity maps. *Quart. J. Roy. Meteor. Soc.*, **111**, 877–946.

Jones, S. C., 1995: The evolution of vortices in vertical shear. Part I: Initially barotropic vortices. *Quart. J. Roy. Meteor. Soc*., **121**, 821–851.

Kain, J. S., and J. M. Fritsch, 1990: A one-dimensional entraining/detraining plume model and its application in convective parameterization. *J. Atmos. Sci.*, **47**, 2784-2802.

Kieu, C. Q., and D.-L. Zhang, 2008: Genesis of Tropical Storm Eugene (2005) from merging vortices associated with the ITCZ breakdowns. Part I: Observational and modeling analyses. *J. Atmos. Sci.*, in press.

Knaff, J.A., and R.M. Zehr, 2007: Reexamination of Tropical Cyclone Wind–Pressure Relationships. *Wea. Forecasting*, **22**, 71–88.

Kurihara, Y., M. A. Bender, and R. Ross, 1993: An initialization scheme of hurricane

models by vortex specification. *Mon. Wea. Rev*., **121**, 2030 –2045.

Lander, M., and G. J. Holland, 1993: On the interaction of tropical cyclone-scale vortices. I. Observations. *Quart. J. Roy. Meteor. Soc.*, **119**, 1347–1361.

Li, X. and B. Wang, 1994: Barotropic dynamics of the beta-gyres and beta-drift. *J. Atmos. Sci.*, **51**, 746-756.

Lin, Y.-L., R. D. Farley, and H. D. Orville, 1983: Bulk parameterization of the snow field in a cloud model. *J. Climate Appl. Meteor*., **22**, 1065-1092.

Liu, Y. B., D.-L. Zhang, and M. K. Yau, 1997: A multiscale numerical study of Hurricane Andrew (1992). Part I: Explicit simulation and verification. *Mon. Wea. Rev*., **125**, 3073-3093.

_____, _____, and ____, 1999: A multiscale numerical study of Hurricane Andrew (1992). Part II: Kinematics and inner-core structures. *Mon. Wea. Rev*., **127**, 2597–2616.

McBride, J. L., 1981: Observational analysis of tropical cyclone formation. Part I: Basic description of data sets. *J. Atmos. Sci.*, **38**, 1117-1131.

_____, and R. Zehr, 1981: Observational analysis of tropical cyclone formation. Part II: Comparison of non-developing versus developing systems. *J. Atmos. Sci.*, **38**, 1132–1151.

Mlawer, E. J., S. J. Taubman, P. D. Brown, M. J. Iacono, and S. A. Clough, 1997: Radiative transfer for inhomogeneous atmosphere: RRTM, a validated correlated-k model for the long-wave. *J. Geophys. Res*., **102**, 16663-16682.

Molinari, J, D. Vollaro, David, S. Skubis, and M. Dickinson, 2000: Origins and mechanisms of Eastern Pacific tropical cyclogenesis: A case study. *Mon. Wea. Rev*., 128, 125-139.

_____, D. Knight, M. Dickinson, D. Vollaro, and S. Skubis, 1997; Potential vorticity, easterly waves, and Eastern Pacific tropical cyclogenesis. *Mon. Wea. Rev*., **125**, 2699–2708.

Möller, J. D., and M. T. Montgomery, 2000: Tropical cyclone evolution via potential vorticity anomalies in a three-diemensional balance model. *J. Atmos. Sci.*, **57**, 3366-3387.

_____, and L. J. Shapiro, 2002: Balanced contributions to the intensification of hurricane Opal as diagnosed from a GFDL model forecast. *Mon. Wea. Rev*., **130**, 1866–1881.

Montgomery, M.T., M.E. Nicholls, T.A. Cram, and A.B. Saunders, 2006: A vortical hot tower route to tropical cyclogenesis. *J. Atmos. Sci.*, **63**, 355–386.

_____, and R. J. Kallenbach, 1997: A theory for vortex Rossby-waves and its application to spiral bands and intensity changes in hurricanes. *Quart. J. Roy. Meteor. Soc.*, **123**, 435–465.

_____, M. E. Nicholls, T. A. Cram, and A. B. Saunders, 2006: A vortical hot tower route to tropical cyclogenesis. *J. Atmos. Sci.*, **63**, 355–386.

_____, and J. Enagonio, 1998: Tropical cyclogenesis via convectively forced vortex Rossby waves in a three-dimensional quasigeostrophic Model. *J. Atmos. Sci.*, **55**, 3176–3207.

Nieto Ferreira, N. R., and W. H. Schubert, 1997: Barotropic aspects of ITCZ breakdown. *J. Atmos. Sci.*, **54**, 261-285.

Ooyama, K., 1969: Numerical simulation of the life cycle of tropical cyclones. *J. Atmos. Sci.*, **26**, 3–40.

Polyanin, A. D., V. F. Zaitsev, and A. Moussiaux, 2001: Handbook of First-Order

Partial Differential Equations, *CRC Publisher*, 520pp.

Prieto, R., B. D. McNoldy, S. R. Fulton, and W. H. Schubert, 2003: A classification of binary tropical cyclone–like vortex interactions. *Mon. Wea. Rev*., **131**, 2656–2666.

Raymond, D. J., and H. A. Jiang, 1990: Theory for long-lived mesoscale convective systems. *J. Atmos. Sci.*, **47**, 3067-3077.

Reasor, P. D., M. T. Montgomery, and L. F. Bosart, 2005: Mesoscale observations of the genesis of hurricane Dolly (1996). *J. Atmos. Sci.*, **62**, 3151–3171.

Ritchie, E. A., and G. J. Holland, 1997: Scale interactions during the formation of Typhoon Irving. *Mon. Wea. Rev*., **125**, 1377-1396.

Rodgers, E. B., W. S. Olson, V. M. Karyampudi, and H. F. Pierce, 1998: Satellite-derived latent heating distribution and environmental influences in Hurricane Opal (1995). *Mon. Wea. Rev*., **126**, 1229–1247.

Rotunno, R., and K. A. Emanuel, 1987: An air-sea interaction theory for tropical cyclones. Part II: Evolutionary study using a nonhydrostatic axisymmetric numerical model. J. Atmos. Sci, **44**, 542-561.

Schubert, W. H., and J. J. Hack, 1982: Inertial stability and tropical cyclone development. *J. Atmos. Sci.*, **39**, 1687–1697.

Simpson J., E. A. Ritchie, G. J. Holland, J. Halverson, and S. Stewart, 1997: Mesoscale interactions in tropical cyclone genesis. *Mon. Wea. Rev*., **125**, 2643–2661.

Shapiro, L. J., and H. E., Willoughby, 1982: The response of balanced hurricanes to local sources of heat and momentum. *J. Atmos. Sci.*, **39**, 378-394.

Skamarock, W. C., J.B. Klemp, J. Dudhia, D. O. Gill, D. M. Barker, W. Wang, and J.

G. Powers, 2005: A Description of the advanced research WRF Version 2, *NCAR Technical Note*, 100p.

Sundqvist, H., 1970: Numerical simulation of the development of tropical cyclones with a ten-level model. I, Tellus, **22**, 359-390.

Tao, W. K., E. A. Smith, R. F. Adler, and co-authors, 2006: Retrieval of latent heating from TRMM measurements. Bull. Amer. Meteor. Soc., **87**, 1555–1572.

Wang, C.-C., and G. Magnusdottir, 2006: The ITCZ in the central and Eastern Pacific on synoptic time scales. *Mon. Wea. Rev*., **134**, 1405-1421.

Wang, Y., and G. J. Holland, 1996: Tropical cyclone motion and evolution in vertical shear. *J. Atmos. Sci.*, **53**, 3313-3332.

Willoughby, H. E., 1979: Forced secondary circulations in hurricanes. *J. Geophys. Res.*, **84**, 3173-3183.

_____, J. Clos, and M. Shoreibah, 1982: Concentric eye walls, secondary wind maxima, and the evolution of the hurricane vortex. *J. Atmos. Sci.*, **39**, 395–411.

_____, 1990: Temporal changes of the primary circulation in tropical cyclones. *J. Atmos. Sci.*, **47**, 242–264.

_____, 1990: Gradient balance in tropical cyclones. *J. Atmos. Sci.*, **47**, 265–274.

Wu, C. C., and K. R. Emanuel, 1993: Interaction of a baroclinic vortex with background shear: Application to hurricane movement. *J. Atmos. Sci.* **50**, 62-76.

Yanai, M., 1964: Formation of tropical cyclones. *Rev. Geophys.*, 2, 367-414.

Yang, M.-J., D.-L. Zhang, and H.-L. Huang, 2008: A modeling study of Typhoon Nari (2001) at landfall. Part I: Topographic effects. *J. Atmos. Sci.*, in press.

Yau, M. K., Y. Liu, D. L. Zhang, and Y. Chen, 2004: A multiscale numerical study of hurricane Andrew (1992). Part VI: Small-scale inner-core structures and wind

streaks. *Mon. Wea. Rev*., **132**, 1410–1433.

Zehnder, J.A., D.M. Powell, and D.L. Ropp, 1999: The interaction of easterly waves, orography, and the intertropical convergence zone in the genesis of eastern Pacific tropical cyclones. *Mon. Wea. Rev*., **127**, 1566–1585.

Zhang, D.-L., and J. M. Fritsch, 1988: A numerical investigation of a convectively generated, inertially stable, extratropical warm-core mesovortex over Land. Part I: Structure and evolution. *Mon. Wea. Rev*., **116**, 2660-2687.

_____, and N. Bao, 1996a: Oceanic cyclogenesis as induced by a mesoscale convective system moving offshore. Part I: A 90-h real-data simulation. *J. Atmos. Sci.*, **124**, 1449-1469.

____, and _____, 1996b: Oceanic cyclogenesis as induced by a mesoscale convective system moving offshore. Part II: Genesis and thermodynamic transformation. *J. Atmos. Sci.*, **124**, 2206-2246.

_____, and C. Q. Kieu, 2006: Potential vorticity diagnosis of a simulated hurricane. Part II: Quasi-balanced contributions to forced secondary circulations. *J. Atmos. Sci.*, **63**, 2898–29144.

_____, Y. Liu, and M. K. Yau, 2001: A multiscale numerical study of Hurricane Andrew (1992). Part IV: Unbalanced flows. *Mon. Wea. Rev*., **129**, 92-107.

_____, _____, and ____, 2002: A multiscale numerical study of Hurricane Andrew (1992). Part V: Inner-core thermodynamics. *Mon. Wea. Rev*., **130**, 2745-2763.

Zhu, T, D.-L. Zhang, and F. Weng, 2002: Impact of the Advanced Microwave sounding Unit data on hurricane forecasts. *Mon. Wea. Rev*., **130**, 2416-2432.

_____, _____, and _____, 2004: Numerical simulation of Hurricane Bonnie (1998). Part I: Eyewall evolution and intensity changes. *Mon. Wea. Rev*., **132**, 225–241.